The 3 + 1 dimensional lattice NJL model at non-zero baryon density.

Walters, David Nathan

THE 3 + 1 DIMENSIONAL LATTICE NJL MODEL AT NON-ZERO BARYON DENSITY

By

David Nathan Walters

SUBMITTED TO THE UNIVERSITY OF WALES
IN FULFILMENT OF THE REQUIREMENTS
FOR THE DEGREE OF
DOCTOR OF PHILOSOPHY
AT
UNIVERSITY OF WALES SWANSEA
SINGLETON PARK
SWANSEA
SA2 8PP
SEPTEMBER 2003

Abstract

Lattice simulations of the 3+1 dimensional Nambu–Jona-Lasinio model are undertaken that provide non-perturbative evidence for the existence of a BCS superfluid phase in the low temperature, high density regime.

Standard analytic methods are used to fit the model's free parameters to low energy vacuum phenomenology. The model is simulated numerically for a range of baryon chemical potential μ, with the introduction of a diquark source j to allow for the observation of spontaneous $U(1)$ global symmetry breaking in a finite volume system. For $\mu \gtrsim 0.6$ inverse lattice spacings and in the limit that $j \to 0$, a non-zero diquark condensate, a vanishing diquark susceptibility ratio and an energy gap $\Delta \neq 0$ about the Fermi surface in the fermion dispersion relation are all consistent with the ground-state being that of a $U(1)$-broken BCS superfluid. The ratio between the gap at $\mu = 0.8$ and the vacuum fermion mass is found to be 0.15(2). This is interpreted as tentative non-perturbative evidence for the existence of a colour superconducting phase in cold, dense QCD.

The effects of simulating on a finite volume, and any conditions this places on the above conclusions, are investigated. Finally, the results of some initial studies at non-zero isospin chemical potential and the prospect of simulations at non-zero temperature are discussed.

UNIVERSITY OF WALES SWANSEA

Author: **David Nathan Walters**

Title: **The $3+1$ Dimensional Lattice NJL Model at Non-zero Baryon Density**

Department: **Department of Physics**

Degree: **Ph.D.** Year: **2003**

This work has not previously been accepted in substance for any degree and is not being concurrently submitted in candidature for any degree.

Signature of Author

12th December 2003

Date

This thesis is the result of my own investigations, except where otherwise stated. Other sources are acknowledged by explicit references. A Bibliography is appended.

Signature of Author

12th December 2003

Date

I hereby give consent for my thesis, if accepted, to be available for photocopying and inter-library loan, and for the title and summary to be made available to outside organisations.

Signature of Author

12th December 2003

Date

Acknowledgements

I would like to take this opportunity to thank all of those without whom this thesis would not have been completed. Primarily I must thank my supervisor Prof. Simon Hands for his support and guidance, both academic and personal, throughout the course of my postgraduate studies. I thank Dr. Costas Strouthos for his advice and useful discussions. Thanks also go to the academic and support staff of the Department of Physics who have helped me during the seven years I have spent in Swansea, and to my fellow students, particularly Andrew Burgess, Gareth John, Tom Kingaby and Nic Turner.

I acknowledge the support of PPARC in funding my studentship and of the UKQCD collaboration in the provision of funds to carry out simulations at the Cambridge-Cranfield HPCF.

Finally, I would like to thank Kathryn for her endless support and encouragement.

Contents

1 Introduction **1**

1.1 The Phase Diagram of QCD 1

1.2 Lattice QCD at $\mu \neq 0$ 7

1.3 Colour Superconductivity 9

2 The Nambu–Jona-Lasinio Model **14**

2.1 NJL as a Model of QCD 14

2.2 Additions to the Standard Model 19

2.3 The Lattice Model 20

2.4 Continuum Limit of the Lattice Model 23

2.5 Phenomenological Parameter Choice 25

3 Zero Temperature Phase Structure **33**

3.1 The Simulation 33

3.2 The Chiral Phase Transition 37

3.3 Diquark Condensation and Superfluidity 42

4 Measurement of the Gap **51**

4.1 Spectroscopy in the Fermionic Sector 51

4.2 The Vacuum Dispersion Relation 58

4.3 $\mu = 0.8$: Measurement of the Gap 59

4.4 Chemical Potential Dependence of the Gap 62

5 Finite Volume Effects **68**
5.1 Reaching the Infinite Volume Limit 68
5.2 Finite Volume Study 71
5.3 The Lattice Fermi Surface 73
5.4 Large-volume Study 76

6 The Strength of the Gap **78**
6.1 Non-zero Isospin Chemical Potential 78
6.2 Quenched Simulations with $\mu_I \neq 0$ 81
6.3 Non-zero Temperature 87

7 Summary **90**

A Staggered Fermions and their Interpretation **95**
A.1 From Naïve to Staggered Fermions 95
A.2 Flavours of Staggered Fermions 96

B Computing Algorithms and Analysis **98**
B.1 The Hybrid Monte-Carlo Algorithm 98
B.1.1 The Algorithm 98
B.1.2 The Sign of the Determinant 100
B.1.3 Matrix Inversion: The Conjugate Gradient Method 101
B.2 Error Analysis 103
B.2.1 Errors in uncorrelated data 103
B.2.2 Binning and Jackknife Analysis 103
B.3 Least Squares Curve Fitting 106

C Shared-memory Parallel Programming **109**

Bibliography **114**

Chapter 1

Introduction

1.1 The Phase Diagram of QCD

For over a quarter of a century, physicists have believed strongly interacting particles such as protons, neutrons and the other baryons and mesons observed in particle accelerators not to be fundamental, but to be composed themselves of fractionally charged fermions known as quarks, and exchange bosons of the strong force known as gluons [1]. The quark model, in which baryons are thought of as bound states of three quarks and mesons as quark anti-quark pairs, successfully described the spectrum of known hadronic sates and predicted the existence of others [2]. The existence of quarks was confirmed experimentally in the early 1970s by the deep inelastic scattering of electrons and muons from the interior of nucleons, which showed evidence for the existence of point-like objects with mass approximately one third that of the proton (m_p) [3].

The model was put into a field theoretic context in 1973, with the birth of Quantum Chromodynamics (QCD) [4]. This theory describes quarks and anti-quarks as quanta of the elementary fermion fields ψ and $\overline{\psi}$, each with an $SU(3)$ colour charge, and gluons as quanta of a self-interacting non-abelian gauge field A_μ. The Lagrangian

density of QCD in Euclidean space is given by

$$\mathcal{L}_{\rm QCD} = \overline{\psi}_i^{\alpha}(i\not{D} - m_0)_{ij}^{\alpha\beta}\psi_j^{\beta} - \frac{1}{4}\mathcal{F}_{\mu\nu}^{a}\mathcal{F}_{a}^{\mu\nu}. \tag{1.1}$$

In the gauge part of the action, the gluon field strength tensor is $\mathcal{F}_{\mu\nu}^{a} = \partial_\mu A_\nu^a - \partial_\nu A_\mu^a + g f_{abc} A_\mu^b A_\nu^c$, where g is the bare coupling constant and f_{abc} are the structure constants of $SU(3)_c$. μ and ν are Lorentz space-time indices and a, b, $c = 1, \ldots, 8$ are the gluonic degrees of freedom. In the fermionic part i, j run over N_f flavours of quark, α, β run over the 3 colours, m_0 is an $N_f \times N_f$ matrix of current quark masses and $D_\mu^{\alpha\beta} \equiv \delta^{\alpha\beta}\partial_\mu - \frac{i}{2}g(\lambda^a)^{\alpha\beta}A_\mu^a$ is the covariant derivative, which observes gauge invariance. As well as the $SU(3)_c$ gauge symmetry, in the limit that $m_0 \to 0$ the theory remains invariant under global rotations in $SU(N_f)_L \otimes SU(N_f)_R \otimes U(1)_B$ of left- and right-handed chirality and Baryon number respectively.[1]

One key feature of QCD is that as a non-abelian gauge theory it has a running coupling α_s, which must be defined at some renormalisation point. In particular, at large momentum q one finds [7,8]

$$\alpha_s(q) \sim \frac{1}{\ln(q/\Lambda_{\rm QCD})}, \tag{1.2}$$

where $\Lambda_{\rm QCD} \sim 200$MeV is the QCD mass-scale. One can see from (1.2) that α_s exhibits asymptotic freedom, i.e. $\alpha_s \to 0$ as the renormalisation momentum scale goes to infinity, corresponding to a vanishing time- or length-scale. At small distances $x \ll \Lambda_{\rm QCD}^{-1}$, α_s remains small such that within the protons and neutrons of the nucleus, quarks remain approximately free. This asymptotic freedom means that at small length scales, QCD may be treated perturbatively, in the same manner as electro-weak interactions. At large length scales, however, the static quark potential

[1] The classical Lagrangian (1.1) also has an additional $U(1)_A$ symmetry which is broken in the quantum theory by instanton effects [5,6].

$V(r) \sim \frac{\alpha_s}{r} + \kappa r$, where κ is a constant, scales approximately linearly with separation, and the theory becomes inherently non-perturbative.

One method to attack this problem, Lattice Gauge Theory (LGT), was proposed by Wilson in 1974 [9]. In this prescription one defines all of the fields in the theory on a discrete Euclidean space-time lattice with non-zero lattice spacing a. This is the equivalent of introducing an on-axis ultra-violet momentum cut-off at $\Lambda \sim a^{-1}$. Because the cut-off is applied before any other assumptions are made, it is possible to solve the theory from first principles without resorting to perturbative expansion, such that in the continuum limit, the results of numerical calculations should be exact within statistical errors. Problems still persist of course: it currently remains difficult to discretise the fermion fields in both a local and chirally invariant way; it remains computationally too expensive to carry out full simulations with reasonably light current quark masses; to make both the lattice spacing small enough and the volume large enough so that space-time appears as a smooth infinite volume box to all length scales of the theory requires a very large number of lattice sites. With advances being made in both formalisms and algorithms, however, and the continuing improvement of high-performance computing, in the coming years the vacuum structure of QCD may be understood not only qualitatively, but quantitatively. For an outline of such issues see for example [10].

As well as understanding the vacuum theory as a function of its fundamental parameters, such as the number and masses of light quarks, it has become increasingly popular to ask the question: "How does the nature of QCD change when one changes the external thermodynamic parameters?". In the first few microseconds after the big bang, for instance, the temperature of the universe was about 10^{12} times higher

than it is now [11]. In heavy ion experiments, atomic nuclei are being collided at such high energies that matter in their wake can thermalise at similarly high temperatures. Also, in the cores of compact stars, strongly interacting matter can be compressed by gravity to densities of over 10^8 tonnes/teaspoonful of matter [12]. The ultimate goal of asking this question is to accurately determine the phase diagram of QCD, i.e. to map out the phases of the theory, including any transitions between them, as a function of the external parameters. For recent reviews on the QCD phase diagram see [13] and [14].

A well known example of such a phase diagram is that of H_2O, which is illustrated as a function of temperature and pressure in Fig. 1.1. The ice, water and steam phases

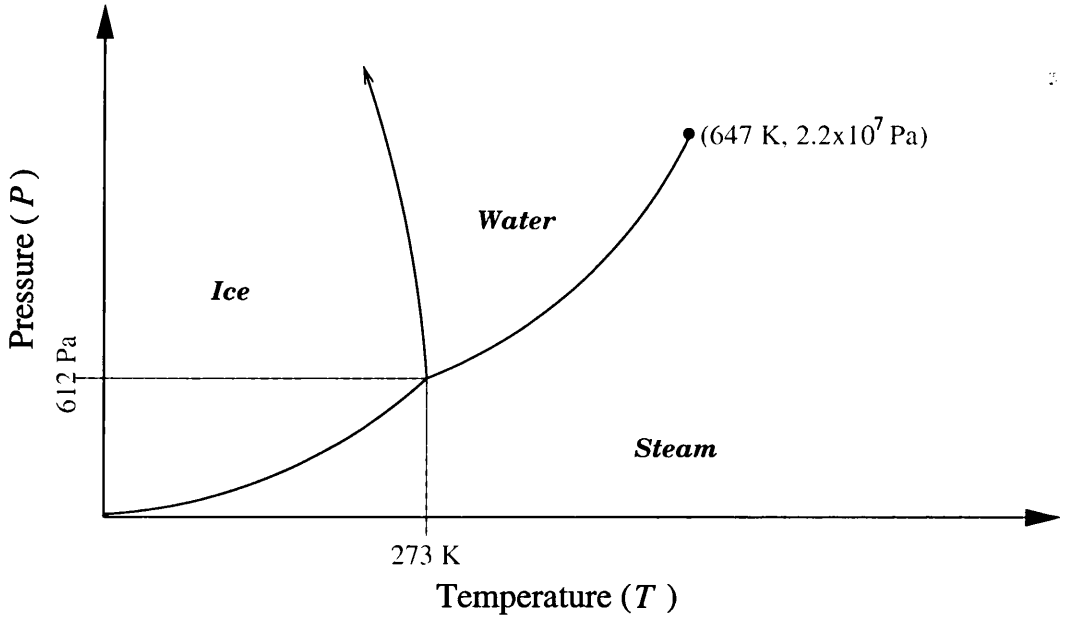

Figure 1.1: The phase diagram of H_20.

are all separated by first order phase transitions, meaning that there is a definite latent heat involved in crossing the solid transition lines. At $T \sim 650$K, however, there is a critical end point such that above this temperature there is no discernible transition

between the liquid and vapour phases. These are separated instead by a crossover, which implies that there is no exact order parameter that can distinguish between them.

A caricature of the QCD phase diagram including both known and proposed phases is presented in Fig. 1.2. The parameters on the axes are the temperature T and

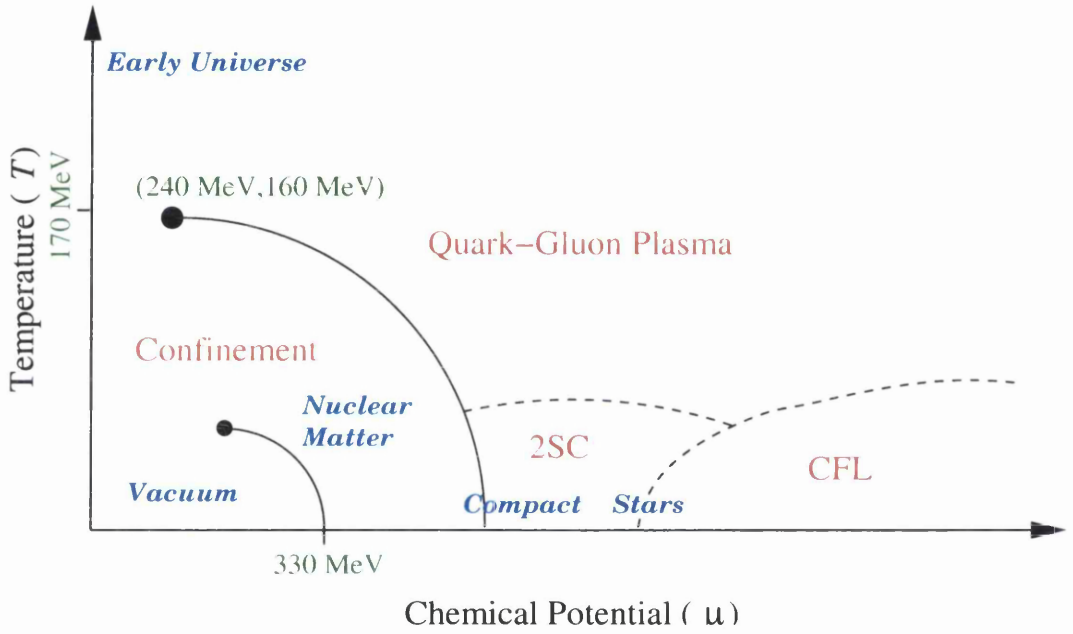

Figure 1.2: The proposed phase diagram of QCD.

the quark chemical potential μ. The world in which we live is situated in the corner of the diagram nearest to the origin. In these conditions of low temperature and chemical potential, the theory's $SU(N_f)_L \otimes SU(N_f)_R$ chiral symmetry is spontaneously broken to $SU(N_f)_V$. Since this is a global symmetry, Goldstone's theorem implies that its breaking should lead to the appropriate number of Goldstone bosons. For $N_f = 2$, corresponding to massless "up" and "down" quarks, the Goldstone modes are the three pions. Quarks and anti-quarks close to the surface of the Dirac sea with equal momentum and energy condense in pairs leading to the creation of a mass gap of

2Σ about $E = 0$. This gap causes the quarks to become massive. In this phase, the strong force is confining in that it is impossible to isolate a single quark or gluon; the only states observed are those which are singlet in the $SU(3)_c$ gauge symmetry, i.e. are colour neutral. If one tries to isolate a quark and antiquark from each other, for example, the potential between them increases linearly exhibiting string-like behaviour. Once there is enough energy in the string tension, it becomes energetically favourable for a $q+\overline{q}$ pair created from the vacuum to each bind with one of the original pair and break the string. If there is enough initial kinetic energy, this process can recur many times, which accounts for the 2 or 3 hadronic "jets" observed in particle accelerators following initial high-energy scatterings such as $e^+ + e^- \rightarrow q + \overline{q}$ or $e^+ + e^- \rightarrow q + \overline{q} + gluon$ respectively [15].

If the temperature is increased significantly from current conditions, arguments based on the bag model, in which hadronic states are modelled by free quarks confined by a "bag constant" potential, suggest that thermal fluctuations should eventually dominate and the theory should pass into a phase in which chiral symmetry is restored [16]. Quarks and gluons become deconfined into a soup called the quark-gluon plasma (QGP). This picture has been confirmed by lattice simulations in which the critical temperature T_c is found to be about 170MeV [17, 18]. The order of the transition is known to be dependent on the parameters of the QCD Lagrangian [19] and in a world such as ours with light "up" and "down" quarks and a "strange" quark with a mass similar to Λ_{QCD}, it is thought the QGP is reached via a crossover [20]. Heavy ion collision experiments such as those being carried out at the Relativistic Heavy Ion Collider (RHIC) are currently attempting to confirm the existence of the QGP.

Travelling along the $T = 0$ axis, one expects to reach a first-order transition between the vacuum and nuclear matter at $\mu \sim m_p/3$, i.e. when the chemical potential is sufficient to create a single nucleon. This is called the liquid-vapour transition [16, 21]. Further increasing μ, one should reach a transition when the chemical potential is significant enough for chirally symmetric quark matter to be energetically favourable; at high densities one expects a large Fermi sphere with degrees of freedom deep below the Fermi surface frozen by Pauli blocking [16]. The fact that neither of these first-order transitions are observed at $\mu = 0$ in lattice QCD with 2+1 flavours leads one to conclude that when continued into the $\mu - T$ plane, these transition lines should each reach some critical end point. Unfortunately, due to reasons we shall now discuss, it is currently impossible to confirm this picture directly by lattice simulation.

1.2 Lattice QCD at $\mu \neq 0$

The reason that exact lattice calculations cannot be extended to $\mu \neq 0$ is largely not physical in origin, but technical. When recast in Euclidean space-time, the quantum system can be represented statistically in terms of the partition function

$$\mathcal{Z} = \int \mathrm{d}U \mathrm{d}\overline{\psi} \mathrm{d}\psi e^{-S[U,\overline{\psi},\psi]}, \tag{1.3}$$

where $S = \sum_x \mathcal{L}_{\mathrm{QCD}}$ is the action written in terms of compact gauge fields $U = e^{iagA_\mu}$. Because U is an element of a compact gauge group, in this formulation there is no need to perform any gauge fixing and results can remain gauge invariant. In order to to be able to calculate (1.3), or related expectation values $\langle \mathcal{O} \rangle \equiv \frac{1}{\mathcal{Z}} \int \mathrm{d}U \mathrm{d}\overline{\psi} \mathrm{d}\psi \mathcal{O} e^{-S}$, one can explicitly integrate out the bilinear fermionic dependence leaving

$$\mathcal{Z} = \int \mathrm{d}U \det M e^{-S_g[U]}, \tag{1.4}$$

where S_g is the gauge contribution to the action and $M = (\not{D} + m_0)$ is the fermion kinetic matrix. Drawing on the direct correspondence between Euclidean quantum field theory and statistical mechanics, it is then possible to carry out the integral over gauge field configurations using Monte Carlo methods, in which the highly peaked nature of e^{-S} is exploited by using it as an importance sampling weight. This relies on the fact that $\not{D}$ is an anti-hermitian operator which obeys chiral symmetry, i.e. $[\not{D}, \gamma_5] = 0$ so that its imaginary eigenvalues $\pm i\lambda$ must come in complex conjugate pairs. Because $\not{D}$ is diagonalisable its determinant can be written as the product of these eigenvalues which must, therefore, be real. This means that one can use $\det \not{D} e^{-S_g}$ as the full functional weight, which remains real and highly peaked. This argument remains valid with the inclusion of bare quark masses, since the eigenvalues of $\not{D} + m_0$ are $m_0 \pm i\lambda$, which remain in conjugate pairs.

When a chemical potential is introduced, however, $M \to (\not{D} + m_0 + \mu\gamma_0)$, which is the sum of hermitian and anti-hermitian parts. This has, in general, complex eigenvalues making its determinant complex and the importance sampling weight becomes $|\det M|\, e^{i\theta} e^{-S_g}$. The complex phase can lead to configurations with large e^{-S_g} cancelling and the effectiveness of the importance sampling is suppressed. This suppression is parameterised by $\langle e^{i\theta} \rangle$, which is the ratio of partition functions with complex and real measure $\frac{\mathcal{Z}_{\text{comp}}}{\mathcal{Z}_{\text{real}}} = \exp(\mathcal{F}_{\text{comp}} - \mathcal{F}_{\text{real}})$, where $\mathcal{F}$ is the free energy of the partition function $\mathcal{Z}$. Since this is an extensive quantity, and $\mathcal{Z}_{\text{comp}} < \mathcal{Z}_{\text{real}}$, then $\langle e^{i\theta} \rangle \sim e^{-\alpha V}$, where α is some constant, and the suppression gets exponentially worse with increasing volume V; this is the notorious "sign problem". Recent advances mean that it is now possible to re-weight configurations generated at $\mu = 0$ into the $\mu - T$ plane and there are initial lattice predictions for the position of the critical end point

of the chiral phase transition [22, 23]. Results for the curve of the chiral transition analytically continued from imaginary chemical potential, where the sign problem does not occur, appear to be in agreement with these predictions [24]. These methods represent a significant step forward in the determination of the phase diagram of QCD, but because they require good overlap with the $\mu = 0$ configurations, one can only explore regions for which $\frac{\mu}{T} \lesssim 1$. Although this is sufficient to explore the chemical potentials reached at RHIC, where $\frac{\mu}{T} \sim 0.1$, these techniques cannot be extended to probe the rather complicated structure of the $\mu > T \sim 0$ region of the phase diagram relevant to the physics of compact stars. In order to do this we must still rely on results from models and effective field theories. It is this region of the phase diagram with which the work presented in this thesis is concerned.

1.3 Colour Superconductivity

At high chemical potential and low temperature, the ground-state of QCD could be described in terms of essentially free gluons and quarks with a Fermi surface at $E = E_F \approx \mu$. All fermion states below the Fermi Surface would be filled, and all states above would be vacant. If there is even a weak net attractive force between fermions in such a system, however, this state is unstable with respect to quark (hole) pairs with equal and opposite momenta above (below) the Fermi surface forming bound states and condensing out of the fermionic spectrum. This is analogous to the breaking of chiral symmetry by $q\bar{q}$ pairs condensing from the relativistic vacuum. This Cooper instability, described the Bardeen–Cooper–Schrieffer (BCS) theory, is the mechanism responsible for conventional superconductivity [25, 26]. The BCS ground-state is one with a distinct energy gap 2Δ in the dispersion relation about the Fermi surface from

where the Cooper pairs have condensed. This causes the gauge boson to become massive and leads to the Meissner effect. Because in QCD the formation of diquark pairs must necessarily break $SU(3)_c$ gauge invariance, this phenomenon is known as colour superconductivity (CSC) [27]. Perturbative studies of weak coupling expanded 2 flavour QCD at asymptotically high densities have shown this to be the ground-state, which is known as the 2SC phase. For a recent review of CSC see [28].

In a standard electrical superconductor, the BCS mechanism is a subtle one, since the fundamental interaction between electrons is repulsive; the net attractive interaction due to phonon exchange persists only at extremely low temperatures. In QCD, however, the fundamental interaction between quarks is attractive in the anti-triplet channel, meaning that diquark condensation should be more robust against thermal fluctuations. In recent years, studies of four-Fermi models with QCD instanton motivated interactions, have suggested that at $T = 0$ the BCS gap in the 2SC phase could be as large as 50-100MeV [29]. This means that a colour superconducting phase could be relevant to the physics of cold, dense compact stars where the typical temperature is only $\mathcal{O}(1\text{MeV})$ [30]. This study has inspired renewed interest in the field of colour superconductivity, with the existence of several new phases being proposed. One of these is observed in theories with 3 degenerate flavours, where it is thought that the high μ ground-state is one in which $SU(3)_c \otimes SU(3)_L \otimes SU(3)_R$ is broken to a combined $SU(3)_{c+L+R}$; this is known as the colour-flavour locked (CFL) phase [31]. In a world such as ours with $N_f = 2 + 1$, it has been proposed that this phase persists at high μ, whilst at intermediate μ it is separated by a phase transition from the chirally symmetric 2SC phase in which the strange quark would play a largely passive rôle [32].

Due to the persistence of the sign problem, none of these phases have been observed in lattice QCD. However, the non-perturbative simulation of model field theories can potentially provide the most robust treatment of colour superconducting matter at the intermediate densities relevant to the physics of compact stars. Two colour QCD is an interesting model that can be studied on the lattice, since in this theory $\det M(m_0, \mu \neq 0)$ is real [33]. At low chemical potential, the theory is described by a gas of weakly interacting bosonic diquark baryons, and therefore has no Fermi surface. At asymptotically high μ, however, asymptotic freedom suggests that quarks should be deconfined and may be in some 2SC-like state, which would be a superfluid rather than a superconductor, as in this theory the diquark does not break the $SU(2)$ colour gauge symmetry. This serves to illustrate the importance of a non-perturbative solution, as it is clear that some interesting physics should occur at some intermediate chemical potential. Lattice studies in recent years have shown that two colour QCD does exhibit superfluidity in the dense phase [34]. The behaviour of the superfluid is dominated by the nature of the low μ baryonic degrees of freedom, and superfluidity occurs via Bose-Einstein condensation in a manner analogous to He^4. Increasing the chemical potential further was found to saturate the lattice with the fundamental fermions before any deconfinement occurred.

In order to observe a BCS-style scenario, it seems one must resort to studying purely fermionic field theories such as the Nambu–Jona-Lasinio (NJL) model [35,36]. This model, discussed in detail in chapter 2, has no gauge degrees of freedom and all orders of gluon exchange are approximated by a four-fermion interaction.

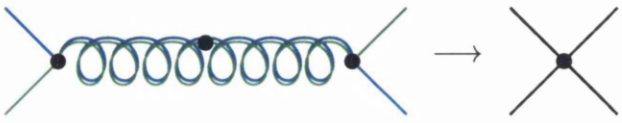

(1.5)

The original motivation for the formulation of this model was, however, that it observed the same global symmetries as strongly interacting matter and its vacuum structure exhibited chiral symmetry breaking in a manner directly analogous to BCS superconductivity. It is, therefore, an ideal model with which to study CSC in a relativistic quantum field theory. Previous lattice studies have been carried out in $2+1d$, since in this reduced dimensionality the theory is renormalisable and has the advantage of being computationally inexpensive to simulate. The $2+1d$ NJL model has both a rich and interesting phase diagram; at zero chemical potential and non-zero temperature the model exhibits spontaneous mass generation despite the lack of chiral symmetry breaking [37], whilst at low temperature and non-zero chemical potential the ground-state is that of a "thin film" superfluid, with long range phase coherence but no BCS gap generated about the Fermi surface [38]. These phenomena, largely due to the reduced dimensionality of the system, are not observed in self-consistent solutions, which serves to illustrate further the importance of a full non-perturbative treatment. To observe the BCS phase expected in QCD, it is necessary to extend the study carried out in [38] to a phenomenologically relevant $3+1$-dimensions.

This thesis contains results from a numerical study of the high μ, low T phase of the 3+1-dimensional NJL model, with the aim of showing that in a phenomenologically relevant dimensionality, the ground-state of this model is that of a conventional BCS superfluid formed in a manner analogous to superfluid He^3. In chapter 2 the continuum formulation of the model is presented along with its equivalent formulation on the lattice. Unfortunately, in $3+1d$ the model has no non-trivial continuum limit meaning it must be treated as an effective field theory with a definite cut-off a; the physics of the model is dependent on both the value of the cut-off and the

regularisation scheme employed. This issue was dealt with by fitting the model's free parameters using standard phenomenological techniques. In chapter 3, results from lattice simulations of the model with a diquark source j, which fixes the direction of symmetry breaking, show that in the limit that $j \to 0$ the high μ phase has a non-zero diquark condensate and a broken $U(1)$ baryon number symmetry. More direct evidence of diquark condensation is presented in chapter 4, where the high μ dispersion relation is shown to exhibit a clear gap $\Delta \neq 0$ about the Fermi surface, directly analogous to the BCS gap observed in low temperature superconductors.

The conclusions of both chapters 3 and 4 are reliant on discarding results with $j < 0.3$ in extrapolations to $j \to 0$. For these low values of j, there appears to be a discrepancy which is attributed to finite volume effects. This argument is explored in more detail in chapter 5. Finally, initial investigations of the persistence of the BCS phase with the introduction of non-zero isospin chemical potential and temperature are presented in chapter 6. The conclusion of this thesis is that there is clear non-perturbative evidence for the existence of a BCS superfluid phase in the $3+1d$ lattice NJL model, which gives a strong indication that there could be an analogous colour superconducting phase somewhere in the high density regime of QCD.

Chapter 2

The Nambu–Jona-Lasinio Model

2.1 NJL as a Model of QCD

The Nambu–Jona-Lasinio (NJL) model was first proposed in the early nineteen-sixties as a theory of the strong nuclear force, in which nuclei and mesons were formed via the four-Fermi contact interaction of a single fundamental spinor field [35,36]. Since this was prior to our knowledge of the existence of partons, these fundamental fermions were proposed to represent the nucleons. The physics of baryons and mesons is now known to be described well by Quantum Chromodynamics (QCD), in which the fundamental degrees of freedom are quarks and gluons. The fact that the theory exhibits asymptotic freedom allows its perturbative treatment at very high energies. As was discussed in the previous chapter, however, when not at asymptotically high energies the theory is strongly interacting and the ground-state is inherently non-perturbative, meaning that one must either find numerical solutions via lattice simulations or solve problems analytically using simple self-consistent models. For this reason, the NJL model, recast as a theory of interacting quarks, is still widely studied by nuclear theorists and phenomenologists as a simple model of QCD. Furthermore, the fact that the sign-problem renders lattice QCD insoluble at high density means that it is one

of only a few tools available with which to study CSC.

Although NJL is a relatively simple model, it does have some interesting properties which make it a suitable model of QCD. The first of these is that the model's symmetries and the patterns of their breaking are very similar to those of QCD. In Euclidean space, the Lagrangian density describing an NJL model with $N_f = 2$ quark flavours in the fundamental representation of $SU(2)$ can be written as

$$\mathcal{L} = \overline{\psi}^p \left(\not{\partial} + m_0\right) \tau_0^{pq} \psi^q - \frac{g^2}{2} \sum_{i=0}^{3} \left[\left(\overline{\psi}^p \tau_i^{pq} \psi^q\right)^2 + \left(\overline{\psi}^p i\gamma_5 \tau_i^{pq} \psi^q\right)^2 \right], \qquad (2.1)$$

where ψ and $\overline{\psi}$ are independent Grassmann-valued Dirac 4-spinors representing the quark fields, and m_0 is the the current-, or bare-mass of the quark. For $i = 1, 2, 3$, τ_i, are the 2×2 Pauli matrices which run over internal isospin or flavour degrees of freedom, and τ_0 is the unit matrix $\mathbb{1}_2$. In keeping with QCD, the fields ψ and $\overline{\psi}$ can have an additional N_c colour degrees of freedom, but since the model has no gauge fields, (2.1) is diagonal in the indices $\alpha = 1, \ldots, N_c$ and these have been suppressed. With this inclusion, the coupling before the interaction term becomes $\frac{-g^2}{2N_c}$. In the limit that $m_0 \to 0$, the Lagrangian (2.1) is invariant under independent $SU(2)$ axial and vector transformations corresponding to the conserved chiral and isospin currents

$$J_{5\mu}^k = \overline{\psi}\gamma_\mu\gamma_5\tau^k\psi, \qquad \partial_\mu J_{5\mu}^k\big|_{m_0\to 0} = 2im_0\overline{\psi}\tau^k\gamma_5\psi\big|_{m_0\to 0} = 0 \qquad (2.2)$$

and

$$J_\mu^k = \overline{\psi}\gamma_\mu\tau^k\psi, \qquad \partial_\mu J_\mu^k = 0. \qquad (2.3)$$

In order to physically interpret these symmetries we apply the operators $P_{L,R} = \frac{1}{2}(1 \pm \gamma_5)$ to ψ to project out left- and right-handed components. The symmetries (2.2) and (2.3) then become the invariance of left- and right-handed fermions under

the independent rotations

$$\psi_L \to U\psi_L, \quad \overline{\psi}_L \to \overline{\psi}_L U^\dagger; \quad \psi_R \to V\psi_R, \quad \overline{\psi}_R \to \overline{\psi}_R V^\dagger, \tag{2.4}$$

where U and V are elements of $SU(2)$. It is clear to see from (2.2) that the inclusion of a small bare quark mass $m_0 \neq 0$ explicitly breaks the $SU(2) \otimes SU(2)$ symmetry down to the $SU(2)_V$ of isospin, with the $SU(2)_A$ remaining only approximate. For a strong enough coupling $g^2 > g_c^2$, this approximate symmetry is spontaneously broken in the vacuum, as happens in nature. This leads to the creation of an approximate Goldstone mode, the pion, which becomes massless only when $m_0 \equiv 0$. The symmetry (2.3) is broken if the bare masses of the 2 quark flavours are made non-degenerate by replacing the $\overline{\psi}\tau_0 m_0 \psi$ term in (2.1) with e.g. $\overline{\psi}\begin{pmatrix} m_u & 0 \\ 0 & m_d \end{pmatrix}\psi$. In nature this is again an approximate symmetry as $m_u \approx m_d$, so for simplicity we keep the two flavours degenerate. The model is also invariant under the axial and vector $U(1)$ rotations

$$\psi \to e^{i\alpha\gamma_5}\psi, \quad \overline{\psi} \to e^{-i\alpha\gamma_5}\overline{\psi} \tag{2.5}$$

and

$$\psi \to e^{i\beta}\psi, \quad \overline{\psi} \to e^{-i\beta}\overline{\psi} \tag{2.6}$$

respectively. The vector symmetry (2.6) manifests itself in nature as the conservation of baryon number and hence we label it $U(1)_B$. When the NJL model was first written down, it was noted that there was no evidence in nature for a conserved $U(1)_A$ symmetry in (2.5) and no Goldstone boson related to its spontaneous breaking, so the model was altered to a form in which this was no longer a good symmetry [36]. It is interesting to note that the original form does have the same global symmetries as the Lagrangian of QCD with 2 degenerate quark flavours, and that the reason that $U(1)_A$ is not observed in nature is that it is anomalous, i.e. it is not a good symmetry in the

full quantum theory. This was found to be due to the effects of QCD instantons [5,6]. We therefore choose to study the form proposed in [36]

$$\mathcal{L} = \overline{\psi}^p \left(\partial\!\!\!/ + m_0\right) \tau_0^{pq} \psi^q - \frac{g^2}{2N_c} \left[\left(\overline{\psi}^p \tau_0^{pq} \psi^q\right)^2 + \left(\overline{\psi}^p i\gamma_5 \vec{\tau}^{pq} \psi^q\right)^2 \right], \tag{2.7}$$

where $\vec{\tau} \equiv (\tau_1, \tau_2, \tau_3)$ is a vector of the Pauli matrices. In this form the model has exactly the same global symmetries as full QCD, i.e. $SU(2)_L \otimes SU(2)_R \otimes U(1)_B$.

Another interesting property of the model is that, by design, it describes both "baryon" and "meson" degrees of freedom, corresponding to the fundamental quark ψ and bound $\psi\overline{\psi}$ states. Most importantly, although the "baryons" are not bound-states, being fermionic they do obey the correct statistics. This means that increasing the chemical potential from zero, it is possible to build up a Fermi surface, and observe related phenomena, such as the formation of a BCS gap $\Delta \neq 0$. However, since the broken $U(1)_B$ symmetry associated with the formation of the gap is global rather than a gauge symmetry, the NJL analogue of a CSC state is not a superconductor, but a superfluid analogous to ^{3}He. By contrast, the baryons in 2-colour QCD, being bound-states of two quarks are bosonic and no Fermi surface can build up. Although diquark condensation still occurs, the gauge invariant qq pairs form via Bose-Einstein condensation and the result is a superfluid, this time analogous to ^{4}He [33, 34, 39].

The two major drawbacks of the NJL model come from the fact that the only interactions are via four-Fermion terms. Due to the point-like nature of the four-Fermi interaction, the NJL model is non-renormalisable for a number of dimensions $d \geq 4$ [40, 41]. One approach to bypass this is to formulate the model in a reduced dimensionality, where theory can be normalised and becomes well-defined [42, 43]. Lattice simulations of the $2+1d$ model, however, have shown the ground-state of the

high-μ phase to be a "thin-film" superfluid with long range coherence, but no mass-gap generated about the Fermi surface [38]. This interesting phase is an artifact of the low dimensionality, implying that in order to draw information about QCD from this model we need to study a physically relevant $3+1d$. We are forced, therefore, to deal with the model's non-renormalisability. This can be overcome by the introduction of either an infinite number of counter-terms in the Lagrangian, or a new regularisation scale for each quantity to be calculated. In practice though, this severely reduces the model's predictive power and it is physically more sensible to associate the interaction with a single scale, the UV cut-off Λ. The model must then be treated as an effective field theory, in which not only the values of physical quantities calculated, but possibly the nature of the ground-state and the order of any phase transitions are dependent on the regularisation scheme employed [41]. In order to ensure that the scheme chosen is sensible, one must therefore match the model's parameters to low-energy, vacuum phenomenology. This is done in section 2.5.

The second problem with the model is that the theory contains no gauge fields to play the rôleof the gluons. i.e. quarks are not confined in any phase of the theory. Not only can free quarks can be created in the vacuum, but once the chemical potential is increased from zero, there is no nuclear matter phase for the model to enter. Bag model arguments suggest that a bag constant of $B^{1/4} \gtrsim 170\text{MeV}$ is required for nuclear matter to be stable [16], whilst in the NJL model $B^{1/4} \approx 0$. Instead the model passes straight from the vacuum to the chirally restored phase. This is not a problem if one limits oneself to studying the symmetry properties of the theory and does not interpret any information as to the order of this phase transition phenomenologically.

Despite this limitation, whilst lattice simulation of dense QCD remains elusive,

the NJL model is the most powerful tool available to probe the statistical behaviour of dense quark systems. Furthermore, the fact that previous lattice simulations of the $2+1d$ model have exposed a non-perturbative ground-state points out the potential importance of fully non-perturbative treatment of even simple models in attempts to understand CSC. It is with this motivation in mind, that the analysis in [38] has been extended to the NJL model in $3+1$ dimensions.

In the rest of this chapter, we discuss the additions to the model necessary to calculate quantities at non-zero μ, the formulation of the model on a discrete space-time lattice and how the continuum limit of this model differs from the standard NJL model. Finally we outline the method chosen for fixing the model's free parameters.

2.2 Additions to the Standard Model

In order to introduce a chemical potential μ to fermionic field theories, a standard term $\mathcal{L}_\mu = \mu\overline{\psi}\gamma_0\psi$ is added to the Lagrangian. The origin of the form of this term can be easily understood by noting that in Minkowski space, $\overline{\psi}\gamma_0\psi \sim \psi^\dagger\psi$, which in the canonical formulation of quantum field theory is the quark number operator N_q. The parameter μ can be seen as a source for this operator, making the creation of fermions energetically more favourable than anti-fermions, and enters the partition function $\sim e^{-\mu N_q}$ in the standard way.

The second addition to the model is the introduction of auxiliary scalar and pseudo-scalar fields, situated at the four-Fermi interaction and denoted by σ and $\vec{\pi}$ respectively. This "bosonisation" makes the model considerably easier to treat,

both numerically and analytically. The bosonised Lagrangian is

$$\begin{aligned}\mathcal{L} &= \overline{\psi}\left(\not{\partial} + m_0 + \mu\gamma_0 + \sigma + i\gamma_5\vec{\pi}.\vec{\tau}\right)\psi + \frac{N_c}{2g^2}\left(\sigma^2 + \vec{\pi}.\vec{\pi}\right) \\ &= \overline{\psi}\left(\not{\partial} + m_0 + \mu\gamma_0 + \sigma + i\gamma_5\vec{\pi}.\vec{\tau}\right)\psi + \frac{N_c}{4g^2}\mathrm{Tr}\Phi^\dagger\Phi, \end{aligned} \tag{2.8}$$

where the combination $\Phi \equiv \sigma + i\vec{\pi}.\vec{\tau}$ is proportional to an element of the chiral group such that (2.8) is invariant under the rotation $\Phi \to V\Phi U^{-1}$. Functionally integrating (2.8) over Φ one retrieves the purely fermionic NJL Lagrangian.

2.3 The Lattice Model

The work presented in this thesis has been carried out utilising the methods of lattice field theory, in which we replace the space-time continuum with a discrete 4-dimensional lattice, with each site separated from its nearest neighbours by the lattice spacing a. This has the effect of introducing an ultra-violet (UV) cut-off $\Lambda \sim a^{-1}$, which regularises any divergences and makes the theory mathematically well-defined. The fact that the cut-off is imposed before any expansions or approximations are made means that this regularisation method can be used to study strongly-interacting field theories in a fully non-perturbative manner. We define fermion fields on lattice sites x and bosonic fields on sites $\tilde{x}$ of a dual lattice translated from the original lattice by $(\frac{1}{2}, \frac{1}{2}, \frac{1}{2}, \frac{1}{2})$. Space-time integrals and differentials are replaced by sums and finite differences respectively such that in the formalism of staggered fermions,[1] the action for a non-interacting quark

$$S = \int \mathrm{d}^4x\overline{\psi}(\not{\partial} + m_0)\psi \tag{2.9}$$

[1]For a discussion on staggered fermions and their interpretation see Appendices A.1 and A.2.

becomes

$$S = \sum_x a^4 \left\{ \frac{1}{2a} \sum_{\nu=0}^{3} \eta_\nu(x) \left[(\overline{\chi}_x \chi_{x+\hat{\nu}}) - (\overline{\chi}_x \chi_{x-\hat{\nu}}) \right] + m_0 \left(\overline{\chi}_x \chi_x \right) \right\}, \tag{2.10}$$

where $\overline{\chi}$ and χ are Grassmann-valued staggered quark fields and $\eta_\nu(x)$ is the Kawamoto-Smit phase

$$\eta_\nu(x) = \begin{cases} 1 & \nu = 0 \\ (-1)^{x_0 + \ldots + x_{\nu-1}} & \nu = 1, 2, 3. \end{cases} \tag{2.11}$$

The fact that when evaluating quantities numerically, computer memory must be allocated for each field to be defined on each lattice site, forces the theory to be defined on a finite volume V. It is necessary, therefore, to define boundary conditions for the fields. We choose bosonic fields to be periodic in all directions, whilst fermionic fields are set to be periodic in spatial directions and anti-periodic in time, as this choice allows the trace of an operator to be identified with the Grassmann functional integral and enforces the correct statistical behaviour [44].

When formulated on the lattice, the action of the bosonised NJL model (2.8) with $\mu = 0$ is

$$S = a^4 \sum_x \left[\overline{\chi} M \left[\sigma, \vec{\pi} \right] \chi + \overline{\zeta} M^* \left[\sigma, \vec{\pi} \right] \zeta \right] + \frac{2a^4}{g^2} \sum_{\tilde{x}} \left(\sigma^2 + \vec{\pi}.\vec{\pi} \right), \tag{2.12}$$

where $M\left[\sigma, \vec{\pi}\right]$ is the fermion kinetic operator

$$\begin{aligned} M^{pq}_{xy}[\sigma, \vec{\pi}] &= \frac{1}{2a} \delta^{pq} \sum_{\nu=0}^{3} \eta_\nu(x) \left(\delta_{yx+\hat{\nu}} - \delta_{yx-\hat{\nu}} \right) + \delta^{pq} \delta_{yx} m_0 \\ &+ \frac{1}{16} \delta_{xy} \sum_{\langle \tilde{x}, x \rangle} \left(\sigma(\tilde{x}) \delta^{pq} + i\epsilon(x) \vec{\pi}(\tilde{x}).\vec{\tau}^{pq} \right), \end{aligned} \tag{2.13}$$

$\langle \tilde{x}, x \rangle$ represents the sum over the set of 16 dual lattice sites neighbouring x and $\epsilon(x) = (-1)^{x_0 + \ldots + x_3}$ is the staggered representation of γ_5 . p, q are the internal $SU(2)$ isospin indices, which we include explicitly. The extra fermionic degrees of freedom $\overline{\zeta}$

and ζ arise due to the fact that in our simulation we use $\det M^\dagger M$ rather than $\det M$ in the functional weight, which is discussed further in section 3.1.

When introducing a chemical potential on the lattice one does not do so with a term $a\mu\overline{\chi}\gamma_0\chi$, since even for free fermions, this leads to quadratic divergences [45]. The reason for this can be understood by observing that in Euclidean space, the chemical potential acts like the zeroth component of a constant imaginary vector potential, and therefore needs to be introduced in a "gauge-invariant" way. The correct solution is to introduce μ into the zeroth derivative by multiplying the forward time difference by $e^{a\mu}$ and the backward time difference by $e^{-a\mu}$. With this addition the kinetic operator becomes

$$\begin{aligned} M_{xy}^{pq} &= \frac{1}{2a}\delta^{pq}\left[\left(e^{a\mu}\delta_{yx+\hat{0}} - e^{-a\mu}\delta_{yx-\hat{0}}\right) + \sum_{\nu=1}^{3}\eta_\nu(x)\left(\delta_{yx+\hat{\nu}} - \delta_{yx-\hat{\nu}}\right) + 2am_0\delta_{xy}\right] \\ &+ \frac{1}{16}\delta_{xy}\sum_{\langle\tilde{x},x\rangle}\left(\sigma(\tilde{x})\delta^{pq} + i\epsilon(x)\vec{\pi}(\tilde{x}).\vec{\tau}^{pq}\right). \end{aligned} \tag{2.14}$$

Finally, we consider the effect that formulation on a finite volume has on spontaneous symmetry breaking. Goldstone's theorem implies that the spontaneous breaking of a continuous global symmetry must correspond to the creation of a massless mode and, therefore, to a divergence in the correlation length. Once the correlation length ξ is comparable to the size of the lattice L, it can diverge no more, meaning only a finite amount of energy is required to change the direction of symmetry breaking. This allows the direction of symmetry breaking to change from configuration to configuration and causes the order parameter of the symmetry to remain zero. This is a standard problem in the study of spin systems and chiral symmetry breaking, and can be overcome by the introduction of explicit symmetry-breaking terms to the Lagrangian. These terms have the effect of fixing the direction of symmetry breaking

and keeping $\xi \ll L$ for sufficiently large L. It is in this vein that we introduce diquark sources j and $\bar{j}$, analogous to Majorana masses, in a way that explicitly breaks the $U(1)_B$ symmetry. In order to ascertain if the symmetry is spontaneously broken, one can then study observables, such as the order parameter, in the limit that the symmetry breaking terms are reduced to zero. A convenient way to do this is to write the action in terms of the bispinors $\Psi^{\mathrm{tr}} = (\overline{\chi}, \chi^{\mathrm{tr}})$ and $\Upsilon^{\mathrm{tr}} = (\overline{\zeta}, \zeta^{\mathrm{tr}})$

$$S = a^4 \sum_x \left[\Psi^{\mathrm{tr}} \mathcal{A}[\sigma, \vec{\pi}]\Psi + \Upsilon^{\mathrm{tr}} \mathcal{A}^*[\sigma, \vec{\pi}]\Upsilon\right] + \frac{2a^4}{g^2} \sum_{\tilde{x}} (\sigma^2 + \vec{\pi}.\vec{\pi}), \tag{2.15}$$

where the antisymmetric Nambu-Gor'kov matrix $\mathcal{A}$ is

$$\mathcal{A}^{pq}_{xy} = \frac{1}{2} \begin{pmatrix} \bar{j}\tau_2^{pq}\delta_{xy} & M^{pq}_{xy} \\ -M^{qp}_{yx} & j\tau_2^{pq}\delta_{xy} \end{pmatrix}. \tag{2.16}$$

Looking at (2.15) it is interesting to note that although the lattice formulation necessarily breaks Poincaré-invariance, by making the replacement $\gamma_5 \to \epsilon(x)$ such that projection operators $P_{L,R} \to P_{e,o} = \frac{1}{2}(1 \pm \epsilon(x))$ now project onto even and odd sublattices respectively, the other symmetries defined in section 2.1 are still observed. In particular the $SU(2) \otimes SU(2)$ chiral symmetry remains exact [46], which is not the case in lattice QCD.

2.4 Continuum Limit of the Lattice Model

The non-renormalisability of the $3 + 1d$ NJL model corresponds, on the lattice, to there being no interacting continuum limit. It is illuminating, however, to write down the continuum form of the lattice model (2.15) and compare it with the model described in sections 2.1 and 2.2.

As is discussed in appendix A.1, the staggered quark approach reduces the number of degrees of freedom of naïve lattice quarks by a factor of 4. This is done by

diagonalising the theory in spinor indices and disregarding all but one component. A continuum interpretation is then made by carrying out the unitary transformations outlined in appendix A.2 to fields q and $\overline{q}$ defined on sites y of a blocked lattice, after which, in 4 dimensions, the remaining 16 "doublers" are interpreted as 4 "flavours" of 4-spinor, each with a pole at $k^2 = 0$ only. We interpret these extra "flavour" degrees of freedom as colours. In this basis the kinetic term becomes

$$\begin{aligned} S_{\text{kin}} = \; a^4 16 \textstyle\sum_y \overline{q} \Big[\frac{1}{a} \sum_\mu \{ \Delta_\mu (\gamma_\mu \otimes \mathbb{1}_2 \otimes \mathbb{1}_4 \otimes \mathbb{1}_2) - \delta_\mu (\gamma_5 \otimes \mathbb{1}_2 \otimes t_5 t_\mu \otimes \mathbb{1}_2) \} \\ + m_0 (\mathbb{1}_4 \otimes \mathbb{1}_2 \otimes \mathbb{1}_4 \otimes \mathbb{1}_2) \Big] q, \end{aligned} \tag{2.17}$$

where $t_\mu \equiv \gamma_\mu^*$ and the two differences Δ_μ and δ_μ (defined in appendix A.2) tend to $a\partial_\mu$ and $a^2\partial_\mu^2$ respectively in the continuum limit. In the tensor products, the first matrix acts on spinor, the second on flavour or isospin and the third and fourth on colour degrees of freedom. The fourth matrix, in which the action is diagonal, represents the degeneracy in the χ and ξ fields making the number of colours in the model $N_c = 8$. For brevity, we suppress this matrix in the rest of this section. The diquark term becomes

$$S_{\text{diq}} = a^4 16 \sum_y \left[\frac{j}{2} q^{\text{tr}} (C\gamma_5 \otimes \tau_2 \otimes t_5 C^*)\, q + \frac{\bar{j}}{2} \overline{q} (C\gamma_5 \otimes \tau_2 \otimes t_5 C^*)\, \overline{q}^{\text{tr}} \right], \tag{2.18}$$

where $C \equiv \gamma_4\gamma_2 = -\gamma_1\gamma_3\gamma_5$ is the charge conjugation operator, which satisfies

$$\begin{aligned} C\gamma_\mu C^{-1} &= -\gamma_\mu^*, \\ -C = C^{\text{tr}} &= C^{-1} = C^*. \end{aligned} \tag{2.19}$$

In order to treat the interaction term between the fermions and the auxiliary fields, we label the dual lattice $(x + \frac{1}{2}, x + \frac{1}{2}, x + \frac{1}{2}, x + \frac{1}{2})$ by $(A; \tilde{y})$, where x corresponds to

$(A;y)$. We then treat each part of the sum over A independently, resulting in

$$S_{\rm int} = a^4 \sum_y \sum_A \left[\sigma(A;\tilde{y})\overline{q}\,(\mathbb{1}_4 \otimes \mathbb{1}_2 \otimes \mathbb{1}_4)\,q + \overline{q}i\,(\gamma_5 \otimes \vec{\tau}.\vec{\pi}(A;\tilde{y}) \otimes t_5)\,q\right] + \mathcal{O}(a). \tag{2.20}$$

Finally, taking the continuum limit, i.e. $a \to 0$, and including the purely bosonic part, the continuum action becomes

$$\begin{aligned} S_{\rm cont} \;=\; & \int \mathrm{d}^4x \Big\{ \overline{\psi}\,(\partial\!\!\!/ + m_0 + \mu\gamma_0)\,\psi + \overline{\psi}\,[(\mathbb{1}_4 \otimes \sigma\mathbb{1}_2 \otimes \mathbb{1}_4) + i\,(\gamma_5 \otimes \vec{\tau}.\vec{\pi} \otimes t_5)]\,\psi \\ & + \frac{1}{2}\left[j\left(\psi^{\rm tr} C\gamma_5 \otimes \tau_2 \otimes t_5 C^* \psi\right) + \bar{\jmath}\left(\overline{\psi} C\gamma_5 \otimes \tau_2 \otimes t_5 C^* \overline{\psi}^{\rm tr}\right)\right] \Big\} \\ & + \frac{4}{g^2}\mathrm{Tr}\Phi^\dagger\Phi, \end{aligned} \tag{2.21}$$

which in the limit $j, \bar{\jmath} \to 0$, is equivalent to the original model (2.8).

2.5 Phenomenological Parameter Choice

In this section we discuss the method for fitting the model's free parameters to low energy vacuum phenomenology. Since the lattice model has no interacting continuum limit, one must choose a fixed lattice spacing $a \sim 1/\Lambda$, corresponding to a fixed coupling constant β. Employing methods outlined in [41] we calculate the ratio between the pion decay rate f_π and the constituent quark mass m^*, i.e. the mass of the quark in the chirally broken phase. By fitting to phenomenological values one may then extract β as a function of the model's only other free parameter, the bare quark mass m_0. Finally, calculating and fitting the pion mass m_π allows one to fix m_0, and hence β. We take advantage of the fact that a perturbative expansion in $1/N_c$ is possible in four-Fermi theories by calculating quantities analytically to leading order in $1/N_c$, the Hartree approximation. Feynman diagrams are evaluated using staggered quark propagators defined on an $L_s^3 \times L_t/2^4$ Euclidean blocked lattice with periodic

boundary conditions in spatial dimensions and anti-periodic boundary conditions in the temporal dimension. In this scheme the Feynman rules of the model are:

(a) Draw all topologically distinct, connected diagrams to the desired order in $1/N_c$;

(b) In each diagram attach a staggered quark propagator to each internal line

$$\begin{aligned} \xrightarrow{k} \quad = \quad & \frac{-\frac{i}{2a}\sum_{\mu}\sin 2ak_{\mu}\left(\gamma_{\mu}\otimes\mathbb{1}_2\otimes\mathbb{1}_4\otimes\mathbb{1}_2\right)}{\sum_{\nu}\sin^2 ak_{\nu}+\left(am^*\right)^2} \\ & + \frac{\frac{1}{2a}\sum_{\mu}\left(1-\cos 2ak_{\mu}\right)\left(\gamma_5\otimes\mathbb{1}_2\otimes t_5t_{\mu}\otimes\mathbb{1}_2\right)}{\sum_{\nu}\sin^2 ak_{\nu}+\left(am^*\right)^2} \\ & + \frac{m^*\left(\mathbb{1}_4\otimes\mathbb{1}_2\otimes\mathbb{1}_4\otimes\mathbb{1}_2\right)}{\sum_{\nu}\sin^2 ak_{\nu}+\left(am^*\right)^2}; \end{aligned} \tag{2.22}$$

(c) For each four-Fermi interaction multiply by

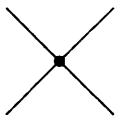

$$= \begin{cases} \frac{g^2}{4} & \text{Scalar} \\ i\gamma_5\tau_i\frac{g^2}{4}i\gamma_5\tau_j & \text{Pseudoscalar;} \end{cases} \tag{2.23}$$

(d) At each inner vertex enforce momentum conservation modulo π/a, since the fact that the lattice spacing on the blocked lattice is $2a$ limits the momentum range of the staggered quark to $-\frac{\pi}{2} \leq p_{\mu} \leq \frac{\pi}{2}$;

(e) For each internal momentum k not fixed by momentum conservation at the vertices insert a factor $\int_{-\pi/2a}^{\pi/2a}\frac{\mathrm{d}^4p}{(2\pi)^4}$;

(f) For each closed loop multiply by a factor (-1) and impose a trace over the fermion's degrees of freedom;

(g) Multiply the contribution for each diagram by

(i) a factor of (-1) between graphs which differ from each other only by an interchange of two external lines;

(ii) a symmetry factor to take the combinatorics of the diagram into account.

The momentum loop integrals were evaluated over discrete mode sums on increasing volumes V until the effect of increasing V was found to be negligible.

Let us first calculate the gap equation, the fermion self-interaction, to leading order in $1/N_c$. For sufficiently strong coupling $g^2 > g_c^2$ the scalar auxiliary field σ develops a spontaneous vacuum expectation value Σ, which in the chiral limit can be identified with the constituent fermion mass and is given by

$\Sigma =$ 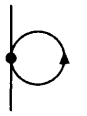 $= \frac{N_c N_f m^*}{\beta} \int_{\frac{-\pi}{2}}^{\frac{\pi}{2}} \frac{\mathrm{d}^4 p}{(2\pi)^4} \frac{1}{\sum_\mu \sin^2 p_\mu + (am^*)^2}, \qquad (2.24)$

where N_c and N_f are the number of flavours and colours respectively, and $\beta = a^2/g^2$ is the dimensionless inverse coupling constant.

Now let us calculate the dimensionless ratio between the pion decay rate f_π and the constituent quark mass m^*. f_π is calculated from the vacuum to one-pion axial-vector matrix element

$\langle 0 | J_{i5\mu}(k) | \pi_j \rangle = i\gamma_\mu\gamma_5 \frac{\tau_j}{2}$ 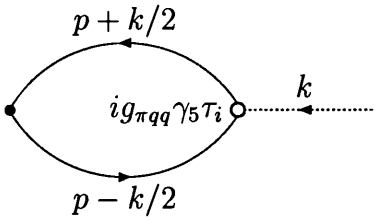

. $\qquad (2.25)$

Translating this diagram we yield

$$if_\pi \delta_{ij} \sin k_\mu = \frac{g_{\pi qq}}{2} \int_{-\frac{\pi}{2}}^{\frac{\pi}{2}} \frac{\mathrm{d}^4 p}{(2\pi)^4} \mathrm{Tr}\gamma_\mu\gamma_5 S\left(p^+\right) \gamma_5 S\left(p^-\right) \delta_{ij}, \qquad (2.26)$$

where the momenta $p^{\pm} = p \pm k/2$. Factors of the lattice spacing a have been suppressed. Having carried out the trace over colour, flavour and spinor labels we divide (2.26) by the constituent quark mass m^* to find the desired ratio

$$\frac{f_\pi}{m^*} = \frac{g_{\pi qq} N_c N_f}{2m^*} \int_{-\frac{\pi}{2}}^{\frac{\pi}{2}} \frac{\mathrm{d}^4 p}{(2\pi)^4} \frac{\sum_\mu \cos 2p_\mu}{\left[\sum_\nu \sin^2 p_\nu^+ + m^{*2}\right]\left[\sum_\rho \sin^2 p_\rho^- + m^{*2}\right]}, \tag{2.27}$$

where $g_{\pi qq}$ represents the pion-to-quark-quark coupling strength.

In order to obtain a functional form for $g_{\pi qq}$ let us investigate the nature of the pion propagator in this model. To leading order in $1/N_c$ the effective interaction can be expressed as an infinite sum of "bubble" diagrams in the random-phase approximation, i.e. the pion is approximated as a single quark-antiquark pair with no internal isospin-changing interactions. The scattering of two quarks via pion exchange is illustrated diagrammatically in Fig. 2.1.

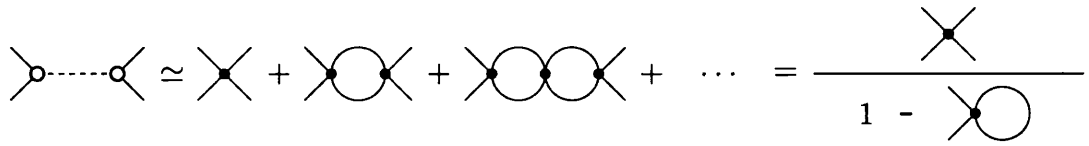

Figure 2.1: Feynman diagram of quark scattering via pion-exchange to leading order in the $1/N_c$ expansion.

Using the Feynman rules the diagram becomes

$$g_{\pi qq} S_\pi(k) g_{\pi qq} = \gamma_5 \tau_i \left[\frac{g^2}{4} + \frac{g^2}{4}\Pi_{\mathrm{ps}}\frac{g^2}{4} + \frac{g^2}{4}\Pi_{\mathrm{ps}}\frac{g^2}{4}\Pi_{\mathrm{ps}}\frac{g^2}{4} + \ldots\right]\gamma_5 \tau_j \tag{2.28}$$

$$= \gamma_5 \tau_i \left[\frac{g^2}{4 + g^2 \Pi_{\mathrm{ps}}}\right]\gamma_5 \tau_j, \tag{2.29}$$

where $\Pi_{\rm ps}$ is the vacuum polarisation of the pion. Diagrammatically

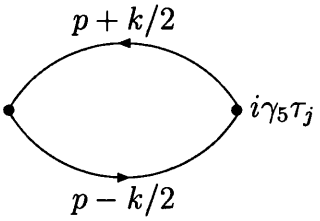

, (2.30)

which is written as

$$\Pi_{\rm ps}\left(\tilde{k}^2\right) = -N_c N_f \int_{-\frac{\pi}{2}}^{\frac{\pi}{2}} \frac{\mathrm{d}^4 p}{(2\pi)^4} \frac{1}{\left[\sum_\nu \sin^2 p_\nu^+ + m^{*2}\right]\left[\sum_\rho \sin^2 p_\rho^- + m^{*2}\right]} \times \left(\sum_\mu \left[\sin 2p_\mu^+ \sin 2p_\mu^- + \left(1 - \cos 2p_\mu^+\right)\left(1 - \cos 2p_\mu^-\right)\right] + 4m^{*2}\right), \quad (2.31)$$

where $\tilde{k}^2 = \sum_{\mu=0}^{3} \sin^2 a k_\mu$ is the effective squared-pion-momentum in units of a^2. In order to bring this into a form more easily manageable one can rewrite the denominator of the integrand in terms of the partial fractions

$$\frac{1}{\left(1 - \sum_\nu \cos 2p_\nu \cos k_\nu + 2m^{*2}\right)} \left(\frac{1}{\sum_\mu \sin^2 p_\mu^+ + m^{*2}} + \frac{1}{\sum_\rho \sin^2 p_\rho^- + m^{*2}}\right) \quad (2.32)$$

and the numerator as

$$2\sum_\mu \left[1 - \cos 2p_\mu \cos k_\mu - \sin^2 k_\mu\right] + 4m^{*2}. \quad (2.33)$$

It is then possible to show that (2.31) becomes

$$\Pi_{\rm ps}\left(\tilde{k}^2\right) = 2N_c N_f \sum_\nu \sin^2 k_\nu I(\tilde{k}^2) - 2N_c N_f \int_{-\frac{\pi}{2}}^{\frac{\pi}{2}} \frac{\mathrm{d}^4 p}{(2\pi)^4} \left[\frac{1}{\sum_\mu \sin^2 p_\mu^+ + m^{*2}} + \frac{1}{\sum_\mu \sin^2 p_\mu^- + m^{*2}}\right], \quad (2.34)$$

where the integral $I(\tilde{k}^2)$ is given by

$$I(\tilde{k}^2) = \int_{-\frac{\pi}{2}}^{\frac{\pi}{2}} \frac{\mathrm{d}^4 p}{(2\pi)^4} \frac{1}{\left[\sum_\mu \sin^2 p_\mu^+ + m^{*2}\right]\left[\sum_\rho \sin^2 p_\rho^- + m^{*2}\right]}. \quad (2.35)$$

By making shifts in the loop momenta the second and third terms of (2.34) are seen to be proportional to the gap equation (2.24) leaving

$$\Pi_{\rm ps}\left(\tilde{k}^2\right) = -4\left(\frac{m^* - m_0}{m^* g^2}\right) + 2N_c N_f \tilde{k}^2 I(\tilde{k}^2). \tag{2.36}$$

Expanding (2.29) about the pole at $\tilde{k}^2 = -(am_\pi)^2$, again with a suppressed, we find

$$g_{\pi qq} S_\pi(k) g_{\pi qq} \simeq \gamma_5 \tau_i \frac{\left(\partial\Pi_{\rm ps}/\partial\tilde{k}^2\right)^{-1}}{\tilde{k}^2 + m_\pi^2} \gamma_5 \tau_j, \tag{2.37}$$

from which we may deduce

$$g_{\pi qq}^2 = \left(\frac{\partial\Pi_{\rm ps}}{\partial\tilde{k}^2}\right)^{-1}\Bigg|_{\tilde{k}^2 = -m_\pi^2}. \tag{2.38}$$

In the vacuum, the pion is an approximate Goldstone mode which means that it is a good approximation to evaluate $\partial\Pi_{\rm ps}/\partial\tilde{k}^2$ in the chiral limit, i.e. at $\tilde{k}^2 = -m_\pi^2 = 0$. This yields the particularly simple form

$$g_{\pi qq}^{-2} = 2N_c N_f \int_{-\frac{\pi}{2}}^{\frac{\pi}{2}} \frac{\mathrm{d}^4 p}{(2\pi)^4} \frac{1}{\left[\sum_\mu \sin^2 p_\mu + m^{*2}\right]^2}. \tag{2.39}$$

Finally, by substituting this into (2.27), setting the momentum of the pion to zero, and reintroducing the lattice spacing a, the ratio between f_π and m^* is found to be

$$\frac{f_\pi}{m^*} = \frac{\sqrt{2N_c N_f}\displaystyle\int_{-\frac{\pi}{2}}^{\frac{\pi}{2}} \frac{\mathrm{d}^4 p}{(2\pi)^4} \frac{\cos 2p_\nu}{\left[\sum_\mu \sin^2 p_\mu + (am^*)^2\right]^2}}{\left\{\displaystyle\int_{-\frac{\pi}{2}}^{\frac{\pi}{2}} \frac{\mathrm{d}^4 p}{(2\pi)^4} \frac{1}{\left[\sum_\rho \sin^2 p_\rho + (am^*)^2\right]^2}\right\}^{\frac{1}{2}}}. \tag{2.40}$$

In order to check that this form is sensible we choose to examine the continuum limit by extracting the leading-order behaviour of (2.40) as the dimensionless quark

mass am^* is reduced to zero. This is done by the introduction of a hyper-spherical cut-off δ which splits the loop momenta into two regions, one with $|p| > \delta$ and the other with $|p| \leq \delta$. As $\delta \to 0$, the inner hyper-spherical region picks up all of the leading order continuum behaviour whilst the outer region contains the small terms relevant to lattice perturbation theory [47]. Ignoring these terms and taking $am^* \to 0$ we pick up the leading order behaviour of (2.40), namely $f_\pi/m^* \sim \sqrt{N_c N_f/4\pi^2}\ln(\delta/am^*)$. Although this quantity is logarithmically divergent, we know that the integral between $\pi/2a$ and $-\pi/2a$ is finite and independent of δ, and that the transition between the two regions of integration is smooth. This means that the $\ln\delta$ term must be cancelled out by a similar term in the outer region leaving the leading-order continuum behaviour of f_π/m^* to be

$$\frac{f_\pi}{m^*} \sim \sqrt{\frac{N_c N_f}{(2\pi)^2}\ln\frac{1}{am^*}}. \tag{2.41}$$

This is the same leading order behaviour that is found for the regularisation schemes employed in [41], namely $3d$-momentum, $4d$-momentum and real-time cut-offs as well as the Pauli-Villars scheme.

By calculating (2.40) in the infinite volume limit and fitting f_π to its experimental value of 93MeV and m^* to a reasonable 400MeV we are able to extract the dimensionless quark mass $am^* = 0.557$, meaning that to leading in $1/N_c$ the lattice spacing $a = (720\text{MeV})^{-1} \sim 0.3\text{fm}$. Solving the gap equation (2.24) with this value for the mass we find that $a\beta\Sigma = 0.2730$, and using the identity that $m^* \equiv m_0 + \Sigma$ we are able to deduce a relationship between the bare quark mass and the inverse-coupling

$$\beta = \frac{0.273}{(0.557 - am_0)}. \tag{2.42}$$

Finally, in order to fix the bare quark mass and hence the coupling constant, we need to fit to one more phenomenological observable. Again following [41], we calculate

the mass of the pion m_π by identifying the poles in equations (2.29) and (2.37),

$$\begin{aligned} 0 &= 4 + \left.\frac{\Pi_{ps}(\tilde{k}^2)}{\beta}\right|_{\tilde{k}^2=-m_\pi^2} \\ &= 4\frac{m_0}{m^*} - 2N_cN_f\frac{(am_\pi)^2}{\beta}I(-(am_\pi)^2). \end{aligned} \tag{2.43}$$

Setting m_π to a phenomenologically reasonable 138MeV and demanding that (2.42) is satisfied fixes the bare mass to $am_0 = 0.006$ and the inverse-coupling to $\beta = 0.495$. Table 2.1 contains a summary of the fits carried out and parameters extracted. It also contains results of the above analysis repeated with different values of the constituent quark mass.

Phenomenological Observables Fitted	Lattice Parameters Extracted
$m^* = 350$MeV $f_\pi = 93$MeV $m_\pi = 138$MeV	$am_0 = 0.006$ $\beta = 0.518$ $a^{-1} = 714$MeV
$m^* = 400$MeV $f_\pi = 93$MeV $m_\pi = 138$MeV	$am_0 = 0.006$ $\beta = 0.495$ $a^{-1} = 720$MeV
$m^* = 450$MeV $f_\pi = 93$MeV $m_\pi = 138$MeV	$am_0 = 0.006$ $\beta = 0.475$ $a^{-1} = 728$MeV

Table 2.1: Summary of large-N_c parameter fits.

Chapter 3

Zero Temperature Phase Structure

3.1 The Simulation

The phase structure of the Nambu–Jona-Lasinio model is known from self-consistent approaches to be both rich and varied. At low temperature and chemical potential, spontaneous chiral symmetry breaking leads to a dynamically generated fermion mass, whilst at high temperature the model passes through a transition into a phase in which this symmetry is restored [48,49]. The fact that this behaviour of the symmetry structure at zero chemical potential closely resembles results from lattice QCD [17,18] is encouraging when considering the model at $\mu > T$, where the numerical solution of QCD remains elusive. Self-consistent treatment of the model in this region has shown there to be a BCS phase with restored chiral symmetry and a superconducting gap $\Delta > 0$ for sufficiently high density and low enough temperature [27]. In this chapter a numerical study of the phase structure of the model as a function of chemical potential is presented. The chiral condensate and baryon number density have been measured and are shown to qualitatively agree with the self-consistent solution calculated in the large-N_c limit. In the diquark sector, measurement of the order parameter and related susceptibilities provide non-perturbative evidence for the existence of the BCS

phase at intermediate densities that may be phenomenologically relevant in the study of compact stars. These initial results have been extrapolated to zero temperature, since with no thermal effects, the BCS gap should be at its largest, and evidence of diquark condensation is likely to be strongest. Before the presentation of any results, however, it is necessary to discuss some technicalities of the simulation and the approximations that have been made.

The Euclidean path integral of the lattice model described in section 2.3 is

$$\mathcal{Z} = \int \mathrm{d}\sigma \mathrm{d}\vec{\pi} \mathrm{d}\Psi^{\mathrm{tr}} \mathrm{d}\Psi \mathrm{d}\Upsilon^{\mathrm{tr}} \mathrm{d}\Upsilon e^{-S}, \tag{3.1}$$

where S is the lattice action (2.15). Integrating over the fermionic bispinors, we have

$$\mathcal{Z} = \int \mathrm{d}\sigma \mathrm{d}\vec{\pi} \mathrm{Pf}^2 \left(2\mathcal{A}\left[\sigma, \vec{\pi}\right]\right) \exp\left\{-\frac{2}{g^2}\left(\sigma^2 + \vec{\pi}.\vec{\pi}\right)\right\}, \tag{3.2}$$

where the pfaffian $\mathrm{Pf}\mathcal{Q} \equiv \sqrt{\det \mathcal{Q}}$.

Simulations were carried out with the Hybrid Monte-Carlo (HMC) algorithm [50] described in appendix B.1.1, which has the advantage of being exact, i.e. the only errors in measured quantities are statistical in origin. Since this algorithm requires the evaluation of the full action at the end of each trajectory, one is required to use an integer N species of staggered quark corresponding to $N_c = 8N$ continuum quark colours.

In order for the importance sampling techniques used in the HMC algorithm to work, it is important to show that the $\mathrm{Pf}^2\left(2\mathcal{A}\right) = \det 2\mathcal{A}$ is both real and positive. This proof, outlined in [38], is repeated here for completeness. First, we use the property of a block square matrix

$$\det \begin{pmatrix} X & Y \\ W & Z \end{pmatrix} = \det X \det\left(Z - WX^{-1}Y\right) \tag{3.3}$$

to show that

$$\det 2\mathcal{A} = \det(j\bar{j} + \tau_2 M^{\mathrm{tr}} \tau_2 M). \tag{3.4}$$

Using the identity $\tau_2\tau_i\tau_2 \equiv -\tau_i^*$, it is then simple to show that $\tau_2 M \tau_2 = M^*$, and therefore

$$\det 2\mathcal{A} = \det(j\bar{j} + M^\dagger M), \tag{3.5}$$

which is real and positive if $j\bar{j}$ is chosen real and positive. We set $j = \bar{j} = j^*$ throughout, which fulfils this requirement. In the limit that $j, \bar{j} \to 0$, (3.5) reduces to $\det\left(M^\dagger M\right)$, which is manifestly real. Furthermore, it is possible show that $\det M$ itself is both real and positive by use of an argument that was used in [33] to show that this is the case in 2 colour QCD. The argument, outlined in full in appendix B.1.2, states that if there exists a unitary operator T such that $[KT, M] = 0$ and $(KT)^2 = -1$, where K is the complex conjugation operator, then $\det M$ is both real and positive. If we choose $T = \tau_2$, we see that $[K\tau_2, M] = (K\tau_2 M - MK\tau_2) = (\tau_2^* M^* \tau_2^* - M)\tau_2^* K = 0$ and $(K\tau_2)^2 = K\tau_2 K\tau_2 = \tau_2^*\tau_2 = -\mathbb{1}_2$, so both of these criteria are met.

This reassuring property means that were simulations carried out with the hybrid molecular dynamics "R" algorithm [51], one could safely choose $N = \frac{1}{2} \Rightarrow N_c = 4$. In keeping with [46], however, we keep $N = 1$ corresponding to $N_c = 8$ in the continuum. The fact that $\det M$ is both real and positive may also be a reflection of the fact that interactions between quarks from M and conjugate quarks from $M^\dagger$ do not play an important rôle in the dynamics of the lattice NJL model [52]. In QCD, in which $\det M(\mu \neq 0)$ is not real, this is not true; simulations with $\det(M^\dagger M)$ lead to the formation of Goldstone baryons between the quarks and conjugate quarks and the onset of matter occurs at $\mu \sim m_\pi/2$ rather than at $\mu \sim m_p/3$.

Simulations were carried out on $L_s^3 \times L_t$ lattices with $L_s = L_t = 12$, 16 and 20, for various values of μ. Approximately 500 equilibrated configurations separated by HMC trajectories of mean length 1.0 were generated in each run. The non-integer parameter N', i.e. the number of staggered quark species used in the "molecular dynamic" generation of trajectories, was tuned so that the acceptance rate was high, whilst the number of time-steps per trajectory could be kept fairly low. The reason this was possible is that the trajectories' only rôle in the HMC algorithm is to separate successive Monte-Carlo steps in phase-space, whilst remaining in a region in which the acceptance rate is high. The numerical evaluation of the path integral occurs solely in the accept/reject step for which N is kept strictly 1.0 and the physics of the simulation remains unchanged. Empirically, the optimum value of N' was found to be slightly larger than N, and tended to decrease as the volume of the lattice increased. As an example of the improvement that this can bring, in a run at $\mu = 0$ on a 20^4 lattice with time-step $\delta\tau = 0.1$ and $N' = N = 1.0$ the acceptance rate was as low as 26%. By increasing N' to 1.005 and keeping the time-step the same length this rate was increased to 80%.

Another deviation from the standard algorithm is that the diquark terms were treated in the partially quenched approximation, in which the sources j and $\bar{j}$ were set to zero during the HMC update of the bosonic fields and the functional measure reduced to $\det(M^\dagger M)$. The sources were made non-zero and the full path integral restored only during the measurement of diquark observables. Field theoretically, this means that the formation of virtual diquark pairs in the vacuum was suppressed. This approach has the advantage that one can examine many source strengths for only one computationally expensive chain of field evolutions but it is theoretically less sound

than a full simulation with dynamical diquarks. It should be noted, however, that no significant effect on diquark observables due to partial quenching was noted in [38].

3.2 The Chiral Phase Transition

As has been previously discussed, self-consistent treatment of the NJL model shows that for sufficiently strong coupling the approximate $SU(2)_L \otimes SU(2)_R$ chiral symmetry is spontaneously broken in the vacuum to $SU(2)_V$, leading to a dynamically generated quark mass $m^* = \Sigma + m_0$, and 3 degenerate pseudo-Goldstone modes identified with the pions. In the presence of a baryon chemical potential $\mu \neq 0$ the symmetry is approximately restored as μ is increased through some onset scale $\mu_o \sim \Sigma$, with the order of the transition being sensitive to the parameters employed [41].

We determine the nature of this transition in our physically reasonable regime by studying the order parameter of chiral symmetry breaking, the chiral condensate $\langle \overline{\chi}\chi \rangle$, defined by

$$\langle \overline{\chi}\chi \rangle \equiv \frac{1}{V} \frac{\partial \ln \mathcal{Z}}{\partial m_0}. \tag{3.6}$$

Using the form of the path integral (3.2), we find that

$$\frac{\partial \ln \mathcal{Z}}{\partial m_0} = \left\langle \frac{\partial \ln \mathrm{Pf}(2\mathcal{A})}{\partial m_0} \right\rangle = \left\langle \frac{1}{2} \frac{\mathrm{Tr} \partial \ln(2\mathcal{A})}{\partial m_0} \right\rangle = \left\langle \frac{1}{4} \mathrm{Tr} \begin{pmatrix} 0 & \mathbb{1}_2 \\ -\mathbb{1}_2 & 0 \end{pmatrix} \mathcal{A}^{-1} \right\rangle. \tag{3.7}$$

The reason why the above expression contains the pfaffian of $2\mathcal{A}$ rather than the determinant, is that in keeping with [38] we chose not to take the derivative of the part containing the bispinors Υ and Υ^{tr}. An equivalent statement is that we chose to differentiate only with respect to the current mass of the Ψ and Ψ^{tr} fields.

The traces were taken via a stochastic estimation in which one chooses a complex

pseudofermion estimator η from a Gaussian distribution such that

$$\eta^\dagger\eta \approx 4V \quad \Rightarrow \quad \eta^\dagger\mathcal{Q}\eta \approx \mathrm{Tr}\mathcal{Q}, \tag{3.8}$$

where $\mathcal{Q}$ is some square matrix with the same dimension as $\mathcal{A}$. The expectation value was then found by taking the average of the measurement carried out on n_{conf} successive field configurations $[\Phi]$ such that

$$\begin{aligned}\langle\overline{\chi}\chi\rangle &= \frac{1}{4V}\left\langle \eta^\dagger \begin{pmatrix} 0 & \mathbb{1}_2 \\ -\mathbb{1}_2 & 0 \end{pmatrix} \mathcal{A}^{-1}\eta \right\rangle \\ &= \frac{1}{n_{\mathrm{conf}}}\frac{1}{4V}\sum_{[\Phi]} \eta^\dagger \begin{pmatrix} 0 & \mathbb{1}_2 \\ -\mathbb{1}_2 & 0 \end{pmatrix} \mathcal{A}^{-1}\eta. \end{aligned} \tag{3.9}$$

We also define the baryon number density per flavour as

$$n_B \equiv \frac{1}{2}\frac{\partial \ln \mathcal{Z}}{\partial \mu}, \tag{3.10}$$

which calculated on the lattice is

$$n_B = \frac{1}{16V}\left\langle \eta_x^\dagger \begin{pmatrix} 0 & e^{\mu}\delta_{x,y+\hat{0}} + e^{-\mu}\delta_{x,y-\hat{0}} \\ -e^{\mu}\delta_{x,y-\hat{0}} - e^{-\mu}\delta_{x,y+\hat{0}} & 0 \end{pmatrix} \mathcal{A}^{-1}\eta_y \right\rangle. \tag{3.11}$$

The matrix $\mathcal{A}$ was inverted using the same conjugate gradient algorithm used in the HMC field updates [53]. Because here we wish to evaluate the inverse of $\mathcal{A}$ rather than M, the noise vectors chosen here were twice the size. This algorithm solves the vector equation $\mathbf{A}.\mathbf{x} = \mathbf{b}$ to an accuracy dependent on a parameter known as the stopping residual. In our measurement routines we used $\mathbf{A} = \mathcal{A}^\dagger\mathcal{A}$ and $\mathbf{b} = \mathcal{A}^\dagger\eta$, such that the resulting vector $\mathbf{x} = (\mathcal{A}^\dagger\mathcal{A})^{-1}\mathcal{A}^\dagger\eta = \mathcal{A}^{-1}\eta$. To calculate $\langle\overline{\chi}\chi\rangle$ and n_B, therefore, only one inversion of $\mathcal{A}$ was necessary, during which the stopping residual per site r_s was chosen as 1×10^{-5}. For more information on this algorithm see appendix B.1.3.

Both $\langle\overline{\chi}\chi\rangle$ and n_B were calculated at various values of $\mu \in [0, 1.2]$ on 12^4, 16^4 and 20^4 lattices, with measurements made on every other field configuration. At the time of each measurement, 5 pseudofermion estimations were made of both $\langle\overline{\chi}\chi\rangle$ and n_B and the average recorded. The cost of the simulation was much greater in the chirally restored phase than in the chirally broken one, since the rate of convergence of the matrix inversion is related to the magnitude of the diagonal elements of M, which in turn are proportional to m^*. For example, the run at $\mu = 1.0$ on a 20^4 lattice took approximately 8.5 CPU days on a 2.0GHz Xeon processor. On the same CPU, the run at $\mu = 0.0$ took just over 3 days.

Once the simulations were complete, the statistical errors in the measured quantities were calculated using the jackknife estimate described in appendix B.2. Results were extrapolated linearly to the infinite volume limit $V^{-1} \to 0$ by a least-squares fit solved via singular value decomposition. A discussion of the curve-fitting procedure used is contained in appendix B.3. As an example of the quality of the fits, the

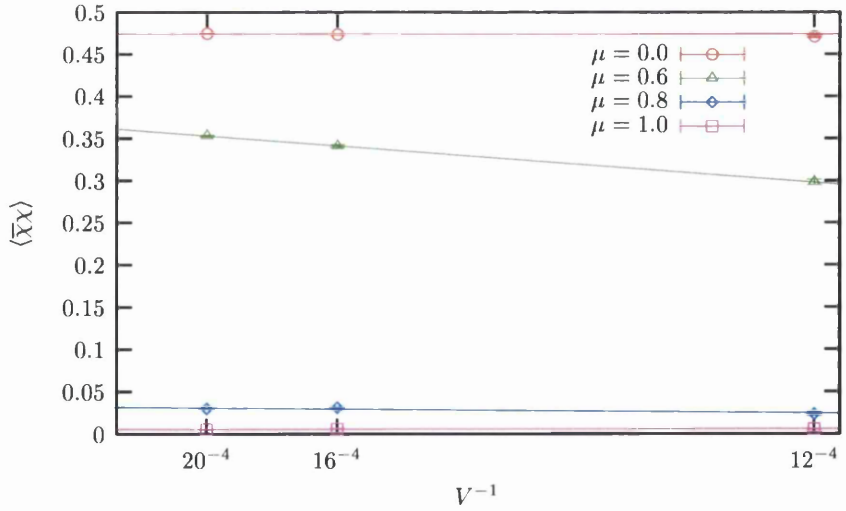

Figure 3.1: Extrapolations of $\langle\overline{\chi}\chi\rangle$ to $V^{-1} \to 0$ for $\mu = 0.0$, 0.6, 0.8, and 1.0.

χ^2/d.o.f. for the curves fitted to $\langle\overline{\chi}\chi\rangle$ at $\mu = 0.0$, 0.6, 0.8 and 1.0 were 7.05, 0.02, 4.27 and 0.60 respectively. These values are higher than one would wish for, as three volumes, corresponding to a single degree of freedom, is the minimum number for which a linear fit has any meaning. They do show the fits to be acceptable, however, especially when one considers Fig. 3.1, in which the dependence on V^{-1} appears only weak.

In order to compare the lattice data with perturbative results, both $\langle\overline{\chi}\chi\rangle$ and n_B were calculated to leading order in $1/N_c$. This large-N_c limit corresponds to a mean-field theory, in which the scalar field $\sigma = \Sigma$ on every dual lattice point, and the auxiliary pseudoscalars $\vec{\pi}$ are exactly zero. In this limit, and with $j = 0$, (3.9) becomes

$$\lim_{N_c\to\infty}\langle\overline{\chi}\chi\rangle = \frac{1}{4V}\sum_{\nu=0}^{3}\sum_{k_\nu=-\pi/2}^{\pi/2}\mathrm{Tr}4M[\mu,k_\nu]^{-1}, \tag{3.12}$$

where $M[\mu,k_\nu]$ is the fermion matrix on a blocked lattice and transfered into momentum space. The trace of its inverse is

$$\mathrm{Tr}M[\mu,k_\nu]^{-1} = \frac{32m^*}{\frac{1}{2}(1-\cos 2k_0\cosh 2\mu - i\sin 2k_0\sinh 2\mu) + \sum_{j=1}^{3}\sin^2 k_j + m^{*2}}. \tag{3.13}$$

Similarly, the baryon number density (3.10) becomes

$$\lim_{N_c\to\infty} n_B = -\frac{1}{4V}\frac{1}{m^*}\sum_{\nu=0}^{3}\sum_{k_\nu=-\pi/2}^{\pi/2}(\cos 2k_0\sinh 2\mu + i\sin 2k_0\cosh 2\mu)\,\mathrm{Tr}M[\mu,k_\nu]^{-1}. \tag{3.14}$$

The solutions to these equations were found by evaluating the mode sums on the same sized lattices as those on which the simulations were carried out, and extrapolating to V^{-1} in the same manner. The quality of the extrapolation was then checked by

comparing the results to (3.12) and (3.14) evaluated on a 150^4 lattice, beyond which, increasing V was seen to have little or no effect.

Our results are shown in Fig. 3.2. To leading order in $1/N_c$ chiral symmetry is approximately restored via a crossover between $0.4 \lesssim \mu \lesssim 0.6$. The lattice data agree qualitatively with this although both $\langle \overline{\chi}\chi \rangle$ and μ_o are about 15-20% smaller, which we attribute to corrections of $\mathcal{O}(1/N_c)$. n_B increases approximately as a power of μ, with saturation effects appearing for $\mu > 1.0$, as not far beyond this point the occupancy of states on the finite volume system becomes close to one per flavour label per site.

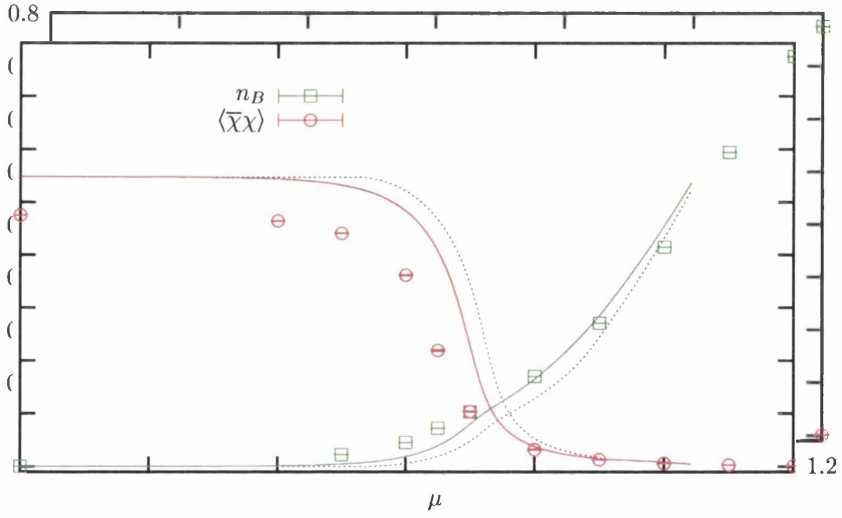

Figure 3.2: Chiral condensate and number density as functions of μ extrapolated to $V^{-1} \to 0$ showing both the large-N_c solution (solid curve) and lattice results (points). The dashed curves are the large-N_c solutions solved directly in the infinite volume limit.

As was discussed in chapter 2, the NJL model is believed to have no nuclear matter phase between the vacuum and chiral symmetry restoration, which is confirmed here since the crossovers in $\langle \overline{\chi}\chi \rangle$ and n_B are coincident. For this reason we cannot interpret the fact that we observe a crossover phenomenologically. It is interesting to compare

this, however, with the $2+1d$ model in which the transition is strongly first-order [38, 46].

3.3 Diquark Condensation and Superfluidity

The main purpose of this study of the model's phase structure was to determine the nature of the high density phase in which chiral symmetry is approximately restored. In particular, in order to explore the possibility of a $U(1)_B$-violating BCS phase we have studied diquark order parameters and their susceptibilities [38, 46] as functions of chemical potential. To define these parameters let us first introduce the operators

$$qq_{\pm}(x) = \chi^{\mathrm{tr}}\frac{\tau_2}{4}\chi(x) \pm \overline{\chi}\frac{\tau_2}{4}\overline{\chi}^{\mathrm{tr}}, \tag{3.15}$$

which allow one to define both the diquark condensates

$$\langle qq_{\pm}\rangle \equiv \frac{1}{V}\frac{\partial \ln \mathcal{Z}}{\partial j_{\pm}}, \tag{3.16}$$

where $j_{\pm} = j \pm \overline{\jmath}$, and the related susceptibilities

$$\begin{aligned}\chi_{\pm} &= \sum_x \left\langle qq_{\pm}(0)qq_{\pm}(x)\right\rangle &(3.17)\\ &= \frac{1}{16}\sum_x \left\langle \chi^{\mathrm{tr}}\tau_2\chi(0)\chi^{\mathrm{tr}}\tau_2\chi(x) + \overline{\chi}\tau_2\overline{\chi}^{\mathrm{tr}}(0)\overline{\chi}\tau_2\overline{\chi}^{\mathrm{tr}}(x)\right\rangle \\ &\qquad \pm \left\langle \chi^{\mathrm{tr}}\tau_2\chi(0)\overline{\chi}\tau_2\overline{\chi}^{\mathrm{tr}}(x) + \overline{\chi}\tau_2\overline{\chi}^{\mathrm{tr}}(0)\chi^{\mathrm{tr}}\tau_2\chi(x)\right\rangle . &(3.18)\end{aligned}$$

On their own, these susceptibilities are of limited importance. From (3.18), however, it is straightforward to derive the Ward identity

$$\chi_-|_{j_-\to 0} = \frac{\langle qq_+\rangle}{j_+}, \tag{3.19}$$

which along with the ratio

$$R = -\frac{\chi_+}{\chi_-} \tag{3.20}$$

allows one to distinguish between phases in which the $U(1)_B$ symmetry is either manifest or broken. With the symmetry manifest and in the limit $j \to 0$, these two susceptibilities should be identical up to a sign factor and the ratio should equal 1. If the symmetry is broken, the Ward identity predicts that χ_- should diverge as $j \to 0$ and that R should vanish.

To calculate the diquark condensate one can use the same stochastic estimation method used to measure $\langle\overline{\chi}\chi\rangle$ and n_B via

$$\langle qq_\pm\rangle = \frac{1}{8V}\left\langle \eta^\dagger \begin{pmatrix} \pm\tau_2 & 0 \\ 0 & \tau_2 \end{pmatrix} \mathcal{A}^{-1}\eta \right\rangle . \tag{3.21}$$

Once again, the definition (3.21) allows one to use the same values of $\mathcal{A}^{-1}\eta$ as in the evaluation of $\langle\overline{\chi}\chi\rangle$ and n_B and one is not required to carry out an extra inversion of $\mathcal{A}$.

To calculate the susceptibilities, let us first write them as the sum of two contributions corresponding to the two possible Wick contractions

$$\chi = \left[\left\langle(\mathrm{Tr}\Gamma\mathcal{G}_{xx})^2\right\rangle - \left\langle\mathrm{Tr}\Gamma\mathcal{G}_{xx}\right\rangle^2\right] + \left\langle\mathrm{Tr}\Gamma\mathcal{G}_{0x}\Gamma\mathcal{G}_{0x}^{\mathrm{tr}}\right\rangle , \tag{3.22}$$

$$= \left[\left\langle \bigcirc\!\bullet\!\bigcirc \right\rangle - \left\langle \bigcirc\!\bullet \right\rangle^2\right] + \left\langle \bigcirc\!\!\bullet\!\!\bigcirc \right\rangle \equiv \chi^{dis} + \chi^{con}, \tag{3.23}$$

where $\mathcal{G} = \mathcal{A}^{-1}$ is the Gor'kov propagator

$$\mathcal{G}_{xy} = \mathcal{A}^{-1}_{xy} = \begin{pmatrix} \left\langle\chi_x\chi_y^{\mathrm{tr}}\right\rangle & \left\langle\chi_x\overline{\chi}_y\right\rangle \\ \left\langle\overline{\chi}_x^{\mathrm{tr}}\chi_y^{\mathrm{tr}}\right\rangle & \left\langle\overline{\chi}_x^{\mathrm{tr}}\overline{\chi}_y\right\rangle \end{pmatrix} , \tag{3.24}$$

and Γ projects out the appropriate components. We label these components the "disconnected" and "connected" susceptibilities respectively. This definition implies that the disconnected component follows directly from (3.21) as

$$\chi_\pm^{dis} = \left\langle qq_\pm^2\right\rangle - V\left\langle qq_\pm\right\rangle^2 . \tag{3.25}$$

Although the first term of (3.25) appears to need an extra inversion of $\mathcal{A}$, it was possible to take advantage of the fact that $n = 5$ measurements of $qq_{\pm}$ were made and use

$$\left\langle qq_{\pm}^2 \right\rangle = \frac{2}{64V}\frac{1}{n(n-1)}\left\langle \sum_{\alpha=1,\beta\neq\alpha}^{n} \eta^{\alpha\dagger}\begin{pmatrix} \tau_2 & 0 \\ 0 & \tau_2 \end{pmatrix}\mathcal{A}^{-1}\eta^{\alpha}\eta^{\beta\dagger}\begin{pmatrix} \tau_2 & 0 \\ 0 & \tau_2 \end{pmatrix}\mathcal{A}^{-1}\eta^{\beta}\right\rangle. \tag{3.26}$$

For the connected component, let us calculate the four terms in (3.18) independently. The first term is

$$\left\langle \chi^{\mathrm{tr}}\frac{\tau_2}{4}\chi(0)\chi^{\mathrm{tr}}\frac{\tau_2}{4}\chi(x)\right\rangle = -\frac{1}{4}\left\langle \chi_1\chi_2(0)\chi_1\chi_2(x)\right\rangle, \tag{3.27}$$

which after Wick contraction of the non-local terms leaves

$$\left\langle \chi_1\chi_1\right\rangle_{0x}\left\langle \chi_2\chi_2\right\rangle_{0x} - \left\langle \chi_1\chi_2\right\rangle_{0x}\left\langle \chi_2\chi_1\right\rangle_{0x} = \mathcal{G}_{11}\mathcal{G}_{22} - \mathcal{G}_{12}\mathcal{G}_{21}. \tag{3.28}$$

Similarly, the three remaining components are

$$\left\langle \overline{\chi}\frac{\tau_2}{4}\overline{\chi}^{\mathrm{tr}}(0)\overline{\chi}\frac{\tau_2}{4}\overline{\chi}^{\mathrm{tr}}(x)\right\rangle = \frac{1}{4}(\mathcal{G}_{33}\mathcal{G}_{44} - \mathcal{G}_{34}\mathcal{G}_{43}); \tag{3.29}$$

$$\left\langle \chi^{\mathrm{tr}}\frac{\tau_2}{4}\chi(0)\overline{\chi}\frac{\tau_2}{4}\overline{\chi}^{\mathrm{tr}}(x)\right\rangle = \frac{1}{4}(\mathcal{G}_{14}\mathcal{G}_{23} - \mathcal{G}_{13}\mathcal{G}_{24}); \tag{3.30}$$

$$\left\langle \overline{\chi}\frac{\tau_2}{4}\overline{\chi}^{\mathrm{tr}}(0)\chi^{\mathrm{tr}}\frac{\tau_2}{4}\chi(x)\right\rangle = \frac{1}{4}(\mathcal{G}_{31}\mathcal{G}_{42} - \mathcal{G}_{32}\mathcal{G}_{41}), \tag{3.31}$$

which imply that one must to know all of $\mathcal{G}$ to calculate $\chi_{\pm}$. This was done by choosing a random point source on the lattice, which was labelled $x = 0$, and defining $\eta_i^{\dagger}$ as the ith component of $\eta^{\dagger} = (\delta_{0x}, \delta_{0x}, \delta_{0x}, \delta_{0x})$. By calculating $\langle \sum_x \mathcal{A}^{-1}\eta_i\rangle$ for each i one has therefore calculated the four columns of $\mathcal{G}$. The fact that both $\langle \overline{\chi}_x\chi_y\rangle$ and $\tau_2\langle \chi_x^{\mathrm{tr}}\chi_y\rangle$ and their barred counterparts are proportional to elements of $SU(2)$, however, implies the following symmetry constraints:

$$\begin{aligned} &\mathcal{G}_{21} = \mathcal{G}_{12}^*, \quad \mathcal{G}_{22} = -\mathcal{G}_{11}^*, \quad \mathcal{G}_{23} = -\mathcal{G}_{14}^*, \quad \mathcal{G}_{24} = \mathcal{G}_{13}^*; \\ &\mathcal{G}_{41} = -\mathcal{G}_{32}^*, \quad \mathcal{G}_{42} = \mathcal{G}_{31}^*, \quad \mathcal{G}_{43} = \mathcal{G}_{34}^*, \quad \mathcal{G}_{44} = -\mathcal{G}_{33}^*, \end{aligned} \tag{3.32}$$

such that in order to know the whole propagator one need only calculate the first and third columns. The connected susceptibilities are then given by

$$\chi_{\pm}^{con} = -\frac{\left[|\mathcal{G}_{11}|^2 + |\mathcal{G}_{21}|^2 + |\mathcal{G}_{33}|^2 + |\mathcal{G}_{43}|^2\right]}{4} \pm \frac{\left[|\mathcal{G}_{13}|^2 + |\mathcal{G}_{23}|^2 + |\mathcal{G}_{31}|^2 + |\mathcal{G}_{41}|^2\right]}{4}. \quad (3.33)$$

These susceptibilities were calculated on the same lattices used in the previous section for various values of μ. It is interesting to note that although in most cases the disconnected contributions were found to be consistent with zero, in the low μ phase with large j, χ_{+}^{dis} could be up to $10-20\%$ the magnitude of χ_{+}^{con}, an example of which is illustrated in Fig. 3.3. In contrast with the NJL model in 2+1d [38], therefore, we cannot ignore these contributions and assume that $\chi_{+} \simeq \chi_{+}^{con}$.

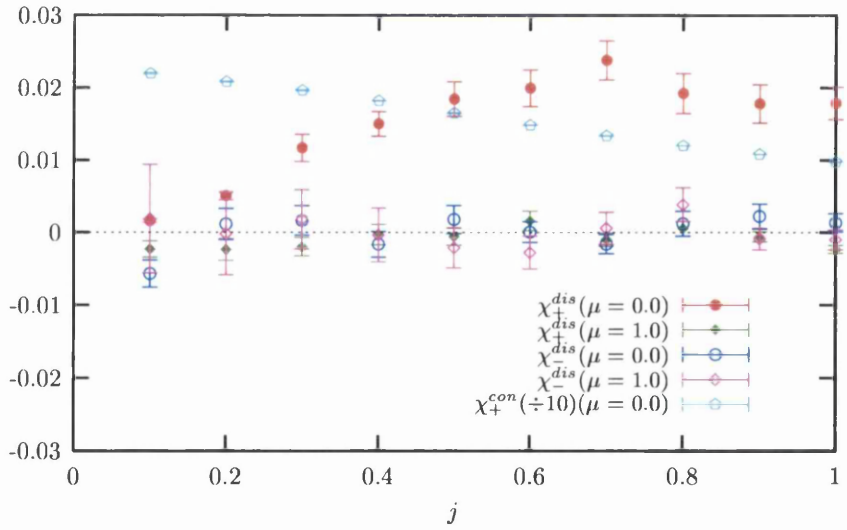

Figure 3.3: $\chi_{\pm}^{dis}$ at $\mu = 0.0$ and 1.0 on a 16^4 lattice. $\chi_{+}^{con}/10$ at $\mu = 0.0$ has been included for comparison.

Because the disconnected part is the difference of highly correlated numbers, i.e. $\langle qq^2 \rangle$ and $V \langle qq \rangle^2$, one cannot simply calculate the errors in each quantity and then combine them in the standard way, since this would grossly overestimate the error and "swamp" any signal in the susceptibility data. Instead one can take advantage

of the fact that $\langle qq^2 \rangle - V \langle qq \rangle^2$ is essentially the variance of $\langle qq \rangle$, and calculate the variance of this variance with a jackknife estimate.

Because $\chi_{\pm}^{con}$ are non-local objects we require high accuracy in calculation of these quantities since the signal becomes small as $x \to \infty$. For this reason, when calculating $\chi_{\pm}^{con}$ a significantly smaller stopping residual of $r_s = 1 \times 10^{-8}$ was used in the conjugate gradient routine. Although this means that more iterations were required for the algorithm to converge, the fact that $j \neq 0$ did help to counter this and keep the number of iterations reasonable, since these components are close to the diagonal. Indeed, in the high μ phase, when m^* is small, increasing j from 0.1 to 1.0 was seen to reduce the number of iterations by a factor of 4.

Some data for $\chi_{\pm}$ from a 16^4 lattice, including the disconnected contribution, are presented in Fig. 3.4. The main points to note are that similarly to the results pre-

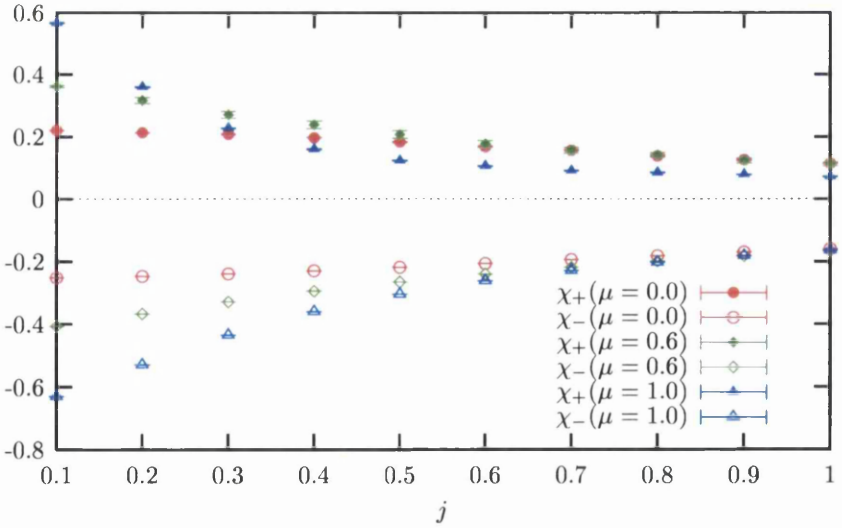

Figure 3.4: $\chi_{\pm}$ vs. j at $\mu = 0.0$, 0.6 and 1.0 on a 16^4 lattice.

sented in [38], the susceptibilities obey the general trend that $|\chi_-| > |\chi_+|$. Also, we see little j dependence at low μ, whilst as μ slowly increases, so does the dependence

on j. If the $U(1)_B$ symmetry were broken one would expect χ_- to diverge, whilst χ_+ remains finite. To check whether this was the case the ratio between the susceptibilities R defined in (3.20)was calculated. Having first checked that the Ward identity is satisfied, one can use the RHS of (3.19) to replace the measured value of χ_- since this makes the statistical error in R much smaller. The ratio was extrapolated to the limit $L_t^{-1} \to 0$, corresponding to zero temperature, which as in [38] was found to be a reasonable extrapolation. An example of the quality of the fits is illustrated in Fig. 3.5.

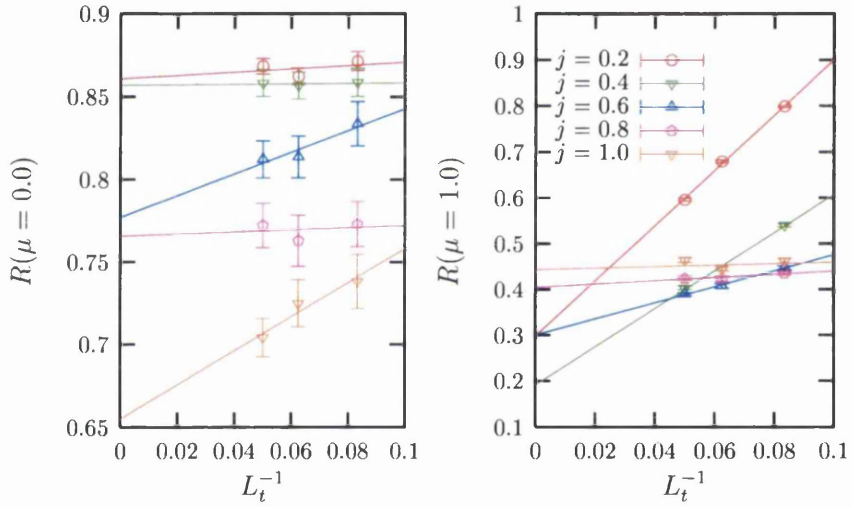

Figure 3.5: Susceptibility ratio R at $\mu = 0.0$ and 1.0 on various lattice sizes.

Fig. 3.6 shows the extrapolated data plotted against j for various values of μ. Although the linear fits made through the data for $j \geq 0.3$ are reasonable, for $j < 0.3$ the data depart sharply from the fit, especially in the high density phase $\mu \gtrsim 0.6$. One explanation for this could be that if there is a spontaneously broken symmetry in the high μ phase, so that as one takes $j \to 0$ one approaches an exact Goldstone mode and the effects of working on a finite volume become more pronounced. We propose, however, that the deviation of data at low j can be explained by a geometrically

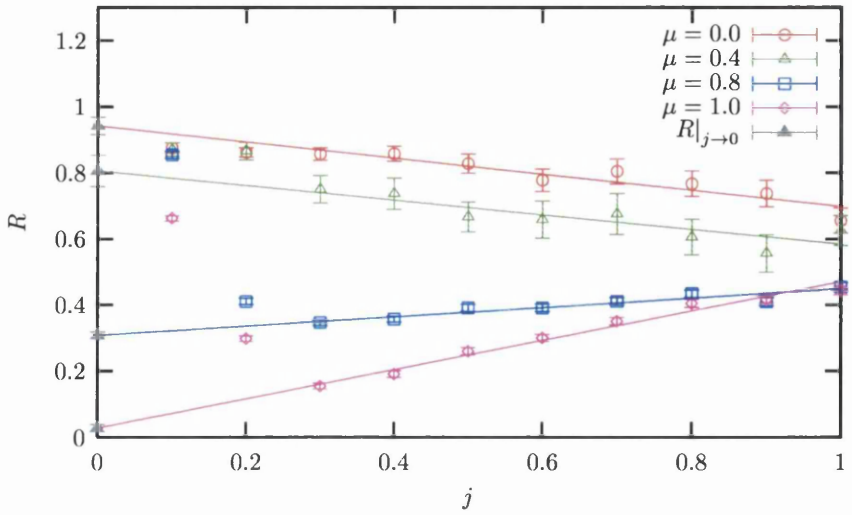

Figure 3.6: R vs. j for various values of μ.

motivated argument related to our trying to represent a thin shell of states about the Fermi surface on a simple cubic momentum-space lattice. This argument is developed further in chapter 5.

Assuming that one is justified in disregarding the points with $j < 0.3$, one can see from Fig. 3.6 that for $\mu = 0$ a linear fit is consistent with a ratio of $R \approx 1$, corresponding to a manifest baryon number symmetry as one would expect in the vacuum. At $\mu = 1.0$, however, $R \approx 0$ suggesting that the $U(1)_B$ symmetry is broken.

For more direct evidence of diquark condensation let us study the order parameter defined in (3.21). Again, these data were extrapolated linearly to the limit $L_t^{-1} \to 0$ and the quality of the fits was found to be good. Fig. 3.7 shows the extrapolated values of $\langle qq_+ \rangle$ plotted against j for various values of μ. Fitting a quadratic curve through the data with $j \geq 0.3$, one can clearly see that for high μ the low j points lie well below the curves. Ignoring these points, the data were extrapolated to $j \to 0$. For $\mu = 0$ we find no diquark condensation as expected, but as μ increases from zero, so does $\langle qq_+ \rangle$. Together, the observations that $\lim_{j\to 0} R = 0$ and $\lim_{j\to 0} \langle qq_+ \rangle \neq 0$

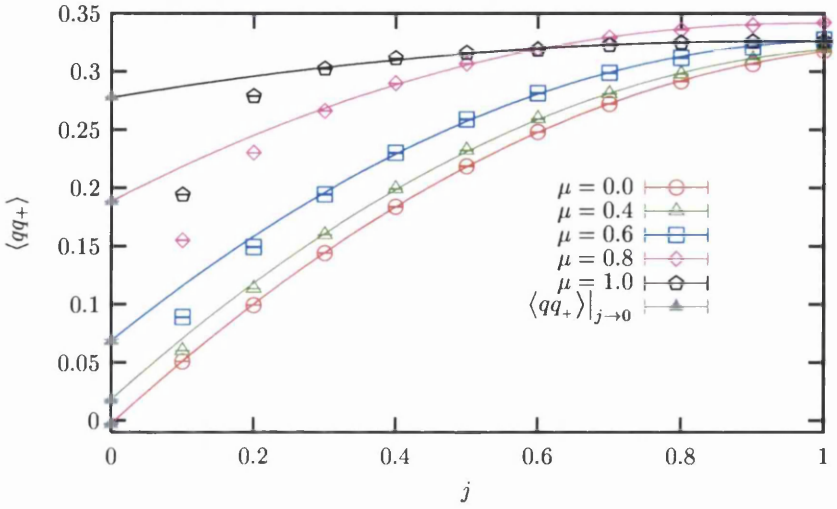

Figure 3.7: $\langle qq_+ \rangle$ extrapolated to $j \to 0$ for various μ.

support the existence of a BCS superfluid phase at high chemical potential.

Finally, $\langle qq_+ \rangle$ is plotted as a function of μ in Fig. 3.8 along with the previously presented results for $\langle \overline{\chi}\chi \rangle$ and n_B. Although there is clearly a crossover from a phase with no diquark condensation to one in which the diquark condensate has a magnitude approximately that of the vacuum chiral condensate, this crossover is far less pronounced than in the chiral case. $\langle qq_+ \rangle$ increases approximately as μ^2, but eventually saturates as μ approaches 1.0 and even decreases past $\mu \sim 1.1$. This is a sign that $\langle qq_+ \rangle$ is directly related to the surface area of the Fermi surface, which was calculated in the large-N_c limit and is plotted as the solid curve. The curvature $\partial^2 \langle qq_+ \rangle / \partial \mu^2$ is positive, in contrast to the behaviour observed in simulations of two colour QCD in which there is no Fermi surface and $\mathrm{U}(1)_B$ breaking proceeds via Bose-Einstein condensation [33, 34, 39].

The weakness of the transition at intermediate μ is coupled with the fact that at these chemical potentials, the value of $R|_{j_+\to 0}$ interpolates between the two extremes of 0 and 1. This is counterintuitive, since this suggests a partially broken symmetry,

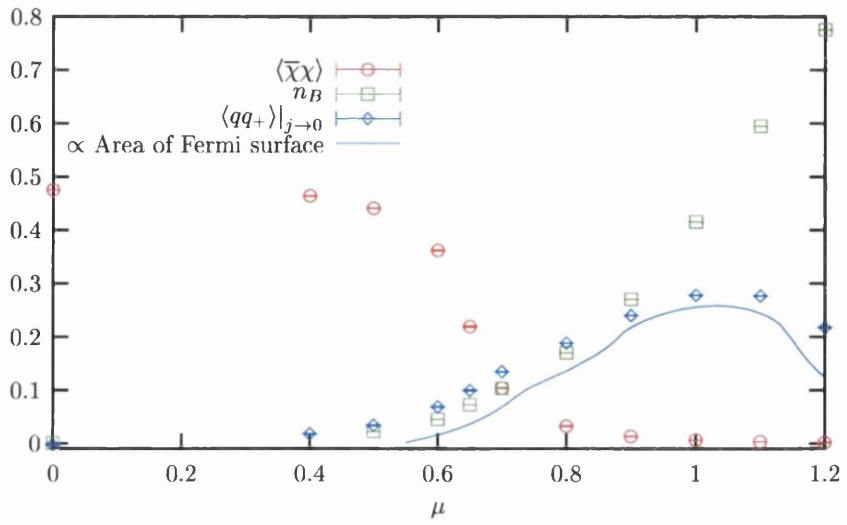

Figure 3.8: A comparison between the diquark and chiral condensates plus the baryon number density, all as functions of μ.

even at $j = 0$. It may be that this is a side-effect of the chiral transition being a crossover, since there is no sharp point at which a large Fermi surface is created. It is also possible, of course, that this behaviour for intermediate μ is an artifact of our poor control over the $j \to 0$ extrapolation.

Chapter 4

Measurement of the Gap

4.1 Spectroscopy in the Fermionic Sector

In the previous chapter, we saw evidence for the existence of a superfluid phase at high chemical potential in the form of a non-zero diquark condensate $\langle qq_+ \rangle$ and a vanishing susceptibility ratio R. This evidence must be treated as indirect, however, since neither of these quantities is measurable in an experiment. Furthermore, even if the sign problem were overcome, one could not measure $\langle qq_+ \rangle$ in lattice QCD, since in this theory the colour superconducting phase is characterised by the breaking of a gauge symmetry; Elitzur's theorem states that one cannot write down a local order parameter to distinguish the existence of such a phase in a gauge-invariant way [54]. Instead we must turn to more direct evidence in the form of the global order parameter for the BCS phase, the energy gap Δ about the Fermi surface.

To measure Δ, one must study the fermion dispersion relation, i.e. the energy of the fermionic degrees of freedom as a function of their 3-momentum $\vec{k}$. This does present a small problem, however. Due to the periodicity of the lattice in spatial dimensions and the doubling of fermionic species, dispersion relations for staggered fermions are symmetric about $k_i = \pi/2a$, leaving only $L_s/4+1$ independent momenta

in each spatial direction. For the largest volume simulated for the previous chapter, this is only 6, which is far too few momenta to map out $E(k)$ and extract Δ. Since simulation on lattices much larger than 20^4 would be computationally too expensive, we chose to use lattices with one spatial dimension much longer than the others, corresponding to a finer resolution in that direction in momentum space.

In order to extract the dispersion relation we define the time-slice propagator

$$\mathcal{G}(\vec{k};t) = \sum_{\vec{x}} \mathcal{G}(\vec{0},0;\vec{x},t)e^{-i\vec{k}.\vec{x}}, \tag{4.1}$$

where $\mathcal{G}$ is the Gor'kov propagator (3.24). As in the original BCS theory [25,26], the fermionic degrees of freedom can be viewed as quasi-particles with energy E relative to the system's Fermi energy E_F. In analogy with the Dirac picture of the quantum vacuum, the promotion of a quark out of the Fermi sea can then be viewed as the creation of a particle-hole pair. In the limit that $j, \bar{\jmath} \to 0$, the propagation of these quasi-particles is described by the "normal" $\langle q(0)\overline{q}(x)\rangle$ and $\langle \overline{q}(0)q(x)\rangle$ parts of (4.1), i.e. those that are off-diagonal in the Nambu-Gor'kov space and related to M^{-1}. If the Fermi surface is unstable with respect to a BCS ground-state, the quasi-particles nearest to E_F undergo particle-hole mixing and a gap appears in the energy spectrum. The propagation of these mixed states is generated by the diagonal, or "anomalous" $\langle q(0)q(x)\rangle$ and $\langle \overline{q}(0)\overline{q}(x)\rangle$ parts of (4.1).

$\mathcal{G}(\vec{k};t)$ was measured on $L_x \times L_{y,z}^2 \times L_t$ lattices with $L_x = 96$, $L_{y,z} = 12$ and $L_t = 12$, 16 and 20 using the same evaluation of (3.24) that was used to measure $\chi_\pm$. Setting $\vec{k} = (k,0,0)$, the available momenta are $ak = 2\pi n/L_x$ $(n = 0,1,2,\ldots,L_s/4)$ such that there are 25 independent momentum modes between 0 and $\pi/2a$. The same values of the diquark sources $j = \bar{\jmath} = j^*$ were used as in the previous chapter for various values of μ between 0 and 1. Again, approximately 500 equilibrated trajectories were

generated per run, with measurement taking place on every other configuration.

The symmetry constraints (3.32) reduce the number of independent components of $\mathcal{G}(\vec{k};t)$ to 16; 8 real and 8 imaginary. Additionally and in agreement with [38], the following features were observed. As a reflection of the conserved $SU(2)_V$ isospin symmetry, the diagonal parts of the anomalous sector $\langle \mathcal{G}_{11} \rangle$ and $\langle \mathcal{G}_{33} \rangle$ and the off-diagonal parts of the normal sector $\langle \mathcal{G}_{41} \rangle$ and $\langle \mathcal{G}_{23} \rangle$ were all found to be consistent with zero. Furthermore, $\mathrm{Re}\,\langle \mathcal{G}_{21} \rangle$ and $\mathrm{Im}\,\langle \mathcal{G}_{13} \rangle$ were also found empirically to be approximately zero. Of the remaining non-zero components, the normal fermion and anti-fermion were found to be related by time reversal, i.e $\mathrm{Re}\,\langle \mathcal{G}_{31}(t) \rangle \approx \mathrm{Re}\,\langle \mathcal{G}_{13}(L_t - t) \rangle$ whilst the anomalous fermion and anti-fermion are equivalent and anti-symmetric in time, i.e. $\mathrm{Im}\,\langle \mathcal{G}_{21}(t) \rangle \approx \mathrm{Im}\,\langle \mathcal{G}_{43}(t) \rangle \approx -\mathrm{Im}\,\langle \mathcal{G}_{21}(L_t - t) \rangle$. The only non-zero, independent components of (3.32), therefore, are

$$N(k,t) \equiv \mathrm{Re}\,\langle \mathcal{G}_{31}(k,t) \rangle \tag{4.2}$$

and

$$A(k,t) \equiv \mathrm{Im}\,\langle \mathcal{G}_{21}(k,t) \rangle\,, \tag{4.3}$$

which from hereon shall be referred to simply as the normal and anomalous propagators respectively. Some example propagators in both the chirally broken and restored phases are plotted in Fig. 4.1. At $\mu = 0.0$ the normal propagator is non-zero for all t, whilst at $\mu = 0.8$ it approximates zero on even time-slices which reflects the fact that with a manifest chiral symmetry the N_{oo} and N_{ee} components of the standard staggered fermion propagator vanish. The anomalous propagator is zero on all odd time-slices for all μ, which reflects that the $SU(2)_V$ symmetry is manifest in both phases.

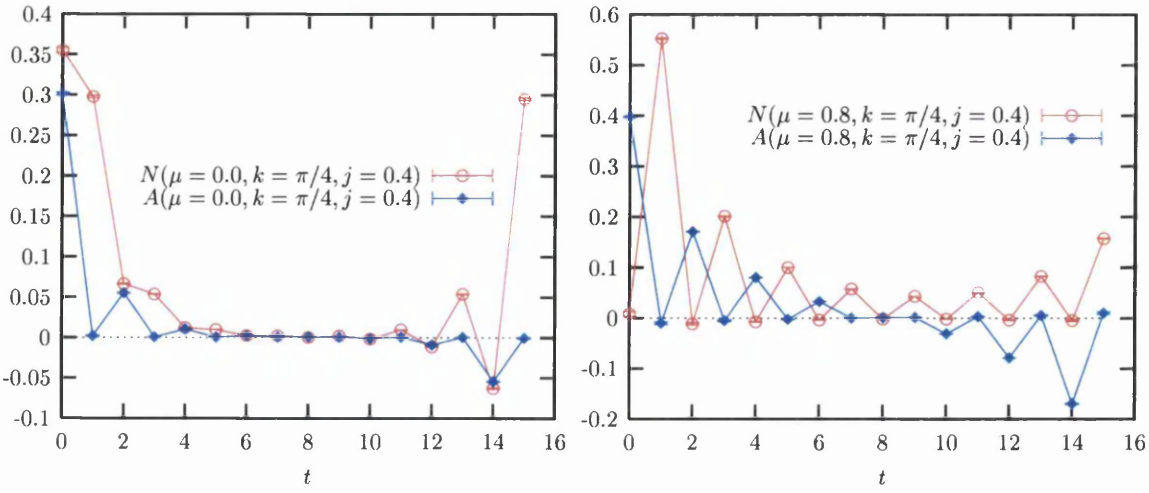

Figure 4.1: Normal and anomalous propagators measured on a $96 \times 12^2 \times 16$ lattice in both the chirally broken and restored phases.

To map out the dispersion relation for each value of μ, the energy was extracted by fitting the propagators to

$$\begin{aligned} N(k,t) &= Ae^{-Et} + Be^{-E(L_t - t)} \quad \text{if} \quad t = \text{odd} \\ N(k,t) &= 0 \qquad\qquad\qquad\quad \text{if} \quad t = \text{even} \end{aligned} \tag{4.4}$$

and

$$\begin{aligned} A(k,t) &= C(e^{-Et} - e^{-E(L_t - t)}) \quad \text{if} \quad t = \text{even} \\ A(k,t) &= 0 \qquad\qquad\qquad\quad \text{if} \quad t = \text{odd}, \end{aligned} \tag{4.5}$$

where A, B and C were kept as free parameters, as was the energy E, which is expected to be the same for both (4.4) and (4.5). Fits were carried out using a non-linear least-squares method; details of the fitting procedure used are presented in appendix B.3. Table 4.1 lists the fitting windows used as well as the average χ^2/d.o.f over the 250 fits made per propagator per value of μ. As was to be expected, the quality of fits made to (4.4) with $L_t = 12$ was rather substandard, since when fitting 3 parameters over 5 data there are only 2 degrees of freedom. The situation seems markedly better when fitting (4.5), however, which has one fewer free parameter. For

$L_t =$	12		16		20	
Range fitted	$t \in [2, 11]$		$t \in [4, 13]$		$t \in [4, 17]$	
	$N(k,t)$	$A(k,t)$	$N(k,t)$	$A(k,t)$	$N(k,t)$	$A(k,t)$
$\mu = 0.0$	0.171	0.663	0.111	0.899	0.344	0.399
$\mu = 0.5$	53.383	1.279	4.492	0.751	7.110	0.813
$\mu = 0.6$	41.165	0.562	2.242	0.909	0.305	1.076
$\mu = 0.7$	35.131	0.773	2.209	0.440	3.307	0.641
$\mu = 0.8$	22.049	0.628	1.195	0.626	1.967	0.615
$\mu = 0.9$	1.772	0.940	1.007	0.956	1.087	0.836

Table 4.1: Average χ^2 per degree of freedom in fits to (4.4) and (4.5).

this reason it was decided that it was from these fits that we should extract $E(k)$ for all $\mu > 0$. Examples of fits to both (4.4) and (4.5) are illustrated in Fig. 4.2.

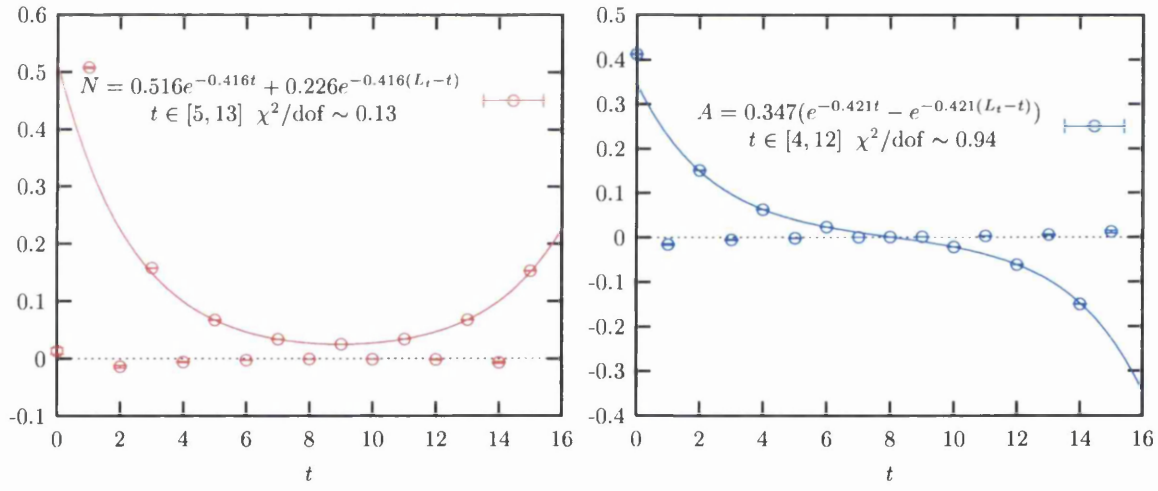

Figure 4.2: Normal and anomalous propagators with their fitted curves measured on a $96 \times 12^2 \times 16$ lattice at $\mu = 0.8$, with $j = 0.5$ and $k = 0.27\pi$.

The fit parameters from the $L_t = 12$, 16 and 20 lattices were extrapolated to $T \to 0$ for each value of μ and j in the same manner as $\langle qq_+ \rangle$ and R. The quality of the fits, however, was found to be quite poor, probably because of the small fitting window available for $L_t = 12$. In order to address this issue, a run was done with $L_t = 24$ at $\mu = 0.8$. This run took approximately 16 CPU days to generate 400

trajectories after equilibration using a 2.0GHz Intel Xeon processor machine. The average χ^2/d.o.f of the fits to the normal and anomalous propagators in the range $4 \leq t \leq 21$ were 1.384 and 0.907 respectively. The fit parameters for $\mu = 0.8$ were extrapolated to $T \to 0$ as before, this time through $L_t = 16$, 20 and 24, and the average χ^2/d.o.f. for these fits was found to fall from 7.53 to 0.32. Fig 4.3 shows some

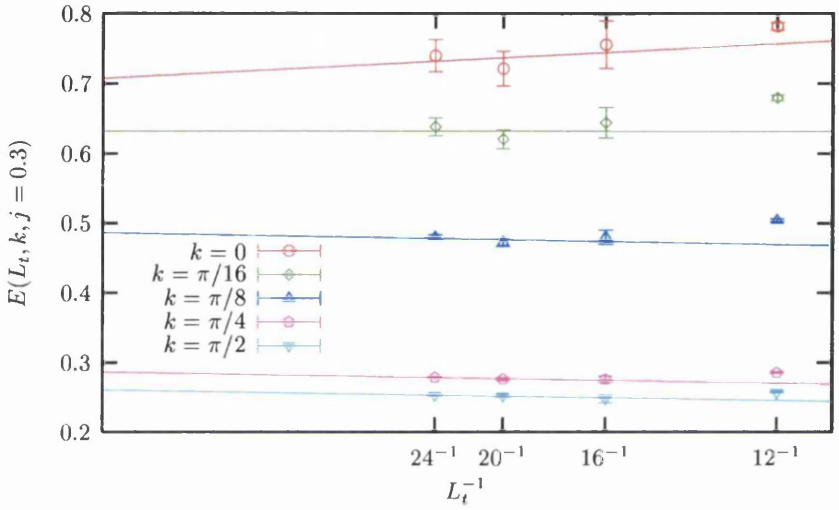

Figure 4.3: E extracted from $A(k,t)$ for $j = 0.5$ and various k. The solid lines depict fits through $L_t = 16$, 20 and 24.

example fits of E extracted from $A(k,t)$ and extrapolated to $T \to 0$. Whilst a $T \to 0$ extrapolation is seen to work well through $L_t \in [16, 24]$, the $L_t = 12$ point clearly does not fit, confirming that this is not long enough a temporal extent from which to accurately extract the energy.

Some example plots of the free parameters in (4.4) and (4.5) at $\mu = 0.8$, extrapolated to $T \to 0$, are depicted in Fig. 4.4. These were, in turn, extrapolated to $j \to 0$. Quadratic polynomial curves were fitted to the coefficients $A(k)$, $B(k)$ and $C(k)$, whilst the energy $E(k)$ was fitted with a straight line. As with the extrapolations of $\langle qq_+ \rangle$ and R in the previous chapter, the quality of the extrapolations appear to

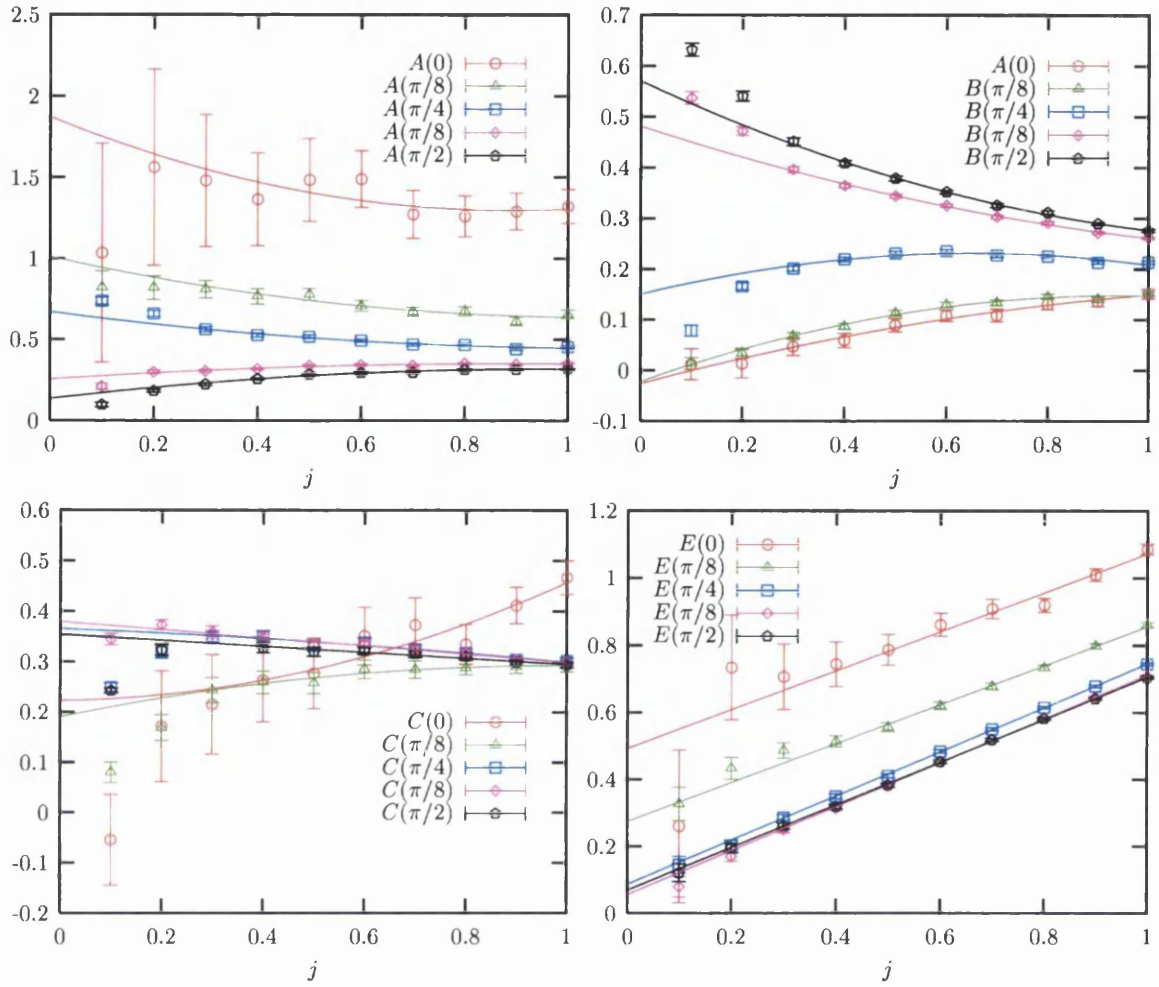

Figure 4.4: Zero temperature propagator parameters at $\mu = 0.8$ and various k. The solid curves show extrapolation to $j \to 0$.

smoothly fit the data except for at low j, where the discrepancy we have attributed to a finite volume effect persists. Again, for the purpose of the extrapolations, points with $j < 0.3$ have been ignored.

Now that we have established the correct way to extract the energy E and coefficients A, B and C at both zero temperature and diquark source strength, let us investigate their k dependence.

4.2 The Vacuum Dispersion Relation

Before we concern ourselves with $\mu > 0$, let us investigate the nature of the dispersion relation in the familiar case of the vacuum. In order to allow the $T \to 0$ extrapolation to be done accurately, another data set was generated with $L_t = 24$. Being in the chirally broken phase, this run was considerably faster than that at $\mu = 0.8$, however, taking only $5\frac{1}{2}$ CPU days to generate 400 equilibrated trajectories.

When $\mu = 0$, the time reversal symmetry of the lattice is restored, the coefficients A and B become identical and (4.4) reduces to its usual form of $|N(k,t)| = A(e^{-Et} + e^{-E(L_t - t)})$. This was checked and A and B were found to be equal, within errors, for all four values of L_t. The resulting dispersion relation, extrapolated to zero temperature

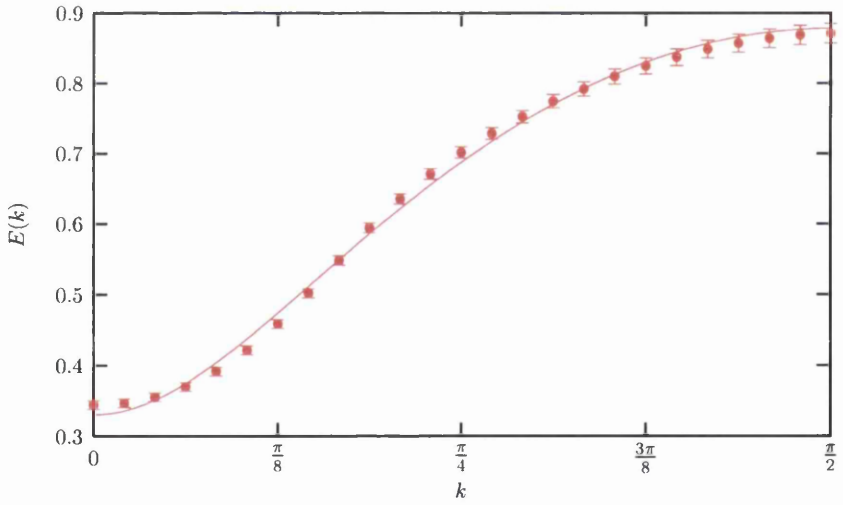

Figure 4.5: The vacuum dispersion relation $E(k)$ extrapolated to $T \to 0$ and then $j \to 0$. The solid curve is a fit to $\sinh^2 E = \alpha^2 \sin^2 k + m^{*2}$.

through $L_t = 16$, 20 and 24 and then to $j \to 0$, is plotted in Fig. 4.5. This curve was fitted to the free staggered fermion dispersion relation [55]

$$\sinh^2 E = \alpha^2 \sum_{i=1}^{3} \sin^2 k_i + m^{*2}, \tag{4.6}$$

where m^* is the dynamical fermion mass, and α is a free parameter. The curve is consistent with a system with no Fermi surface and a dynamically generated fermion mass m^*. It should be noted that the spectral fermion mass extracted from (4.6), $m^* \equiv \sinh E(k=0) = 0.351(6)$, differs from the expectation value of the scalar field $\Sigma \equiv \langle\sigma\rangle \sim 0.48$ due to $\mathcal{O}(1/N_c)$ effects. We also found $\alpha \simeq 1$, meaning there is no significant thermally induced modification to the speed of light on the lattice, as one would expect at $T = 0$.

4.3 $\mu = 0.8$: Measurement of the Gap

In this section, results are presented for the dispersion relation in the chirally restored phase. We shall concentrate on results at $\mu = 0.8$, since this is the only non-zero value of chemical potential for which we have successfully extrapolated results to zero temperature and diquark source strength. Fig. 4.6 shows the parameters $A(k)$, $B(k)$ and $C(k)$ extracted from the propagator fits and extrapolated first to $T \in [16^{-1}, 24^{-1}] \to 0$ and then $j \in [0.3, 1.0] \to 0$.

$A(k)$ and $B(k)$ represent the forward- and backward-moving components of the normal propagator $N(k,t)$ respectively. For low momenta, representing excitations below E_F, propagation is dominated by the forward-moving signal, whilst the high momentum excitations above the E_F are dominated by backward propagation. In a system of free fermions the transition between these two regimes occurs sharply at the Fermi surface [38]. This means that one can use the point at which $A(k)$ and $B(k)$ cross to distinguish the Fermi momentum k_F in analogy to the coefficients u_k and v_k of the BCS ground-state

$$|\psi_{\mathrm{BCS}}\rangle = \prod_k \left(u_k + v_k c^\dagger_{k\uparrow} c^\dagger_{-k\downarrow}\right)\Big|\,0\Big\rangle, \tag{4.7}$$

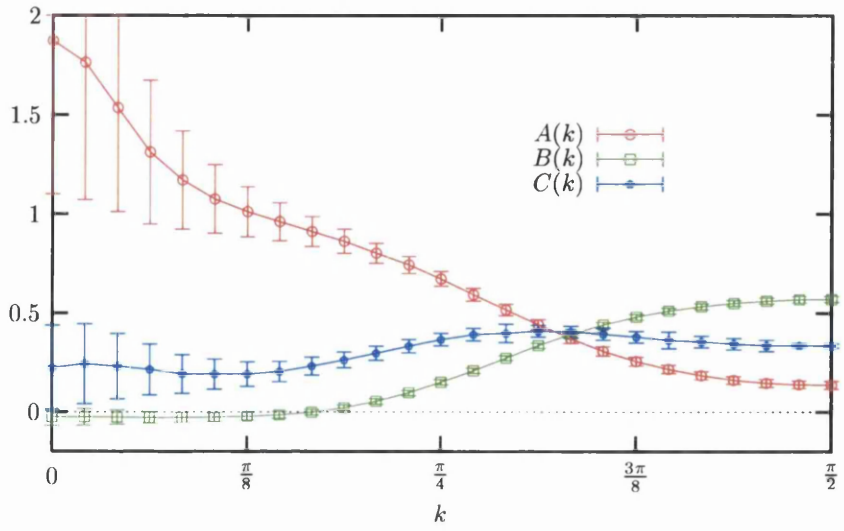

Figure 4.6: The propagator coefficients A, B and C for $\mu = 0.8$ extrapolated to $T \to 0$ and then $j \to 0$.

in which the operator $c^\dagger_{k\uparrow}$ creates an electron with momentum k and spin "up" from the vacuum $|0\rangle$. $|u_k|^2$ and $|v_k|^2$ represent, therefore, the probabilities of an electron pair with momenta $\pm k$ and spin $\uparrow\downarrow$ being filled and unfilled respectively [26]. The coefficient $C(k) \sim 0$ at low momentum, but becomes non-zero in a broad peak about the position of k_F. This non-vanishing of the anomalous propagator $A(k,t)$, even in the limit that $j \to 0$, is a clear signal of particle-hole mixing and, therefore, an indirect signal of the existence of a BCS gap $\Delta \neq 0$.

For more direct evidence, let us look at the dispersion relation $E(k)$, which is illustrated in Fig. 4.7. In the plot on the left, the red points are $E(k)$ at $\mu = 0.8$ extracted from (4.5) and extrapolated first to $T \in [16, 24] \to 0$ and then $j \in [0.3, 1.0] \to 0$. This is seen to disagree at intermediate k with data including $L_t = 12$, denoted by the green points, which justifies the statement made in section 4.1 that $L_t = 12$ is not large enough a temporal extent from which to extract $E(k)$ accurately. The blue curve represents the dispersion relation for free massless fermions

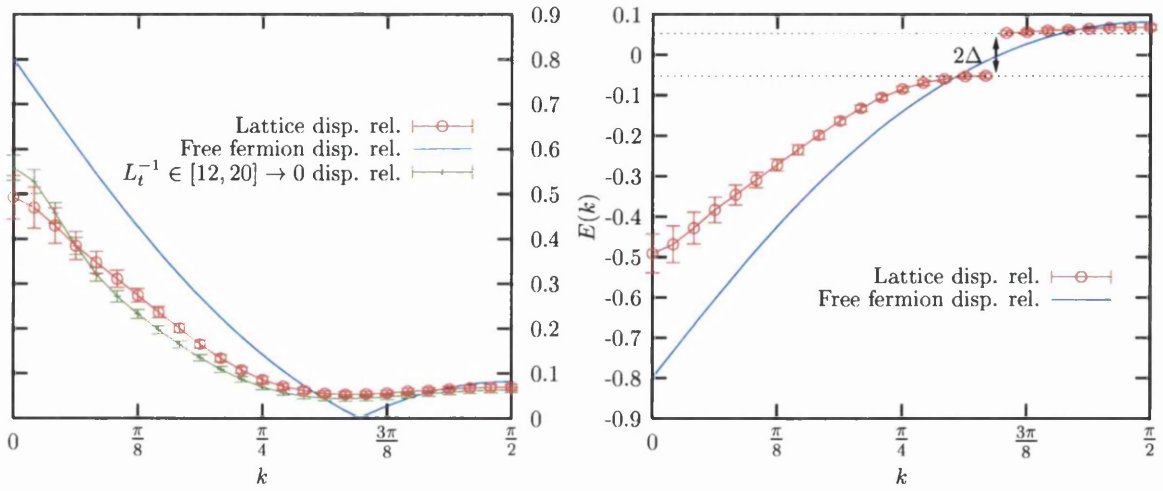

Figure 4.7: Lattice dispersion relation and typical free fermion dispersion relation at $\mu = 0.8$. In the right-hand figure the hole branch is plotted as negative.

on the lattice, similar to those observed in the $2+1d$ lattice Gross-Neveu model [56], and parameterised by $E(k) = \left|-\mu + \sinh^{-1}(\sin k)\right|$. This dispersion relation has two distinct parts, the hole-branch where $E(k)$ reduces with increasing k corresponding to excitations below E_F, and the particle-branch where $E(k)$ rises with k corresponding to excitations above E_F. In contrast to this, in the dispersion relation extracted from our lattice data, one can see no discontinuity between the two branches, which is another sign of particle-hole mixing. More importantly, at no point does $E(k)$ pass through $E = 0$ and there is a distinct gap between this point and the minimum; this is the BCS gap $\Delta = 0.053(6)$.

This can be seen in a more familiar light if one plots the hole branch as negative, which is done in the right-hand plot of Fig. 4.7. This makes the free fermion dispersion relation a smooth continuous curve, as one would expect in the continuum. For lattice data with no BCS gap the results are similar [38,56], whilst for our smooth dispersion relation this introduces a discontinuity, which looks exactly like a BCS gap in the

continuum. Furthermore, the point at which we introduce the discontinuity, which within the precision allowed by the momentum resolution is where the minimum of $E(k)$ occurs, is the same point at which $A(k)$ and $B(k)$ cross in Fig. 4.6. This confirms that the gap occurs at the Fermi momentum. Together, the non-vanishing anomalous propagator and the direct observation of the gap are the clearest evidence we have for the existence of a traditional BCS phase.

4.4 Chemical Potential Dependence of the Gap

Now that we have established the presence of a non-zero BCS gap at $\mu = 0.8$, it would be interesting to study how the size of the gap varies as a function of chemical potential. Unfortunately, the amount of CPU time needed to generated data in the chirally restored phase with $L_t = 24$ means that it was not plausible to repeat the analysis in the previous section for a wide range of μ. Instead, we took advantage of the data we had for $L_t = 16$ and 20, and made a rough estimate of the zero temperature limit by fitting a straight line through them. Since fitting a straight line through two points is not an overdetermined problem, there was no statistical means by which to assign the resulting $L_t^{-1} = 0$ intercept with an error. Instead we made a conservative estimate by varying the slope as much as possible within the two error bars and taking half the average difference between the resulting intercepts and the original one. The resulting values of $E(k, j)$ were extracted to $j \to 0$ as before with the quality of these fits being very good because of the large error bars through which the curves were fitted.

The reliability of the resulting relations was checked by comparing the data at $\mu = 0.8$ extracted using this method and the data extracted from a full statistical

analysis of $L_t = 16$, 20 and 24. As can be seen in Fig 4.8, the resulting dispersion relations are consistent within errors.

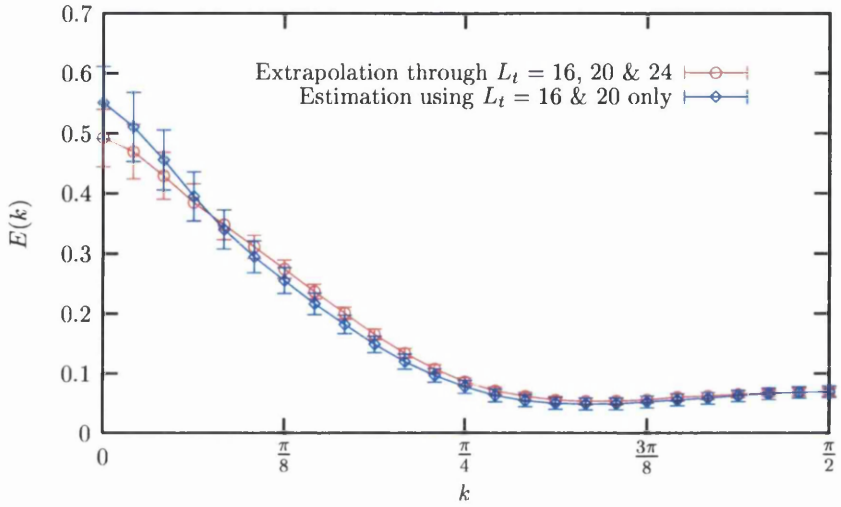

Figure 4.8: A comparison between the dispersion relations extracted with and without using $L_t = 24$ data.

Fig. 4.9 shows dispersion relations estimated from $L_t = 16$ and 20 for various values of chemical potential in the range $0.5 \leq \mu \leq 0.9$. For $\mu = 0.5$, which can be seen from Fig. 3.8 to be within the chirally broken phase, there is no clear sign of a Fermi surface and the observable gap, $E(k = 0) \neq 0$, is probably the remnants of the vacuum mass gap due to chiral condensation. As the chemical potential is increased however, both k_F and Δ rise clearly above zero. In the range $0.6 \leq \mu \leq 0.8$ there are parts of $E(k)$ that decrease and then increase with k, showing that the one has passed k_F, and a minimum value in between with $E(k) \neq 0$ corresponding to BCS gap Δ.

For higher values of chemical potential still, the dispersion relation only decreases with increasing k; this can be understood in terms of discretisation effects, which we shall discuss here at some length. Introducing the lattice spacing a, the free fermion

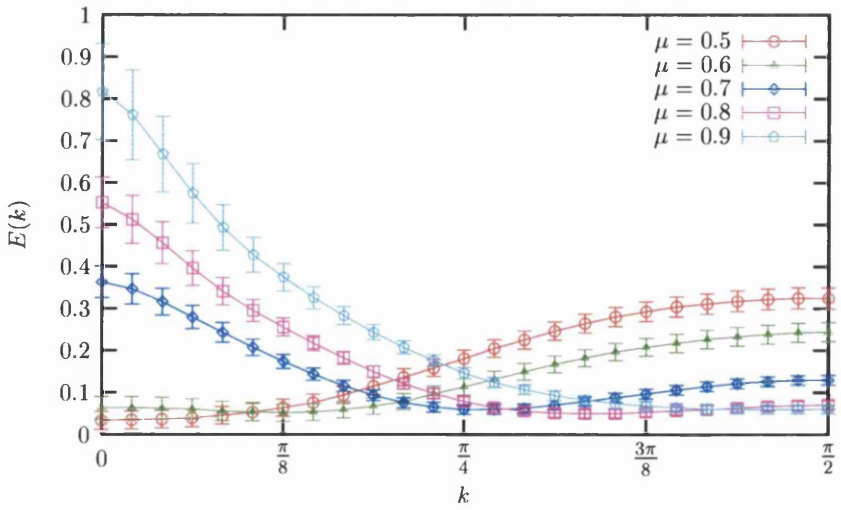

Figure 4.9: Lattice dispersion relation at various values of μ.

dispersion relation (4.6) implies that the Fermi surface is mapped out in momentum space via

$$\sinh^2 aE_F = \sum_{i=1}^{3} \sin^2 ak_{Fi} + (am^*)^2. \tag{4.8}$$

In the small angle approximation, observed for $k_{Fi} \ll \frac{\pi}{2a}$ and implied by taking the continuum limit $a \to 0$, this becomes

$$E_F^2 \approx \vec{k}_F.\vec{k}_F + m^{*2}, \tag{4.9}$$

which is the correct spherical relation for free fermions in the continuum. For fixed lattice spacing, however, as ak_{Fi} increases significantly from zero, the small angle approximation becomes invalid and the Fermi surface becomes distorted.

Fig. 4.10 shows the solution of (4.8) in momentum space in the zero temperature, infinite volume limit for various values of μ. In this limit, $E_F \equiv \mu$, and the lattice theory is defined continuously in momentum space within the periodic Brillouin zone $0 \leq k_{Fi} < \frac{\pi}{a}$. For the Fermion mass, the $T \to 0$ lattice results for the expectation

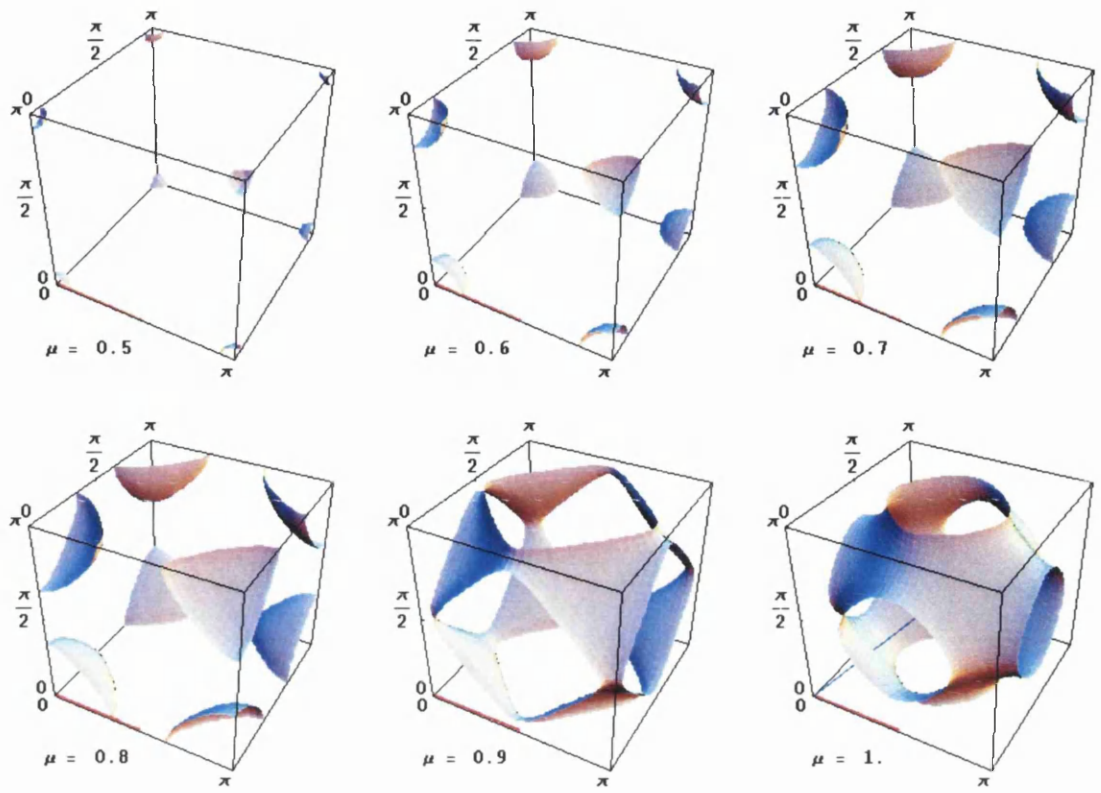

Figure 4.10: Solution of $\sinh^2\mu = \sum_i \sin^2 k_{Fi} + \Sigma^2$ for the zero temperature Fermi surface at various values of μ. The red lines signify the path along which $E(k)$ was measured.

value of the scalar field Σ have been used.[1] The red line on the k_x axis represents the path along which the dispersion relations plotted in Fig. 4.9 were measured, i.e. $\vec{k} = (k, 0, 0)$ with $0 \leq k \leq \frac{\pi}{2}$.

In the chirally broken phase, the approximately spherical Fermi surface grows slowly as the chemical potential is increased through the chiral crossover. In the chirally restored phase, for $\mu = 0.7$ and 0.8, the sphere becomes slightly distorted, but still intercepts the k_x axis such that our dispersion relation study can probe both

[1] Although this is an approximation, for the chemical potentials of interest this makes little quantitative difference, since in the chirally restored phase the fermion is approximately massless.

above and below E_F and detect the presence of the gap. Once μ approaches 0.9, however, the Fermi surface reaches the edge of the Brillouin zone and discretisation effects start to dominate. The Fermi surface meets itself in the periodic momentum space and "necks" away from the k_x axis. This explains why for $\mu > 0.8$ our dispersion relation study failed to find the BCS gap. Although the gap is almost definitely still there, since the maximum value of the diquark condensate was between $1.0 < \mu < 1.1$, our simple (and computationally inexpensive) choice of momenta to sample was not in the right direction to probe it. If one chose to study the more complicated path of $\vec{k} = (k, k, k)$ with $0 \leq k \leq \frac{\pi}{2}$, indicated by the diagonal blue line in Fig. 4.10, we believe that the BCS gap would be clear to observe for higher μ. A point of interest is that the lattice Fermi surface at $\mu = 1.0$ looks exactly like that of the conduction electrons in a simple cubic metal solved in the tight binding approximation [57], since the fact that fermions on the lattice are confined to lattice sites implies these are essentially solutions of the same problem.

Finally, Fig. 4.11 shows Δ and $\langle qq_+ \rangle$ as functions of μ in the range over which Δ could be measured on-axis. The most immediate observation is that whilst the diquark condensate increases with the area of the Fermi surface, once the BCS gap is formed its magnitude remains approximately constant with μ. Because of the rough method used to extract $\Delta(\mu)$, however, and the size of the errors caused by this, we can gain only qualitative information on the variation of Δ with μ.

To summarise the work presented in this and the previous chapter, we have seen evidence for diquark condensation leading to the existence of a BCS phase at high chemical potential in the form of a non-zero diquark condensate, a vanishing diquark susceptibility ratio and now a distinct gap in the dispersion relation about the Fermi

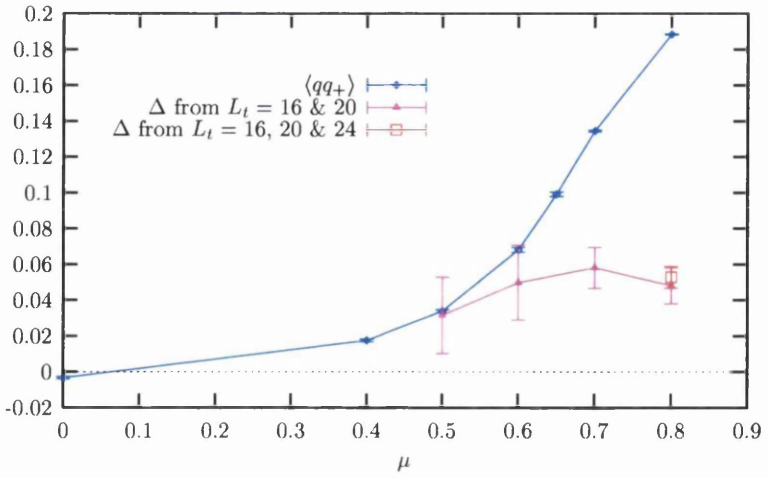

Figure 4.11: The BCS gap and diquark condensate plotted as functions of chemical potential.

surface. At $\mu = 0.8$ the size of the gap is 0.053(6) so the ratio between the BCS gap and the vacuum fermion mass is $\frac{\Delta|_{\mu=0.8}}{m^*|_{\mu=0.0}} = 0.15(2)$. Assuming the fermion has mass $m^* \sim 400\text{MeV}$, this means that in physical units the size of the gap is $\Delta \sim 60\text{MeV}$.

All of this evidence is reliant, however, on the discarding of data with $j < 0.3$, below which there is clear disagreement between lattice data and our extrapolation curves. In the next chapter we present an argument that ascribes this discrepancy to finite volume effects, implying that our curves represent the true solution in the infinite volume limit.

Chapter 5

Finite Volume Effects

5.1 Reaching the Infinite Volume Limit

When investigating any problem in lattice field theory, one must take into account the inherent systematic errors due to the discretisation and finite volume of space-time. Although we have chosen to work with a fixed lattice spacing, due to the triviality of the NJL model's continuum limit [41], it is still important to consider errors due to the finite size of the lattice. In this chapter, we argue that the discrepancy observed in variables in the diquark sector with $j < 0.3$ is due to such a finite volume effect. Furthermore, we argue that rather than being due to the divergence of a correlation length, this effect is due to the difficulty of representing a curved shell of states about the Fermi surface on a discrete lattice of momentum modes.

In general, when performing lattice simulations, one should ensure that any important mass scale Λ in one's theory satisfies

$$a \ll \Lambda^{-1} \ll aL, \tag{5.1}$$

where aL is the length of the smallest spatial dimension. If this condition is satisfied one may say that the systematic errors are under control, and safely extrapolate

to the continuum and infinite volume limits. When considering critical phenomena, however, such as the spontaneous breaking of an exact global symmetry, the matter becomes more complicated. As one approaches criticality, the correlation length ξ of the fluctuations of the order parameter diverges and becomes comparable to the size of the lattice; its associate mass scale $m \sim 1/\xi$ no longer satisfies (5.1).

A familiar example of this problem occurs in simulations of the massless lattice NJL model, which has an exact $SU(2) \otimes SU(2)$ chiral symmetry that is spontaneously broken to $SU(2)$ in the vacuum. The breaking of this symmetry leads to three massless Goldstone modes, i.e. the pions, such that their correlation lengths diverge. At strictly infinite volume, the order parameter for this symmetry breaking is the expectation value of the scalar field $\langle\sigma\rangle$, whilst the pseudo-scalar fields $\langle\pi_i\rangle$ average to zero. Although at finite volume the magnitude of the order parameter $\rho = \sqrt{\sigma^2 + \vec{\pi}.\vec{\pi}}$ remains non-zero, it costs negligible energy to change the direction of symmetry breaking from configuration to configuration such that both $\bar{\sigma} \equiv \frac{1}{V}\sum_{\tilde{x}} \sigma(\tilde{x})$ and $\bar{\pi} \equiv \frac{1}{V}\sum_{\tilde{x}} \vec{\pi}(\tilde{x})$, where V is the lattice volume, average to zero over the ensemble; the system can no longer truly be said to have a broken symmetry. Apart from the lack of a true order parameter, this leads to an additional problem, in that the volume of phase space representing configurations in equilibrium now contains configurations with ρ pointing in an arbitrarily large number of directions. This means that the HMC algorithm has to sample a larger volume of phase space and has to run much longer to produce correlated measurements of observables.

If one explicitly breaks the symmetry by introducing a small bare quark mass m_0, however, this fixes the direction of symmetry breaking. One may then study the order parameter in the limit that $m_0 \to 0$. An example of this is illustrated in

Fig. 5.1, where $\Sigma \equiv \langle\sigma\rangle$ is plotted as a function of m_0 as measured in simulations on a 12×6^3 lattice. One can see that whilst Σ follows a general trend for most values

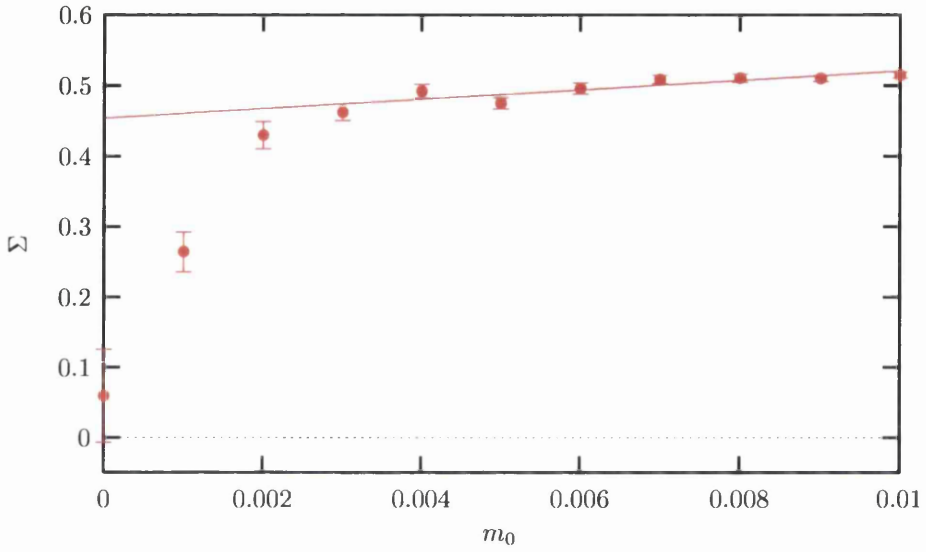

Figure 5.1: Expectation value of the scalar field as a function of the bare quark mass at $\mu = 0$ on a 12×6^3 lattice.

of m_0, below some cut-off value, i.e. as ξ increases through aL, the expectation value drops off sharply to zero.

The resulting curve appears very similar to those of e.g. $\langle qq_+\rangle$ vs. j in Fig. 3.7, where below $j = 0.3$ the order parameter approaches zero sharply. The divergence of the correlation length, then, seems an obvious explanation for the strange behaviour of R, $\langle qq_+\rangle$ and E below this value of j, since if the true high-density ground-state were that of a BCS superfluid, the spontaneously broken $U(1)_B$ symmetry would lead to an exact Goldstone mode. Results of a systematic study of finite volume effects, however, indicate that there may be a different explanation.

5.2 Finite Volume Study

To investigate the possibility that the low-j discrepancies in Figs. 3.6, 3.7 and 4.4 were due to finite volume errors, it was necessary to study spatial volume dependence in a controlled manner. $\langle qq_+ \rangle$ was measured for the values of j used previously, on all $L_s^3 \times L_t$ lattices with L_s = 6, 8, 10, 12, 16 and 20 and L_t=12, 16 and 20 for fixed $\mu = 1.0$. Being both well into the high-μ phase and far from the transition, any finite size effects should be easily identifiable. The data were generated using the parameter set used in [58], i.e. $\beta = 0.565$ and $am_0 = 0.002$.

These data were extrapolated to infinite temporal extent, corresponding physically to zero temperature, using the fact that the dominant finite size correction in the data was proportional to L_t^{-1}. Fig. 5.2, however, does illustrate that there is some residual L_s dependence.

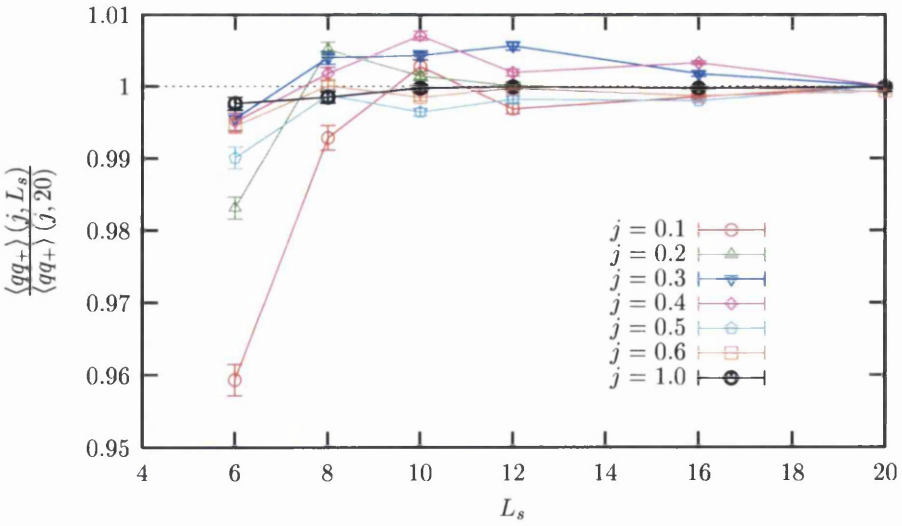

Figure 5.2: $\langle qq_+ \rangle$ in the zero temperature limit as a function of the spatial extent of the lattice. The results are normalised such that $\langle qq_+ \rangle|_{L_s=20} \equiv 1$.

$\langle qq_+ \rangle$ is plotted as a function of spatial extent for various values of j, with data

presented as fractions of $\langle qq_+ \rangle|_{L_s=20}$ to enable them to be displayed on the same axes. For $j \geq 0.5$ and $L_s \geq 12$, the effect is negligible; the data are consistent within errors. For $j < 0.5$, however, we observe non-monotonic fluctuations, whose magnitude increases with decreasing j. These finite volume effects do not resemble

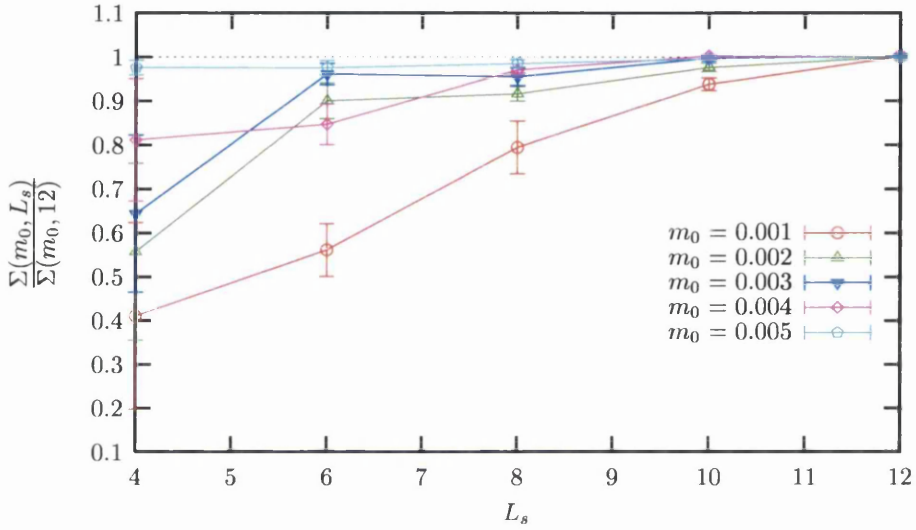

Figure 5.3: Σ measured on $L_t = 12$ lattices as a function of their spatial extent at $\mu = 0.0$. The results are normalised such that $\Sigma|_{L_s=12} \equiv 1$.

those expected from the standard treatment of Goldstone fluctuations, where any shifts due to finite size are expected to be monotonic [59].

An example of finite size effects due to such Goldstone fluctuations is illustrated in Fig. 5.3, where the expectation value of the scalar field in the vacuum Σ, which is the order parameter for the breaking of $SU(2)_L \otimes SU(2)_R \to SU(2)_V$, is plotted against the spatial extent of the lattice for various values of the bare quark mass. This was measured on $L_s^3 \times L_t$ lattices with fixed $L_t = 12$ and $L_s = 4$, 6, 8, 10 and 12. Again, the data are presented as fractions of the order parameter measured on the largest volume used to allow the results for different masses to be plotted on the same axes.

Not only are these finite size effects larger than those observed in Fig. 5.2, they are monotonic, within errors, as expected. Furthermore, Fig. 5.1 shows that these effects become significant only below $m_0 = 0.003$, which is a factor of a hundred smaller than the equivalent value for j on a lattice half the size of the smallest one treated in chapter 3. This suggests that whilst the spontaneous breaking of the global $U(1)_B$ symmetry in the high-μ phase should cause some finite size effects, the discrepancy observed for $j < 0.3$ is due to some other, more dominant effect.

5.3 The Lattice Fermi Surface

One source of finite volume effects that would not have been present in previous lattice studies is due to the fact that we have tried to represent a system with a Fermi surface. Although the nature of the discretised Fermi surface was discussed briefly in chapter 4, the smooth curves in Fig. 4.10 only represent the surface in the infinite volume limit. In a finite volume system at zero temperature, the Brillouin zone is discretised into a cubic momentum lattice with lattice spacing $2\pi/(L_s a)$.

One consequence of this is that when the chemical potential $\mu = E_F|_{T=0}$ is increased smoothly, the Fermi-Dirac distribution changes only when the Fermi surface crosses a momentum mode. If one were to study a transition, therefore, such as the chiral crossover illustrated in Fig. 3.2, the physics of the system would be constant except at these points where the surface crosses a mode; the transition would be turned into a series of steps. As the temperature is increased from zero, however, the Fermi-Dirac distribution is smeared out across a region $\delta k \sim T$, and if this becomes larger than $2\pi/(L_s a)$, the transition once again becomes smooth.

For lattices with $L_t \gg L_s$, the smearing of the Fermi surface is too fine to be

resolved on the coarse momentum lattice and this finite volume effect is observable directly. Fig. 5.3 illustrates Σ as a function of μ measured on a 48×10^3 lattice via both direct lattice simulations and solution in the large-N_c limit. The vertical lines

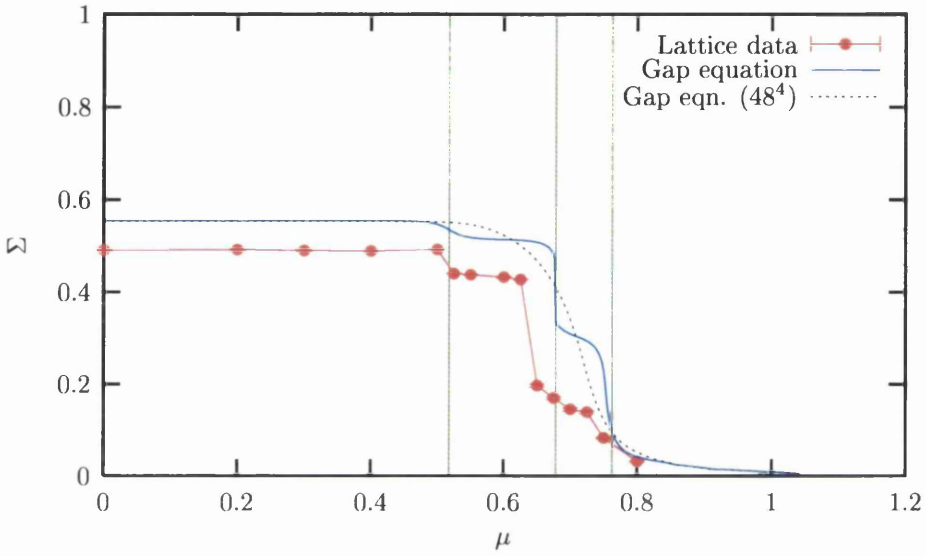

Figure 5.4: Lattice results and large-N_c solution for Σ as a function of chemical potential on a 48×10^3 lattice. The vertical lines show where the Fermi surface crosses a lattice site in the large-N_c limit.

represent the three lowest-lying solutions of $\mu = \sqrt{\sum_{i=1}^{3} \sin^2 k_i + m^{*2}}$ that have k_i coincident with modes of the momentum lattice, where m^* was taken from the large-N_c solution. As expected, the resulting curve in the large-N_c limit is one made up of a series of smeared out steps occurring exactly at these points. Comparing this with the lattice data, as previously, we see $\mathcal{O}(1/N_c)$ corrections of about 15% but qualitatively the curves are in complete agreement. The dashed curve shows that as the volume is increased once more, and $L_t \sim L_s$, the transition returns to its expected form.

Let us now consider the effect that the discretisation of the Brillouin zone could have on results in the diquark sector. A physical interpretation of $\langle qq_+ \rangle$ is that it

counts the density of qq pairs participating in diquark condensation. If one makes the simple-minded assumption that these states lie at momentum modes in some shell with thickness $\mathcal{O}(\Delta)$ about the Fermi surface, one can see how the geometry of the gap and the lattice become important. Since the source term in the introduction of j induces diquark condensation, and hence increases the size of the gap, one should always be able to make j large enough for a significant number of momentum modes to contribute to $\langle qq_+ \rangle$. As j is decreased, however, one can picture that for some small volume, the momentum-mode lattice may be coarse enough for the number of participating modes, and hence the value of the diquark condensate, to drop significantly.

This simple argument was investigated quantitatively by counting the number of momentum modes lying between continuous Fermi surfaces with $E_F = \mu \pm \Delta$, representing the region of the BCS gap. This was done for a chemical potential of 0.8, on an array of lattice volumes and shell thicknesses. The results, plotted in Fig. 5.3, show that for small volumes and thin shells, the number of modes within the shell varies sporadically and non-monotonically with the spatial extent of the lattice, meaning that this could well be the cause of the discrepancy below $j = 0.3$.

The plot for $\Delta = 0.08$, in particular, is reminiscent of results from a variational study of the $N_f = 2$, $N_c = 3$ continuum NJL model with no diquark source at zero temperature in a finite cubic spatial volume [60]. In this study, it was found that a spatial extent of 7fm ($\sim$ 30 lattice spacings) was required before the model approximated its infinite volume limit, whilst below this volume the order parameter was found to oscillate rapidly about its solution in the thermodynamic limit.

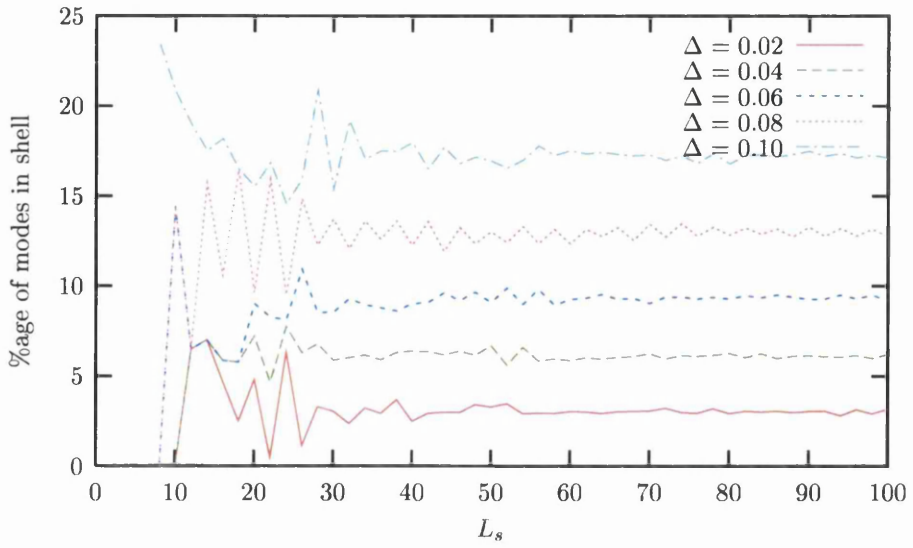

Figure 5.5: Number of momentum modes within a shell of thickness $\delta E = 2\Delta$ as a function of spatial lattice volume at $\mu = 0.8$.

Although this may explain why, with a small source the number of qq pairs condensing may be suppressed, the best way to validate our technique for extrapolation to $j \to 0$ would be to show that for very large lattices, the depletion of diquark condensation is significantly reduced.

5.4 Large-volume Study

Whilst simulation of the NJL model on lattices much large than 20^4 is currently beyond the capability of desktop personal computers, it should be possible to carry out such simulations on a PC cluster or a commercial supercomputer. In particular, it has been possible to secure time on the Sun Galaxy-class supercomputer at the Cambridge-Cranfield High Performance Computing Facility (HPCF), meaning that simulation on such volumes is within reach. Initial simulations have been performed

on both 36^4 and 48^4 lattices and the code was found to run without problems. Unfortunately, due to the length of time it has taken for the run parameters to be tuned for high acceptance and for the initial configurations to reach equilibrium, measurements have yet to be taken, and the results of these runs cannot be published in this volume.

For this reason, our claim to have observed a BCS phase in lattice simulations must remain provisional until the behaviour of data with $j < 0.3$ has been accounted for.

Chapter 6

The Strength of the Gap

6.1 Non-zero Isospin Chemical Potential

In previous chapters, we have demonstrated using non-perturbative methods, outstanding finite volume issues aside, that the ground-state of the NJL model with two degenerate flavours at high baryon chemical potential and zero temperature exhibits BCS superfluidity. The method of pairing in this system between quarks of opposite momenta and isospin, directly analogous to 2SC pairing between up and down quarks, is not only simple, but particularly energetically favourable. If the system were non-interacting, it would cost no energy to create a pair of quarks at the common Fermi surface of the degenerate flavours, such that when the attractive interaction is restored, the system is expected always to be unstable to diquark condensation and the formation of a BCS state [61].

In the real world, however, the Fermi momenta k_F^u and k_F^d for up and down quarks respectively are expected to differ. For instance, a simplistic argument outlined in [62] and simplified further here to describe a two flavour system, suggests that in compact stellar matter, k_F^u should be less than k_F^d. In particular, for massless non-interacting matter with baryon chemical potential $\mu_B = 400\text{MeV}$, an electron chemical potential

$\mu_e = 89\text{MeV}$ is necessary to enforce charge neutrality and that weak interactions be in chemical equilibrium. Together, these two conditions determine all the chemical potentials and Fermi momenta:

$$\begin{aligned} k_F^u &= \mu_u = \mu_B - \tfrac{1}{2}\mu_e = 355.5\text{MeV}, \\ k_F^d &= \mu_d = \mu_B + \tfrac{1}{2}\mu_e = 444.5\text{MeV}, \\ k_F^e &= \mu_e = 89\text{MeV}. \end{aligned} \tag{6.1}$$

The effect of separating the free-particle Fermi surfaces of pairing quarks should be to make the superconducting phase less energetically favourable. This proves a good method, therefore, to investigate the stability of the superfluid phase.

This effect was first investigated not long after the original BCS theory was proposed, in the context of superconductors with k_F for spin up and spin down electrons separated due to Zeeman splitting in an external B field. It was found that below some critical separation, the ground-state is one with coincident Fermi surfaces and a gap equal to that in a system with no splitting. At the critical separation, however, the system was found to go through a first order transition to a phase with two distinct Fermi surfaces and no superconductivity [63, 64].

The simplest way to separate the Fermi surfaces of different flavoured quarks in a QCD-like theory is via the introduction of an isospin chemical potential μ_I, which c.f. $\frac{1}{2}\mu_e$ in (6.1), separates the chemical potentials of up and down quarks by $\delta\mu = 2\mu_I$. This analysis was applied to the 2SC superconducting phase in [65], where the effect of setting $\mu_I \neq 0$ was investigated in a mean-field four Fermi model. Whilst the conclusion was similar to those of [63] and [64], the size of the gap was found to increase slightly under small flavour asymmetries, prior to the first order transition to a gapless phase, an effect attributed to the colour structure extracted from one gluon exchange in QCD. In this model, diquark condensation occurs between quarks

of only two colours, leaving quarks of the third colour without a gap in their spectrum; if the separation in Fermi surfaces is smaller than the size of the gap, the asymmetry has little effect on the condensate and the response of $\Delta(\mu_I)$ is dominated by the dynamics of the spectator quarks. This analysis was extended further to include systems in which the Fermi surfaces k_F^u and k_F^d are separated not only by an isospin chemical potential, but a fixed momentum $\vec{q}$ [61]. In such a system, when μ_I and $\vec{q}$ are sufficiently large that the Fermi surfaces cross, Pauli blocking implies that 2SC becomes less favourable than a state in which diquark condensation occurs only at a ring of states close to the intercept of the surfaces. The state is one with broken translational and rotational invariance, in which the diquark pairs have non-zero total momentum; this is known as the LOFF phase [66, 67].

In addition to these studies of colour superconductivity, the effect of introducing a small isospin chemical potential on the chiral structure of the QCD phase diagram has been recently investigated [68]. This analytic study of the standard NJL model has shown that setting $\mu_I \sim 30$MeV causes the chiral phase transition to split into two, one transition for the condensate of each quark flavour. It has been argued, however, that this effect would not be observed in nature, since the introduction of an instanton motivated flavour mixing vertex with even fairly weak coupling has been shown to restore the model to having a single transition [69].

In lattice calculations, the inclusion of a non-zero isospin chemical potential has predominantly been regarded as yet another means of investigating the low density, high temperature region of the QCD phase diagram, since with $\mu_I \neq 0$ and $\mu_B = 0$ the fermion determinant is real [70, 71]. A lattice motivated theory with both $\mu_{B,I} \neq 0$ has been investigated, however, in 2 colour, 2 flavour QCD, for which $\det M$ is real

and positive for either $\mu_{B,I} \neq 0$. In this theory, analytic calculations have shown that whilst for $\mu_B \gg \mu_I \sim 0$ standard $\langle ud \rangle$ condensation remains, as μ_I is increased the theory passes through a small phase with $\langle uu \rangle$ and $\langle dd \rangle$ condensation, which breaks rotational invariance as in the LOFF phase [72]. Unfortunately, even in this theory the fermion determinant is not positive definite if both $\mu_{B,I} \neq 0$, so simulation is limited to the $N_f = 4$ case, in which this phase is believed not to persist [72].

6.2 Quenched Simulations with $\mu_I \neq 0$

In this section we discuss the results of some initial simulations of the lattice NJL model with both $\mu_{B,I} \neq 0$ with the objective of investigating the effect this has on the model's order parameters, and in particular the stability of the BCS phase. Whilst this is the first attempt to study a lattice model with non-degenerate Fermi surfaces, these simulations are limited in that we have chosen to set $\mu_I \neq 0$ only during the measurement of observables. Before this is discussed further, however, let us address how this introduction affects the formulation of the lattice model outlined in chapter 2.

In the NJL model, diquark pairing occurs via 2SC-style condensation between quarks of opposite isospin, which in our lattice model are the two components of the staggered fermion field,

$$\chi_x \equiv \begin{pmatrix} \chi_1(x) \\ \chi_2(x) \end{pmatrix} = \begin{pmatrix} u(x) \\ d(x) \end{pmatrix}. \tag{6.2}$$

From hereon we shall refer to these as "up" and "down" quark flavours. The Fermi surfaces of the pairing partners can be separated by directly allocating them different chemical potentials, μ_u and μ_d, which is equivalent to having non-zero baryon chemical

potential $\mu_B = \frac{1}{2}(\mu_u + \mu_d)$ and isospin chemical potential $\mu_I = \frac{1}{2}(\mu_u - \mu_d)$ simultaneously.[1] In the physical context of compact stars, these two scales should be ordered $\mu_B \gg \mu_I$, since the simple argument leading to (6.1) predicts that $\frac{1}{2}|\mu_u - \mu_d| \sim 0.1\mu_B$.

With this introduction, the fermion kinetic operator M becomes

$$\begin{aligned} M^{pq}_{xy} &= \frac{1}{2a}\left(e^{a\mu_B}(e^{\tau_3 a\mu_I})^{pq}\delta_{yx+\hat{0}} - e^{-a\mu_B}(e^{-\tau_3 a\mu_I})^{pq}\delta_{yx-\hat{0}}\right) \\ &+ \frac{1}{2a}\delta^{pq}\left[\sum_{\nu=1}^{3}\eta_\nu(x)\left(\delta_{yx+\hat{\nu}} - \delta_{yx-\hat{\nu}}\right) + 2am_0\delta_{xy}\right] \\ &+ \frac{1}{16}\delta_{xy}\sum_{\langle\tilde{x},x\rangle}\left(\sigma(\tilde{x})\delta^{pq} + i\epsilon(x)\vec{\pi}(\tilde{x}).\vec{\tau}^{pq}\right). \end{aligned} \tag{6.3}$$

Unfortunately, the proof that $\det M$ is both real and positive outlined in chapter 3 no longer applies, since it relies on the fact that $\tau_2 M(\mu_I = 0)\tau_2 = M^*$. It is simple to show using the Pauli-Gürsey identity

$$\tau_2\tau_i\tau_2 \equiv -\tau_i^*, \tag{6.4}$$

and its generalisation to matrix exponentials

$$\tau_2 e^{\alpha\tau_i}\tau_2 = e^{\alpha\tau_2\tau_i\tau_2} = e^{-\alpha\tau_i^*}, \tag{6.5}$$

that

$$\begin{aligned} \tau_2 M^{pq}_{xy}\tau_2 = \frac{1}{2a}&\left(e^{a\mu_B}(e^{-\tau_3 a\mu_I})^{pq}\delta_{yx+\hat{0}} - e^{-a\mu_B}(e^{\tau_3 a\mu_I})^{pq}\delta_{yx-\hat{0}}\right) \quad \neq M^{pq*}_{xy}. \\ &+\frac{1}{2a}\delta^{pq}\left[\sum_{\nu=1}^{3}\eta_\nu(x)\left(\delta_{yx+\hat{\nu}} - \delta_{yx-\hat{\nu}}\right) + 2am_0\delta_{xy}\right] \\ &+\frac{1}{16}\delta_{xy}\sum_{\langle\tilde{x},x\rangle}\left(\sigma(\tilde{x})\delta^{pq} - i\epsilon(x)\vec{\pi}(\tilde{x}).\vec{\tau}^{pq*}\right) \end{aligned} \tag{6.6}$$

[1] Although this definition implies that $\mu_u > \mu_d$, which is contrary to the conclusions of the argument outlined above, this notation has been chosen to be consistent with that of [68] and [69]. Since, the NJL model does not include the effects of weak interactions and is therefore isospin invariant, this has no effect since the labels of "up" and "down" are interchangeable.

Although this would not cause our simulation algorithm to fail, since we use $\det M^\dagger M$ as the fermionic part of the measure, the fact that this choice is the only reason the algorithm works implies that there are some important interactions between the quarks and conjugate quarks contained in M and $M^\dagger$ respectively. If we were to perform simulations with this new measure as is discussed in [72], the theory would then have $N_f = 4$ and $N_c = 4$, rather than the $N_f = 2$ and $N_c = 8$ of the model hitherto investigated. By studying this model, therefore, one could not learn of the strength of the gap measured in chapter 4. Instead, it was chosen to simulate in the quenched isospin limit in which $\det M^\dagger M$ was calculated with $\mu_I = 0$ in the HMC update of the bosonic fields, whilst (6.3) was used in $\mathcal{A}$ during the measurement of observables.

Before we discuss the effect of having $\mu_I \neq 0$ on the BCS phase, let us examine the effect this introduction has on the chiral phase transition. Fig. 6.1 illustrates the up and down quark chiral condensates

$$\langle \bar{u}u \rangle \equiv \frac{1}{V}\frac{\partial \ln \mathcal{Z}}{\partial m_u} = \frac{1}{4V}\left\langle \eta^\dagger \begin{pmatrix} 0 & 0 & 1 & 0 \\ 0 & 0 & 0 & 0 \\ -1 & 0 & 0 & 0 \\ 0 & 0 & 0 & 0 \end{pmatrix} \mathcal{A}^{-1}\eta \right\rangle \tag{6.7}$$

and

$$\langle \bar{d}d \rangle \equiv \frac{1}{V}\frac{\partial \ln \mathcal{Z}}{\partial m_d} = \frac{1}{4V}\left\langle \eta^\dagger \begin{pmatrix} 0 & 0 & 0 & 0 \\ 0 & 0 & 0 & 1 \\ 0 & 0 & 0 & 0 \\ 0 & -1 & 0 & 0 \end{pmatrix} \mathcal{A}^{-1}\eta \right\rangle \tag{6.8}$$

as functions of μ_B for various μ_I measured on a 12^4 lattice. Although these results have been measured on only one lattice volume, the speed of these simulations meant that is was possible to gain fine resolution in μ_B. Consistent with the predictions

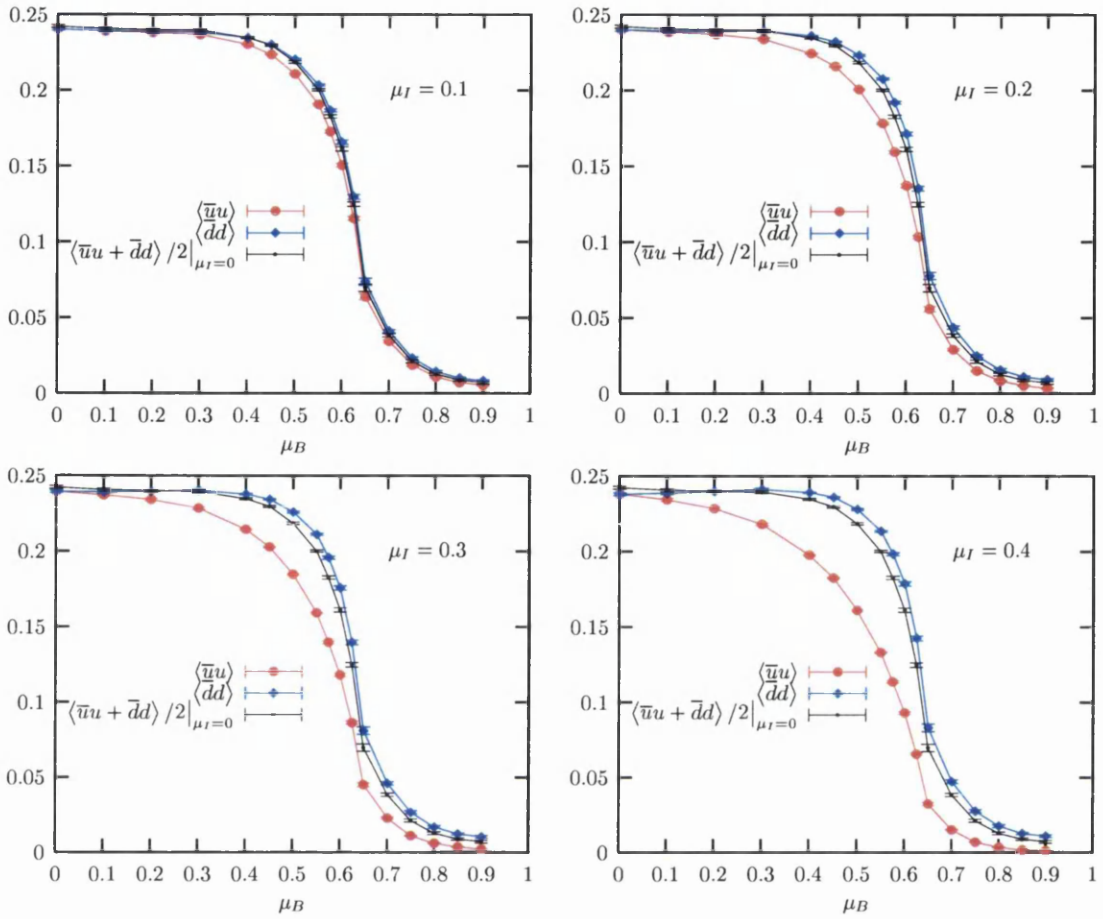

Figure 6.1: $\langle \bar{u}u \rangle$ and $\langle \bar{d}d \rangle$ condensates for various μ_B and μ_I on a 12^4 lattice.

of [68], the two transitions, which are coincident in the limit that $\mu_I \to 0$, separate as μ_I is increased. This can be understood by noting that for fixed μ_I the chemical potential of the up quark is larger than that of the down, such that the up quark reaches the critical chemical potential first. It is not clear, however, why the curve of the up condensate deviates from the $\mu_I = 0$ solutions more than that of the down. This effect, not predicted in [68] could be some lattice artifact, but may well be a result of the crudeness of the quenched approximation.

Of more interest than the quark condensates, which are diagonal in flavour and

therefore not fundamentally affected by the separation of the Fermi surfaces, is the response in the diquark condensate to the introduction of an isospin chemical potential. In this section we relabel the order parameter $\langle qq_+ \rangle$ defined in (3.21) as $\langle ud \rangle$, to emphasise the fact that condensation occurs between quarks of different flavours, i.e. of opposite isospin. Fig. 6.2 illustrates the $\langle ud \rangle$ condensate measured at $\mu_B = 1.0$ on

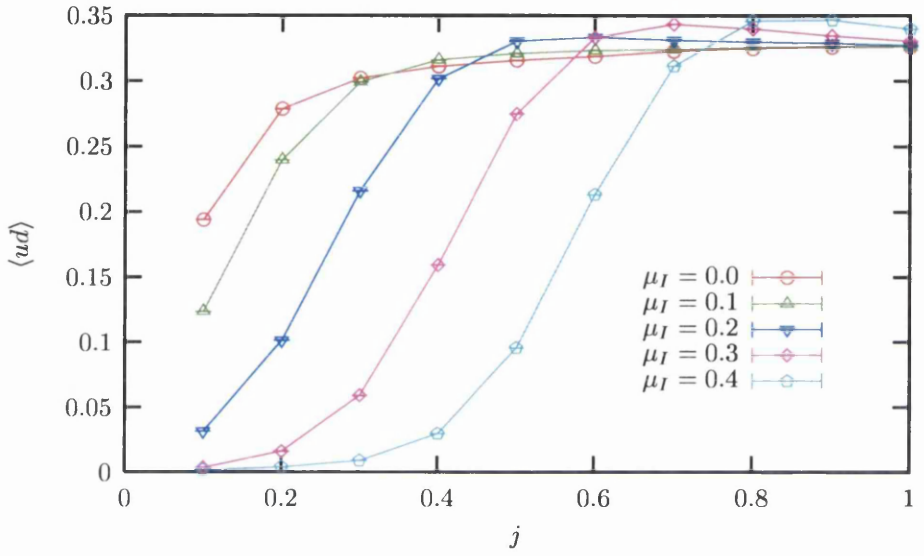

Figure 6.2: $\langle ud \rangle$ condensate as a function of j for various μ_I with $\mu_B = 1.0$.

12^4, 16^4 and 20^4 lattices as a function of j for various values of μ_I. Results have been extrapolated to $T \to 0$ as before. As expected, the effect of significantly increasing μ_I for fixed j is to suppress condensation, an effect that is more pronounced at smaller values of j. An effect that is less straightforward to understand is that prior to this suppression, the values of $\langle ud(j) \rangle$ appear to increase slightly.

Looking at the response of the curves to varying j, one might argue that the curves for $\mu_I > 0.1$ appear to represent transitions between a phase in which j, and hence the interaction between paired quarks, is sufficiently large to overcome the suppression due to having $\mu_I \neq 0$ and one in which it is not. In this case, it is unclear how one

should take the $j \to 0$ limit to retrieve results for the sourceless model.

Another interpretation of Fig. 6.2 could be that the effect of increasing μ_I is to reduce the size of the gap about k_F, which would accentuate any finite volume problems due to a coarse lattice of momentum-modes, and cause the suppression of $\langle ud \rangle$ to occur at $j > 0.2$.

Assuming this presumption could be taken seriously, one could fit curves analogous to those in Fig. 3.7 to a decreasing number of j values with increasing μ_I, and see how $\langle ud \rangle|_{j\to 0}$ varies with μ_I. Such fits were made and the resulting curves are plotted in Fig. 6.3. The resulting trend is the same as that at intermediate fixed j, i.e. the

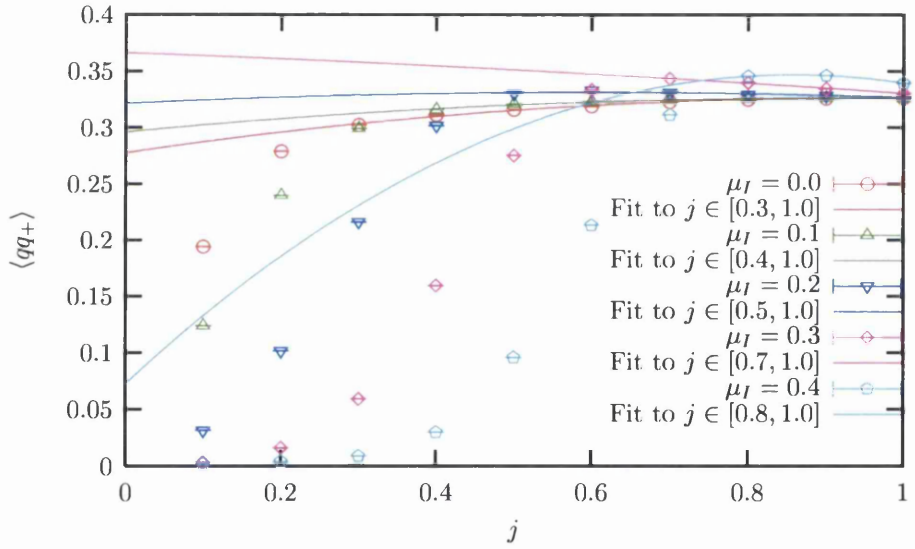

Figure 6.3: Arbitrary fits to the $\langle ud \rangle$ condensates plotted in Fig. 6.2.

value of the condensate remains approximately constant but increases slightly, and then decreases sharply at some large value. This seems to contradict the assumption on which these curves are based, i.e. that the gap is reduced as μ_I is increased, since one would expect $\langle ud \rangle$ to be proportional to the volume k-space within the gap, implying the gap increases slightly before the transition to a non-BCS phase.

At this point, whilst these simulations have presented some interesting results, it remains open both what our interpretation of them should be, and whether or not we should trust the quenched isospin approximation.

6.3 Non-zero Temperature

The standard measure of the stability of a superfluid (or superconducting) phase is the critical temperature T_c, i.e. the temperature at which the superfluid phase breaks down and the order parameter returns to zero. A simple example of this is illustrated in the superfluid phases of the two isotopes of Helium. In He^3, where superfluidity is reached via the pairing of atoms attracted by the subtle van-der-Waals force, $T_c \sim 2.4 \times 10^{-3}$K, whilst in He^4, where superfluidity occurs via the more fundamental Bose-Einstein condensation of the Helium atoms, $T_c \sim 2.12$K, almost a thousand times higher. An obvious avenue for further work in the investigation of the superfluid NJL model, therefore, is to measure T_c for the superfluid phase. In this final section, we shall discuss the prospects for simulations of our lattice model at non-zero temperature.

In standard lattice field theory calculations, the only measure of the temperature is the temporal extent of the Euclidean space-time lattice. To study a system at non-zero temperature, it is necessary to choose $L_t \times L_s^3$ lattices with

$$L_t \ll L_s. \tag{6.9}$$

If instead one were to choose some small $L_t \sim L_s$, one would effectively be studying a zero temperature system, since having $T^{-1} \neq 0$ in this system is equivalent to the finite volume effects. In a renormalisable field theory such as the $2+1d$ NJL model,

one may vary the temperature continuously by varying the bare inverse coupling β; this has the effect of changing the lattice spacing and, therefore, the temporal extent.

In a system of fermions with non-zero density, however, the spread of the Fermi-Dirac distribution, $\delta E \sim T$, serves as a second thermal scale. One cannot say the system is at zero temperature unless in addition to (6.9), one satisfies

$$(aL_t)^{-1} \ll \frac{2\pi}{aL_x}, \tag{6.10}$$

i.e. that the spread of the Fermi-Dirac distribution be smaller than the resolution of the lattice's momentum modes. It is for this reason that for parameters such as the diquark condensate, it was necessary to extrapolate to zero temperature, i.e. $L_t^{-1} \to 0$, even when $L_t \sim L_s$. This means that whilst for a full investigation of non-zero temperatures it is necessary to satisfy (6.9), re-analysis of the data presented herein at fixed L_t may provide some insight into the thermal effects of the system.

Performing new simulations with small L_t is also a relatively simple matter and the current code should run both quickly and efficiently. The fact that our model is an effective field theory, however, does complicate matters, since in such a theory one should not vary β to vary T continuously, as this has the additional effect of changing the cut-off. These simulations may be limited, therefore, to a small number of temperatures given by $L_t = 2n$ for $n = 2$, 3, etc. One possible way to overcome this would be to simulate several temperatures both in and out of the superfluid phase, and try to extrapolate data to T_c. This means that one could, in principle, use measurements of $\langle qq_+ \rangle$ and R to estimate the ratio between the gap and T_c for a fixed chemical potential, and compare it to the non-relativistic prediction of the BCS theory [26]

$$\frac{\Delta}{T_c} = 1.764. \tag{6.11}$$

Another way to circumvent the restriction placed by not being able to vary β, would be to redefine our theory on an anisotropic lattice, i.e. one with different lattice spacings, a_s and a_t in spatial and temporal directions. The physical (or correlation) anisotropy is defined by [44]

$$\xi = \frac{a_s}{a_t}. \tag{6.12}$$

One may then vary the temperature whilst keeping the physical cut-off fixed, either by varying ξ whilst keeping both a_s and L_t fixed, or by choosing ξ such that a_t is small enough to achieve a fine resolution in T and varying L_t. Not only would this allow an accurate measurement of T_c, but also the measurement of $\Delta(T)$, since in chapter 4 we concluded that $L_t = 16$ was the minimum number of temporal planes over which one could accurately fit the correlators (4.4) and (4.5). The introduction of an anisotropy, however, would require enough effort and care to make it a considerable undertaking. Such a study would only be worthwhile if the strategy of using the current code with $L_t \ll L_s$ should prove insufficient to estimate T_c.

Chapter 7

Summary

In this volume we have seen non-perturbative evidence for superfluidity in the $3+1$ dimensional Nambu–Jona-Lasinio model on the lattice at high chemical potential and low temperature. Measurement of a local order parameter for diquark condensation, via the use of noisy pseudo-fermion estimators, has shown that at $\mu = 1.0$, this parameter appears to be between $\frac{1}{2}$ and $\frac{2}{3}$ the value of the chiral order parameter in the vacuum. This was supported by a susceptibility ratio, $\lim_{j\to 0} R(\mu = 1.0) \approx 0$, which suggests a broken $\mathrm{U}(1)_B$ baryon number symmetry in the high-μ phase. By applying standard methods of lattice spectroscopy, we have also seen that when plotted in a suitable way, the dispersion relations of fermionic excitations show a clear discontinuity about the Fermi surface, directly analogous to the BCS gap Δ observed in traditional superconducting materials.

These features contrast sharply with the equivalent measurements in the $2+1$ dimensional NJL model [38], where fermionic dispersion relations were shown to pass smoothly through the Fermi surface, $\langle qq_+ \rangle$ to vanish as a power of j and R to be a constant independent of j. Together, these observations were treated as indicative of a critical phase with unbroken $\mathrm{U}(1)_B$ symmetry at high density.

The measurement of $\langle qq_+ \rangle$ was used to translate into an order-of-magnitude estimate for the gap Δ in [58] using the following simple-minded argument:[1] the condensate is the number density of bound diquark pairs, which in a BCS scenario is roughly equal to the volume of k-space within a shell of thickness 2Δ about the Fermi surface multiplied by the density of states; assuming the Fermi surface to be roughly spherical, this yields

$$\langle qq_+ \rangle \sim \Delta\mu^2. \tag{7.1}$$

At $\mu a = 0.8$, $\langle qq_+ \rangle a^3 \sim m^* a/2|_{\mu=0} \sim 0.2$, which implied that the size of the gap could well have been of $\mathcal{O}(100\text{MeV})$. The study of fermionic dispersion relations presented in chapter 4 showed Δ to be approximately constant over the measured range $0.5 \leq \mu \leq 0.8$, which in conjunction with the observation that for intermediate chemical potentials $\langle qq_+ \rangle \sim \mu^2$, means the assumptions leading to (7.1) are at least qualitatively correct. In the same chapter, it was shown that discretisation effects dominate the topology of the Fermi surface at high chemical potential, which ceases to increase as μ^2. This explains why, for $\mu > 0.8$ the slope of $\langle qq_+(\mu) \rangle$ decreases and eventually turns over, and (7.1) no longer holds.

For $\mu = 0.8$, which is the one non-zero chemical potential for which spectroscopic data were extrapolated in a controlled manner to zero temperature, the ratio $\Delta/(m^*|_{\mu=0})$ was found to be ~ 0.15. Assuming a fermion mass of 400MeV in the vacuum, this translates into a physical prediction $\Delta \approx 60\text{MeV}$, which although somewhat smaller than the naïve estimate above, is still consistent with the model predictions of [28].

[1] In [58] a different choice of parameters was used than in the work presented here, resulting in quantitatively different measurements for the order parameters. Hence, whilst the reasoning of this argument remains the same, the numbers used are slightly changed.

The one outstanding problem, which must yet prevent us from treating the evidence of superfluidity presented herein as absolute, is that all of our conclusions rely on the disregarding of data for which the diquark source j was less than 0.3. In chapter 5 an argument was presented that suggested these data disagreed with those at larger j because of finite volume effects, which are unusually large in this system [60]. In particular, we attribute this to the difficulty of representing the curved shell of states that partake in diquark condensation within $\delta E = \Delta$ of the Fermi surface on a discrete momentum lattice.

One piece of evidence that supports this hypothesis was presented in chapter 6, where the diquark condensate at zero temperature was plotted as a function of j with non-zero isospin chemical potential μ_I measured on field configurations with $\mu_I = 0.0$ and $\mu_B = 1.0$. For free fermions, the ground-state of a system with $\mu_B \gg \mu_I > 0$ is one in which the Fermi surfaces for "up" and "down" quarks are separated. For interacting fermions, however, if μ_I is small enough, the favoured state is one with standard BCS condensation between up and down quarks and one common Fermi surface as before [61]. Our results show that for small μ_I and large j, the value of the condensate is altered only slightly, whilst the value of j at which the condensate deviates from a quadratic is increased. It may be that in our system the effect of increasing μ_I is to reduce the size of the gap about k_F, which would accentuate any finite volume problems due to a coarse lattice of momentum-modes.

The most conclusive way of confirming that the low-j discrepancy is due to finite volume effects, however, must be to show that on some large lattice volume, for which the resolution in momentum space is increased, the discrepancy between data with j above and below 0.3 is reduced. In this vein, parallel simulations have been attempted

on very large lattices. Thusfar, it has proved hard even to reach an equilibrated configuration; on a 36^4 lattice with a molecular dynamic time-step of $\delta\tau = 0.005$ and trajectories of length only 0.5, the acceptance rate remains only $\approx 20\%$. This could be interpreted as a sign of encouragement, as the failure of the algorithm may be a signal that the partially quenched approximation is insufficient for such large volumes; if enough momentum modes were within the shell about the Fermi surface, diquark condensation may occur even with $j \equiv 0$ as partial quenching enforces during the field updates, and the algorithm may be attempting to represent a system with an exact Goldstone mode. A full simulation, with $j \neq 0$ during all steps of the algorithm, may yet be required to resolve this issue.

To summarise, our evidence for s-wave superfluidity via a BCS instability is of some importance, since this is the first time that the presence of such a phase has been demonstrated in a relativistic quantum field theory using a systematic calculational technique. Although the $3+1d$ NJL model is only a simplistic effective field theory, this work can be interpreted phenomenologically as non-perturbative evidence for BCS colour superconductivity in QCD with two degenerate flavours, since these two theories have the same global symmetry structure. This is of particular importance whilst the persistence of the sign problem prevents the numerical solution of full $SU(3)$ QCD. Also, the fact that our full solution agrees with the predictions of self-consistent treatments of this simple model also adds credence to such solutions of models with more complicated flavour structures and interactions.

In future work, one fairly simple calculation would be to measure the mass and/or decay rate of the pion non-perturbatively in our model, so that one could extract an estimate of the lattice spacing, and quote results in physical units as well as just

dimensionless ratios. It would be interesting to further the initial studies presented in chapter 6 to study the stability of the superfluid phase and measure $\langle qq_+ \rangle$ and R at non-zero temperature and to carry out further simulations with $\mu_I \neq 0$, in particular to see what effect this has on the size of the gap.

The most pressing issue, however, is to resolve the finite volume effects discussed above, since it is only when this has been addressed that the conclusions of chapters 3 and 4 may be completely trusted.

Appendix A

Staggered Fermions and their Interpretation

A.1 From Naïve to Staggered Fermions

In this appendix we discuss the nature of Fermion fields discretised using the Kogut-Susskind formalism. In the continuum, the Euclidean action for a free fermion field ψ is given by

$$S = \int \mathrm{d}^4 x \overline{\psi} \left(\not{\partial} + m_0 \right) \psi, \tag{A.1}$$

which when naïvely discretised becomes

$$S = a^4 \sum_x \left[\overline{\psi}_x \sum_\mu \left\{ \gamma_\mu \frac{(\psi_{x+\hat{\mu}} - \psi_{x-\hat{\mu}})}{2a} \right\} + m_0 \overline{\psi}_x \psi_x \right]. \tag{A.2}$$

If one Fourier transforms this to momentum space the action becomes

$$S = a^4 \int_{-\frac{\pi}{a}}^{\frac{\pi}{a}} \frac{\mathrm{d}^4 p}{(2\pi)^4} \overline{\psi} \left[\frac{i}{a} \sum_\mu \gamma_\mu \sin(a p_\mu) \psi + m_0 \psi \right]. \tag{A.3}$$

Taking the inverse of M, where $S = \int_p \overline{\psi} M \psi$, the propagator is found to be

$$S_F(p) = \frac{-\frac{i}{a} \sum_\nu \sin(a p_\nu) + m_0}{\sum_\mu \sin^2(a p_\mu) + (a m_0)^2}, \tag{A.4}$$

and the source of the infamous fermion doubling problem becomes clear. Although in the long wavelength limit, the small angle approximation implies $\sin ap \approx ap$ and one recovers the continuum Euclidean propagator, (A.4) also contains poles at the other 15 corners of the Brillouin zone, meaning that the naïve formulation represents 16 species of fermion.

In the staggered fermion formulation one can reduce the number of species by a factor of 4, which can then be interpreted as physical flavours [73]. Starting from (A.2) we can make the transformation

$$\psi_x \to \gamma_1^{x_1}\gamma_2^{x_2}\gamma_3^{x_3}\gamma_4^{x_4}\chi_x, \quad \overline{\psi}_x \to \overline{\chi}_x\gamma_4^{x_4}\gamma_3^{x_3}\gamma_2^{x_2}\gamma_1^{x_1}, \tag{A.5}$$

such that $\overline{\psi}_x\gamma_\mu\psi_{x\pm\hat{\mu}} \to \eta_\mu(x)\overline{\chi}_x\chi_{x\pm\hat{\mu}}$, where $\eta_\mu(x) = (-1)^{x_1+\ldots+x_{\mu-1}}$ and the action becomes

$$S = a^4\sum_x\left[\overline{\chi}_x\sum_\mu\left\{\eta_\mu(x)\frac{(\chi_{x+\hat{\mu}}-\chi_{x-\hat{\mu}})}{2a}\right\} + m_0\overline{\chi}_x\chi_x\right], \tag{A.6}$$

which is diagonal in γ_μ. One is then free to disregard all but one component in μ, after which the number of quark doublers is reduced to 4.

A.2 Flavours of Staggered Fermions

To interpret (A.6) in terms of the continuum fields ψ and $\overline{\psi}$ we recast the theory on the sites y of a lattice of hypercubic blocks with sites within the hypercube labelled $\eta_\mu = 0, 1$ such that $x_\mu = 2y_\mu + \eta_\mu$. The theory can then be rewritten in terms of fields $q_y^{\alpha a}$ and $\overline{q}_y^{a\alpha}$, which have definite Dirac spinor (α) and flavour (a) degrees of freedom associated with the 16-fold degeneracy in η. These fields are defined as

$$q_y^{\alpha a} \equiv \frac{1}{8}\sum_\eta \Gamma_\eta^{\alpha a}\chi_{2y+\eta}, \qquad \overline{q}_y^{a\alpha} \equiv \frac{1}{8}\sum_\eta \overline{\chi}_{2y+\eta}\Gamma_\eta^{\alpha a\dagger}, \tag{A.7}$$

where $\Gamma \equiv \gamma_1^{\eta_1}\gamma_2^{\eta_2}\gamma_3^{\eta_3}\gamma_4^{\eta_4}$. Using the the inverse of (A.7), and the relations

$$\gamma_\mu \Gamma_\eta = \delta_{0\eta_\mu}(-1)^{\eta_1+\ldots+\eta_{\mu-1}}\Gamma_{\eta+\hat{\mu}} + \delta_{1\eta_\mu}(-1)^{\eta_1+\ldots+\eta_{\mu-1}}\Gamma_{\eta-\hat{\mu}} \tag{A.8}$$

and

$$\gamma_5 \Gamma_\eta \gamma_5 = (-1)^{\eta_1+\eta_2+\eta_3+\eta_4}\Gamma_\eta, \tag{A.9}$$

one can show that the staggered quark action becomes

$$S = 16a^4 \sum_y \left\{ \frac{1}{a} \sum_{\mu=1}^{4} \overline{q}_y \left[(\gamma_\mu \otimes \mathbb{1}_4)\Delta_\mu - (\gamma_5 \otimes t_5 t_\mu)\delta_\mu \right] q_y + m_0 \overline{q}_y (\mathbb{1}_4 \otimes \mathbb{1}_4) q_y \right\}, \tag{A.10}$$

where $\Delta_\mu f_y = \frac{1}{4}(f_{y+\hat{\mu}} - f_{y-\hat{\mu}})$ and $\delta_\mu f_y = \frac{1}{4}(f_{y+\hat{\mu}} + f_{y-\hat{\mu}} - 2f_y)$ [74]. In (A.10) the first matrix in the tensor product acts on spinor and the second on flavour indices, with $t_\mu \equiv \gamma_\mu^{\text{tr}}$. In the continuum limit $\Delta_\mu \to a\partial_\mu$ and $\delta_\mu \to a^2\partial_\mu^2$ such that the second difference term vanishes and (A.10) tends to the continuum action for free fermions (A.1).

Appendix B

Computing Algorithms and Analysis

B.1 The Hybrid Monte-Carlo Algorithm

B.1.1 The Algorithm

In the Euclidean NJL model, the expectation value of an observable O as a function of the bosonic field configuration $[\Phi]$ is given by

$$\langle O \rangle \equiv \mathcal{Z}^{-1} \int \mathrm{D}\Phi O[\Phi] \det(M^\dagger M)[\Phi] e^{-S_{\mathrm{bos}}[\Phi]}, \tag{B.1}$$

where $\mathcal{Z}$ is the path integral (3.2). For a large non-trivial system, the only way to calculate such an integral is via a Monte Carlo method, in which a statistical sample $\{[\Phi_n]; n = 1, 2, \ldots, N\}$ is "picked" to approximate the full ensemble $\{\Phi\}$. Since for large volumes the Boltzmann weight $\det(M^\dagger M) e^{-S_{\mathrm{bos}}[\Phi]} \sim \int \mathrm{d}\chi \mathrm{d}\overline{\chi} e^{-S}$ is highly peaked about certain configurations, it is necessary to use importance sampling methods in which configurations are selected with a probability proportional to this weight.

The hybrid Monte Carlo algorithm (HMC), as its name suggests, is a combination of different parts of various long-established numerical algorithms. One starts with an

initial field configuration $[\Phi_n]$ and evaluates its Hamiltonian $H[\Phi_n]$. In analogy with the heat-bath algorithm [75], one then evolves the fields along a classical trajectory by the solution of Hamilton's equations

$$\dot{p_\sigma} = \frac{\partial S}{\partial \sigma}, \quad \dot{p_{\pi_i}} = \frac{\partial S}{\partial \pi_i} \; ; \tag{B.2}$$

$$\dot{\sigma} = -\frac{\partial S}{\partial p_\sigma}, \quad \dot{\pi_i} = -\frac{\partial S}{\partial p_{\pi_i}} \; , \tag{B.3}$$

where $\dot{p}$ is the derivative of a field's conjugate momentum p with respect to "simulation time" τ. These differential equations are solved via a numerical approximation such as the Euler method, with the initial values for p_σ and p_{π_i} sampled randomly from a Gaussian distribution. This initial random "kick", along with choosing the length of the trajectory from a similar Gaussian distribution, ensures ergodicity, i.e. that for any pair of configurations, the probability $P([\Phi_n] \rightarrow [\Phi_m]) > 0$ over the course of the simulation. The time-step in the numerical evaluation of Hamilton's equations is $\frac{\delta\tau}{2}$ and (B.2)/(B.3) are evaluated after an odd/even number of time-steps such that the fields and momenta are evaluated at $\tau = n\delta\tau$ and $\tau = \frac{(2n+1)}{2}\delta\tau$ respectively, where $n = 1, 2, \ldots$. This does mean that an extra half step must be made for the field momenta at the beginning of each trajectory.

Once a trajectory is complete, its end point is labelled as the trial configuration $[\Phi_{(n+1)_t}]$. The Hamiltonian $H[\Phi_{(n+1)_t}]$ is evaluated and $[\Phi_{(n+1)_t}]$ is accepted with probability

$$P(\Phi_n \rightarrow \Phi_{(n+1)_t}) = \min\left[1, \frac{\det(M^\dagger M)[\Phi_{(n+1)_t}]}{\det(M^\dagger M)[\Phi_n]} e^{-\left(H[\Phi_{(n+1)_t}] - H[\Phi_n]\right)}\right], \tag{B.4}$$

which is the direct equivalent of the accept/reject step in the Metropolis algorithm [76]. If the result is an acceptance, the next link in the Markov chain is $[\Phi_{n+1}] = [\Phi_{(n+1)_t}]$. If not, then the configuration prior to the trajectory is kept such that $[\Phi_{n+1}] = [\Phi_n]$.

One then samples new random field momenta p_σ and p_{π_i} and begins to generate the next trajectory. A schematic of the algorithm is illustrated in Fig. B.1.

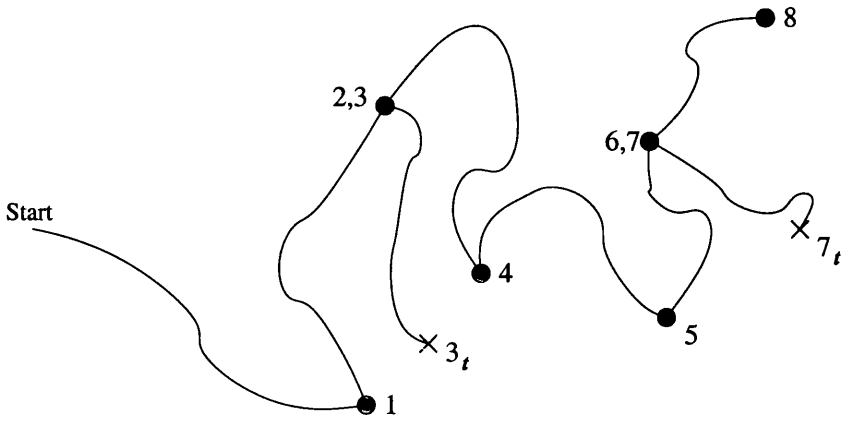

Figure B.1: Schematic of 8 trajectories in the HMC algorithm. Green circles and red crosses represent the end of accepted and rejected trajectories respectively. The trial configurations of both the 3rd and 7th trajectories have been rejected and the initial configurations used.

Similarly to the Metropolis algorithm, it is in the accept/reject step that the evaluation of the integral in (B.1) occurs. Obedience of this Metropolis rule ensures that the algorithm satisfies detailed balance in thermal equilibrium, i.e. that

$$W_m P([\Phi_m] \to [\Phi_n]) = W_n P([\Phi_n] \to [\Phi_m]), \tag{B.5}$$

where W_m is the Boltzmann weight $\det(M^\dagger M)[\Phi_m]e^{-S_{\rm bos}[\Phi_m]}$. The only effect the $\mathcal{O}(\delta\tau)$ errors in the solution of (B.2) and (B.3) have is to reduce the acceptance rate; it is in this sense that HMC is said to be exact.

B.1.2 The Sign of the Determinant

For the HMC algorithm to work it is necessary that $\det(M^\dagger M)$ is both real and positive. Furthermore, it is shown in section 3.1, that there is an operator T that

satisfies both $[KT, M] = 0$ and $(KT)^2 = -1$, where K is the complex conjugation operator, which in turn implies that $\det M$ itself must be both real and positive. The proof of this argument, outlined in [33], is presented here for completeness.

If ψ is an eigenvector of M with the eigenvalue λ,

$$M\psi = \lambda\psi \Rightarrow KTM\psi = KT\lambda\psi \Rightarrow KTM\psi = \lambda^* KT\psi. \tag{B.6}$$

If $[KT, M] = 0$,

$$M\psi' \equiv MKT\psi = KTM\psi = \lambda^* KT\psi = \lambda^*\psi', \tag{B.7}$$

which implies that the eigenvalues of M come in complex conjugate pairs. Since M is diagonalisable, its determinant can be written as the product over its eigenvalues which must, therefore, be real.

The second point is more subtle. Although the product over eigenvalues is real, if ψ and ψ' were proportionate there could exist real and non-degenerate eigenvalues, an odd number of which could be negative. If $(KT)^2 = -1$, however,

$$\langle\psi|\psi'\rangle = \langle\psi|KT\psi\rangle = \langle T\psi|TKT\psi\rangle\,. \tag{B.8}$$

The right hand side can be re-written using the fact that $\langle K\psi_1|K\psi_2\rangle = \langle\psi_1|\psi_2\rangle^* = \langle\psi_2|\psi_1\rangle$ to give

$$\langle\psi|\psi'\rangle = \left\langle (KT)^2\psi|KT\psi\right\rangle = -\langle\psi|\psi'\rangle = 0. \tag{B.9}$$

So if $(KT)^2 = -1$, ψ and ψ' must be linearly independent and $\det M$ must be positive.

B.1.3 Matrix Inversion: The Conjugate Gradient Method

In our implementation of the HMC algorithm, the inverse of M needed to evaluate (B.2), (B.3) and (B.4), was calculated using a (bi)conjugate gradient routine based

on that from §2.7 of Numerical Recipes [53]. This method has the distinct advantage that it is not necessary to store all of M; one need only know how to act M and $M^\dagger$ on a column vector. Here we describe the algorithm as it was used.

The algorithm solves the linear system

$$M^\dagger M\xi = \Phi, \tag{B.10}$$

for $\xi = (M^\dagger M)^{-1}\Phi$, where Φ is the pseudo-fermion field. One first initialises the vectors $\vec{r}_1 = \Phi$ and $\vec{p}_1 = \xi_1$, where the initial guess solution ξ_1 is also chosen as Φ. One then carries out the following recurrence:

$$\begin{aligned}
\alpha_k &= \frac{\vec{r^\dagger}_k \vec{r}_k}{\vec{p^\dagger}_k M^\dagger M \vec{p}_k}; \\
\vec{r}_{k+1} &= \vec{r}_k - \alpha_k M^\dagger M \vec{p}_k; \\
\vec{r^\dagger}_{k+1} &= \vec{r^\dagger}_k - \alpha_k M^\dagger M \vec{p^\dagger}_k; \\
\beta_k &= \frac{\vec{r^\dagger}_{k+1} \vec{r}_{k+1}}{\vec{r^\dagger}_k \vec{r}_k}; \\
\vec{p}_{k+1} &= \vec{r}_k + \beta_k \vec{p}_k; \\
\vec{p^\dagger}_{k+1} &= \vec{r^\dagger}_k + \beta_k \vec{p^\dagger}_k,
\end{aligned} \tag{B.11}$$

leading to the sequence of improved estimates

$$\xi_{k+1} = \xi_k + \alpha_k p_k, \tag{B.12}$$

chosen to stop when the residual $r_k \equiv \Phi - (M^\dagger M)\xi$ is less than the stopping residual $2Vr_s^2$, where r_s^2 is the stopping residual per element.

In the measurement subroutines, the same algorithm was used to solve $\mathcal{A}^\dagger \mathcal{A}\xi = \mathcal{A}^\dagger \eta$ for ξ. Because the dimension of the matrix is twice that of $M^\dagger M$, the stopping residual was $4Vr_s^2$.

B.2 Error Analysis

B.2.1 Errors in uncorrelated data

From any initial configuration, a series of HMC iterations are guarantied take one into the canonical ensemble $\{\Phi_c\}$, i.e. the ensemble in which equilibrium is reached. The post-equilibration Markov chain of configurations $\{[\Phi_i]; i = 1, 2, \ldots, N\}$ generated by the algorithm, however, is only a sample of $\{\Phi_c\}$ and the statistical average of an observable $\langle O \rangle$ measured over $\{[\Phi_i]\}$ can only be identified with its average over the ensemble $\overline{\langle O \rangle}$ in the limit $N \dashrightarrow \infty$. When calculating $\langle O \rangle$, one must also calculate its statistical uncertainty, therefore, so that one can know how well the estimate represents the true value $\overline{\langle O \rangle}$.

In the ideal case, in which all configurations are statistically independent, $\langle O \rangle$ is given by the arithmetic mean

$$\langle O \rangle = \frac{1}{N} \sum_{i=1}^{N} O[\Phi_i], \tag{B.13}$$

and its error with respect to $\langle \bar{O} \rangle$ is given by the standard error

$$\delta \langle O \rangle = \sqrt{\frac{1}{N(N-1)} \sum_{i=1}^{N} (O[\Phi_i] - \langle O \rangle)^2}. \tag{B.14}$$

B.2.2 Binning and Jackknife Analysis

The standard error is only a good estimate of the statistical uncertainty when all configurations are statistically independent. When the configurations are generated with the HMC algorithm, however, this clearly is not the case, since successive configurations are either generated through travel along trajectory of finite length through phase space, or are completely identical. The data set is said to suffer from autocorrelations. Fig. B.2 shows the time history of an observable measured in a typical

simulation in which autocorrelations can be seen. The observable is $V\left\langle qq_{+}^{2}\right\rangle$ measured on a $20 \times 96 \times 12^2$ lattice at $\mu = 0.8$.

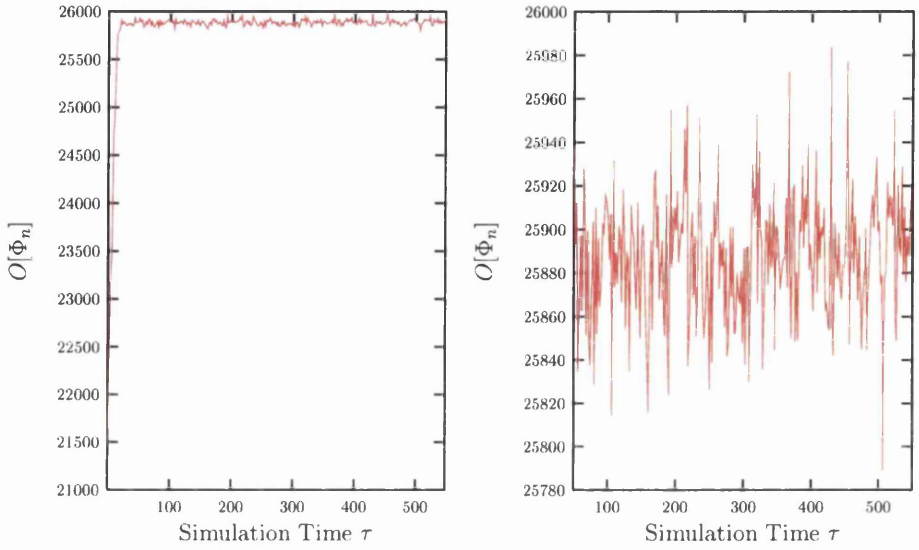

Figure B.2: A typical simulation time history of an observable measured on every other configuration. An equilibration time of ~ 50 time steps is observed in the left hand figure. Discarding this data, autocorrelations are clearly visible.

Autocorrelation in data means that the standard error given by (B.14) significantly underestimates the statistical uncertainty in the mean. The simplest way to overcome this is to generate a large number of configurations and only carry out measurement on widely separated, statistically independent configurations.

It is often more convenient, however, to estimate the true error in the correlated data. One method of doing this is by separating the N data into N_{bins} bins of size $s_{\text{bin}} = N/N_{\text{bins}}$, and calculating the binned estimators as the average of the observable in each bin

$$O_{i_{\text{bin}}} = \frac{1}{s_{\text{bin}}} \sum_{i=1}^{s_{\text{bin}}} O_i. \tag{B.15}$$

If one then treats these estimators as independent data, their mean

$$\langle O_{i_{\rm bin}} \rangle = \frac{1}{N_{\rm bins}} \sum_{i_{\rm bin}=1}^{s_{\rm bin}} O_{i_{\rm bin}} = \frac{1}{N} \sum_{i=1}^{N} O_i, \tag{B.16}$$

is seen to be identical to the mean of the original data set.[1]. The advantage of binning, however, is that when one calculates the standard error in $\langle O_{i_{\rm bin}} \rangle$,

$$\delta \langle O_{i_{\rm bin}} \rangle = \sqrt{\frac{1}{N_{\rm bins}(N_{\rm bins}-1)} \sum_{i_{\rm bin}=1}^{N_{\rm bins}} (O_{i_{\rm bin}} - \langle O_{i_{\rm bin}} \rangle)^2}, \tag{B.17}$$

this is equivalent to the error in data separated by $s_{\rm bin}$. Increasing the bin size increases the estimate in the error until $s_{\rm bin}$ is greater than the autocorrelation length. The magnitude of the error should then be roughly independent of the bin size and represents the true statistical error in $\langle O \rangle$ [44]. An example of this is illustrated in Fig. B.3. The data come from a simulation of 1000 trajectories on an 8^4 lattice at $\mu = 0.0$.

A slightly more sophisticated way of estimating the error in $\langle O \rangle$ is the jackknife method. This is similar to the standard binning procedure except that in the equivalent of (B.15), the jackknife estimators are given by the average of the entire data set excluding the related bin, i.e.

$$O_{i_{\rm jack}} = \frac{1}{N - s_{\rm bin}} \sum_{i \notin i_{\rm bin}} O_i. \tag{B.18}$$

This is the origin of the term jackknife, since it is as if the bin has been cut out of the data set. The mean of the estimators is

$$\langle O_{i_{\rm jack}} \rangle = \frac{1}{N_{\rm bins}} \sum_{i_{\rm jack}=1}^{N_{\rm bins}} O_{i_{\rm jack}} \tag{B.19}$$

[1]This is only strictly true if the number of data N is divisible by the number of bins $N_{\rm bins}$ If this is not the case then the size of the data set should be rounded down and N in (B.16) and following formulae should be replaced by $N - (N \mod s_{\rm bin})$.

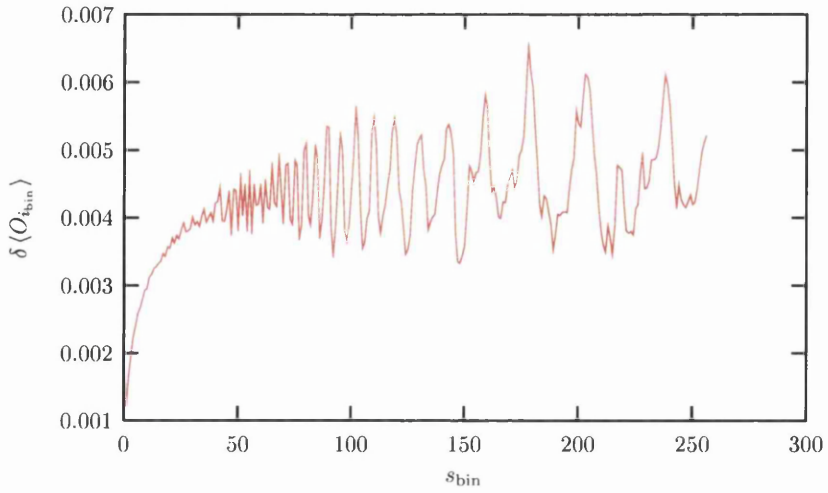

Figure B.3: Error in binned $\langle\overline{\chi}\chi\rangle$ data from a typical simulation as a function of bin size $s_{\rm bin}$. For $s_{\rm bin} > 50$ the magnitude of the error is approximately constant.

and the standard error is given by

$$\delta\left\langle O_{i_{\rm jack}}\right\rangle = \sqrt{\frac{1}{N_{\rm bins}(N_{\rm bins}-1)}\sum_{i_{\rm jack}=1}^{N_{\rm bins}}\left(O_{i_{\rm jack}} - \left\langle O_{i_{\rm jack}}\right\rangle\right)^2}. \tag{B.20}$$

For primary quantities such as $\langle\overline{\chi}\chi\rangle$ this is the equivalent of using standard binning estimators. For secondary quantities however, such as the susceptibility of $\langle\overline{\chi}\chi\rangle$ the jackknife estimate of the error is usually more reliable [44, 77].

B.3 Least Squares Curve Fitting

The modelling of a data set $y_i(x_i)$ by a general curve $y(x) = f(x, a_1, a_2, \ldots, a_m)$ with m free parameters can be carried out by means of maximum likelihood estimation. This is done by identifying the probability of the data set being measured given the parameters, with the likelihood of the parameters being right given the data set. If we assume that each datum $y_i(x_i)$ is picked from a Gaussian distribution about the

"true" model curve $f(x)$ with a standard deviation σ_i, the probability of the data having been measured is

$$P \sim \prod_{i=1}^{N} \exp\left[-\frac{1}{2}\left(\frac{y_i - f(x_i)}{\sigma_i}\right)\right], \tag{B.21}$$

where N is the size of the data set. Finding the maximum of this probability is the equivalent of finding the minimum of the χ^2 value

$$\chi^2 \equiv \sum_{i=1}^{N}\left[\frac{y_i - f(x_i, a_1, a_2, \ldots, a_m)}{\sigma_i}\right]^2. \tag{B.22}$$

Although our data sets are drawn from a Poisson distribution and not a Gaussian, these two distributions are equivalent in the limit that the number of data $N \to \infty$. The problem of fitting the data is therefore reduced to the problem of minimising (B.22) with respect to the parameters a_i.

Fits of data to functions that are linear in a_i, i.e. that take the form $f(x) = a_1 f_1(x) + a_2 f_2(x) + \ldots + a_m f_m(x)$ can be described in the following way. First one defines an $N \times m$ matrix called the design matrix $\mathbf{A}$ with entries $A_{ij} = \frac{f_j(x_i)}{\sigma_i}$ and a vector $\mathbf{b}$ of length N and with elements $b_i = \frac{y_i}{\sigma_i}$. The minimisation of χ^2 is then equivalent to finding the vector $\mathbf{a}$, which contains the values of a_i, that minimises

$$\chi^2 = |\mathbf{A}.\mathbf{a} - \mathbf{b}|^2. \tag{B.23}$$

We choose to solve this via singular value decomposition using the Numerical Recipes subroutine `svdfit` and its dependent subroutines [53]. Calling this routine once, one is returned the solution vector $\mathbf{a}$, the errors $\sigma(a_i)$ as the square root of the diagonal elements of an array $\mathrm{Cov}(a_i, a_j)$ and the value of χ^2. In general, a fit can be said to be good if the value of χ^2 is less than or similar to the number of degrees of freedom, in this case given by $N - m$.

Functions that are not linear in a_i clearly cannot be fitted by this method. Instead one must choose an iterative method, starting with trial values of a_i and carrying out operations that decrease χ^2 until it reaches a minimum. We choose the Levenberg-Marquardt method using the Numerical Recipes subroutine `mrqmin` and its dependent subroutines [53]. One must supply the function to be fitted and its derivative with respect to each a_i. After one call to the routine, $\mathbf{a}$, $\sigma(a_i)$, and χ^2 are returned as before.

Appendix C

Shared-memory Parallel Programming

In the finite volume study presented in chapter 5, some simulations were carried out on lattices with $L_t = 36$ and $L_t = 48$, each on one node ($\sim$ 100 CPUs) of the Sun Galaxy-class supercomputer at the Cambridge-Cranfield High Performance Computing Facility (HPCF). Parts of the code were explicitly parallelised using OpenMP (OMP), a set of compiler directives, library routines and environment variables used to specify shared memory parallelism. This appendix contains a discussion on the choice of which routines were to be explicitly parallelised as well as a brief list of some basic OMP directives and how to implement them.

The Fortran compiler on the Sun machine contains an option to auto-parallelise code. When this was tried for the NJL code, however, it was found to be very inefficient, with little benefit found from running in parallel. It was decided, therefore, that the most CPU intensive parts should be parallelised explicitly. Fig. C.1 shows a breakdown of the exclusive CPU time spent in various parts of the code, i.e. the amount of time the program spends in a subroutine excluding time spent executing calls to functions or subroutines within it. It is clear that the majority of time is spent

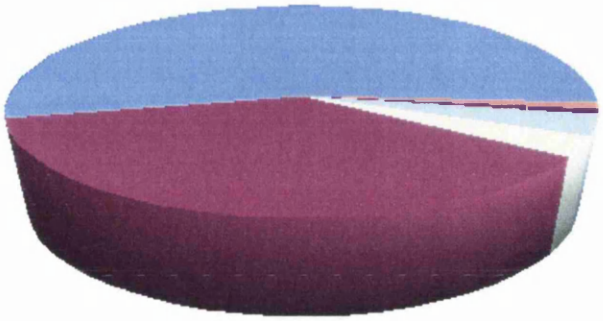

Subroutine	t (%)
Conjugate Gradient (Nambu-Gor'kov)	54.3
Conjugate Gradient (Normal)	37.6
Measurement	3.2
Force Terms	3.1
Main	0.8
Others	1.0

Figure C.1: Pie chart illustrating the percentage of exclusive CPU time spent in various subroutines in a serial run on one processor.

in the fairly simple conjugate gradient routines, so these were chosen to be explicitly parallelised.

The main advantage of OMP over message-passing standards such as MPI is in its simplicity to implement. It is based on the shared memory model, in which all processors have access to the same global memory, but have their own copy of local data, such as the loop counter in a parallelised loop. This means that data transfer is transparent from a programmer's point of view, so long as each variable is declared to be either global or local. The implementation is done by adding directives to the code that begin with the phrase `!$OMP`, and are therefore treated as a comment by a standard Fortran compiler.

A parallel region can be set up in several ways. The simplest way to make a loop run in parallel is by using `!$OMP parallel do`, e.g.

```
!$OMP parallel do
    do i=1,n
        a(i)=b(i)+c(i)
    enddo
!$OMP end parallel do
```

This is called a work-sharing construct, since the work done in the loop is shared between a number of CPUs, or threads. By default, variables are global and shared between all processors except for those used as loop counters, which are private and each processor owns their own copy. However, the above code could have been written as

```
!$OMP parallel do shared(a,b,c,n) private(i,temp)
    do i=1,n
        temp=b(i)+c(i)
        a(i)=temp
    enddo
!$OMP end parallel do     ,
```

which shows the importance in declaring variables explicitly, since by default `temp` would be a global variable, meaning that the values of `a(i)` would be assigned wrong and unpredictable values. One way to stop code becoming cluttered is to declare a default data type. The first line above could then be written as

```
!$OMP parallel do default(shared) private(i,temp)      .
```

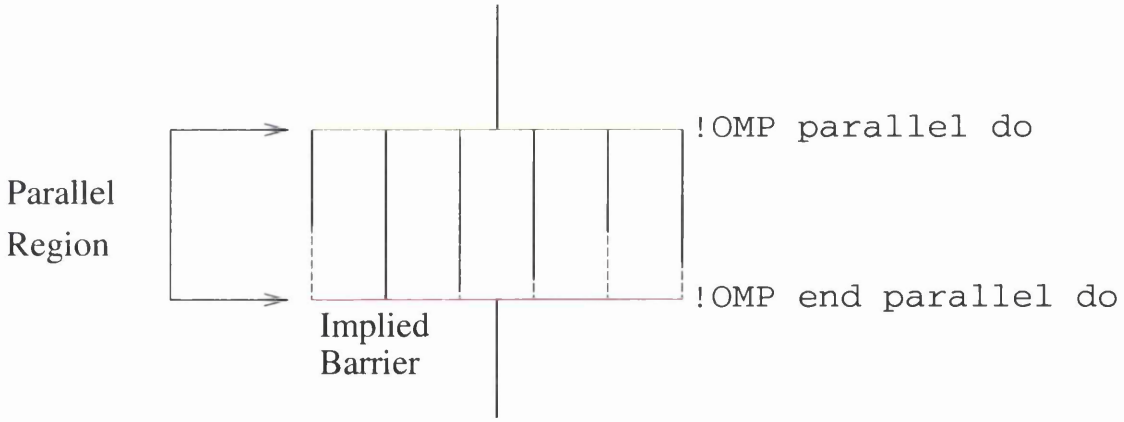

Figure C.2: The fork and join model of shared memory programming. In this example, within the parallel region the number of threads is increased from 1 to 6.

Although running sections of the code in parallel decreases the wall clock time it

takes to run, there are several overheads involved. The first of these is due to copying global data from one CPU to another. With OMP one has little control over this. The other main overhead is that at most times, some processors are idle. Not only does this happen when one is outside the parallel region, but also at the end of a parallel region where a barrier is implied, i.e. where all threads must wait for the slowest to finish. This is illustrated diagrammatically in Fig. C.2.

One way to reduce this is to define large parallel regions with multiple do loops inside. The `nowait` directive can then be used to direct each thread to carry on and start their part of the next parallel loop and the number of barriers is reduced. This can only be done if the input of the second loop does not depend in a non-trivial way on the output of the first. An example of this would be

```
!$OMP parallel default(shared)
!$OMP do private(i,temp)
    do i=1,n
        temp=b(i)+c(i)
        a(i)=temp
    enddo
!$OMP end do nowait
!$OMP do private(i,temp)
    do i=1,n
        temp=e(i)+f(i)
        d(i)=temp
    enddo
!$OMP end do
!$OMP end parallel
```

Another important concept is that of reduction variables. These are scalar variables used in collective operations over elements of an array, such as a sum or a product. The reduction variable is treated as a local variable within the parallel region, the sum or product of which are reduced into a single global variable at the end

of the region. An example of this is

```
sum=0.
prd=1.
!$OMP parallel default(shared)
!$OMP do private(i,temp) reduction(+:sum) reduction(*:prd)
    do i=1,n
        sum=sum+a(i)
        prd=prd*a(i)
    enddo
!$OMP end do
!$OMP end parallel    .
```

This list of directives, which includes all of those used in parallelising the conjugate gradient routines, is by no means comprehensive. There are many issues, such as explicitly scheduling the sharing of work between threads or changing the number of threads between one parallel region and another that have been ignored here since in our implementation the default values were used. For more information see e.g. [78].

Once the conjugate gradient routines were parallelised, some short test runs showed that when run on 48 CPUs, the speedup (i.e. the ratio between the wall clock times of the serial and parallel code) was found to be ~ 15 for the inversion of M and ~ 25 for the inversion of $\mathcal{A}$. The rest of the code was parallelised using the compiler's auto-paralleliser.

Bibliography

[1] M. Gell-Mann, *A schematic model of baryons and mesons*, Phys. Lett. **8** (1964), 214–215.

[2] V.E. Barnes et al., *Observation of a hyperon with strangeness −3*, Phys. Rev. Lett. **12** (1964), 204–206.

[3] G. Miller et al., *Inelastic electron - proton scattering at large momentum transfers*, Phys. Rev. **D5** (1972), 528.

[4] H. Fritzsch, M. Gell-Mann, and H. Leutwyler, *Advantages of the color octet gluon picture*, Phys. Lett. **B47** (1973), 365–368.

[5] G. 't Hooft, *Computation of the quantum effects due to a four-dimensional pseudoparticle*, Phys. Rev. **D14** (1976), 3432–3450.

[6] G. 't Hooft, *Symmetry breaking through Bell-Jackiw anomalies*, Phys. Rev. Lett. **37** (1976), 8–11.

[7] D.J. Gross and F. Wilczek, *Ultraviolet behavior of non-abelian gauge theories*, Phys. Rev. Lett. **30** (1973), 1343–1346.

[8] H.D. Politzer, *Reliable perturbative results for strong interactions?*, Phys. Rev. Lett. **30** (1973), 1346–1349.

[9] K.G. Wilson, *Confinement of quarks*, Phys. Rev. **D10** (1974), 2445–2459.

[10] F. Wilczek, *Opportunities, challenges, and fantasies in lattice QCD*, Nucl. Phys. Proc. Suppl. **119** (2003), 3–12.

[11] J.V. Narlikar, *Introduction to cosmology*, Cambridge University Press, 1983.

[12] N.K. Glendenning, *Compact stars: Nuclear physics, particle physics, and general relativity*, Astronomy and Astrophysics Library, Springer-Verlag New York, 1996.

[13] S.J. Hands, *The phase diagram of QCD*, Contemp. Phys. **42** (2001), 209–225.

[14] M.G. Alford, *QCD at high density / temperature*, Nucl. Phys. Proc. Suppl. **117** (2003), 65–82.

[15] P. Duinker, *Review of electron - positron physics at PETRA*, Rev. Mod. Phys. **54** (1982), 325.

[16] J.I. Kapusta, *Finite-temperature field theory*, Cambridge monographs on mathematical physics, Cambridge University Press, 1989.

[17] S. Ejiri, *Lattice QCD at finite temperature*, Nucl. Phys. Proc. Suppl. **94** (2001), 19–26.

[18] E. Laermann and O. Philipsen, *Status of lattice QCD at finite temperature*, `arXiv:hep-ph/0303042` (2003).

[19] K. Kanaya, *Recent lattice results relevant for heavy ion collisions*, Nucl. Phys. **A715** (2003), 233–242.

[20] Z. Fodor, *Lattice QCD results at finite temperature and density*, Nucl. Phys. **A715** (2003), 319–328.

[21] L.P. Csernai and J.I. Kapusta, *Entropy and cluster production in nuclear collisions*, Phys. Rept. **131** (1986), 223–318.

[22] Z. Fodor and S.D. Katz, *Lattice determination of the critical point of QCD at finite T and μ*, JHEP **03** (2002), 014.

[23] C.R. Allton, S. Ejiri, S.J. Hands, O. Kaczmarek, F. Karsch, E. Laermann, C. Schmidt, and L. Scorzato, *The QCD thermal phase transition in the presence of a small chemical potential*, Phys. Rev. **D66** (2002), 074507.

[24] P. de Forcrand and O. Philipsen, *The QCD phase diagram for small densities from imaginary chemical potential*, Nucl. Phys. **B642** (2002), 290–306.

[25] J. Bardeen, L.N. Cooper, and J.R. Schrieffer, *Microscopic theory of superconductivity*, Phys. Rev. **106** (1957), 162.

[26] J. Bardeen, L.N. Cooper, and J.R. Schrieffer, *Theory of superconductivity*, Phys. Rev. **108** (1957), 1175–1204.

[27] M.G. Alford, K. Rajagopal, and F. Wilczek, *QCD at finite baryon density: Nucleon droplets and color superconductivity*, Phys. Lett. **B422** (1998), 247–256.

[28] K. Rajagopal and F. Wilczek, *The condensed matter physics of QCD*, in: M. Shifman (Ed.), *Handbook of QCD*, World Scientific, ch.35, 2001.

[29] J. Berges and K. Rajagopal, *Color superconductivity and chiral symmetry restoration at nonzero baryon density and temperature*, Nucl. Phys. **B538** (1999), 215–232.

[30] A. Burrows and J.M. Lattimer, *The birth of neutron stars*, Astrophys. J. **307** (1986), 178–196.

[31] M.G. Alford, K. Rajagopal, and F. Wilczek, *Color-flavor locking and chiral symmetry breaking in high density QCD*, Nucl. Phys. **B537** (1999), 443–458.

[32] F. Neumann, M. Buballa, and M. Oertel, *Mixed phases of color superconducting quark matter*, Nucl. Phys. **A714** (2003), 481–501.

[33] S.J. Hands, I. Montvay, L. Scorzato, and J. Skullerud, *Diquark condensation in dense adjoint matter*, Eur. Phys. J. **C22** (2001), 451–461.

[34] J.B. Kogut, D.K. Sinclair, S.J. Hands, and S.E. Morrison, *Two-colour QCD at non-zero quark-number density*, Phys. Rev. **D64** (2001), 094505.

[35] Y. Nambu and G. Jona-Lasinio, *Dynamical model of elementary particles based on an analogy with superconductivity. I*, Phys. Rev. **122** (1961), 345–358.

[36] Y. Nambu and G. Jona-Lasinio, *Dynamical model of elementary particles based on an analogy with superconductivity. II*, Phys. Rev. **124** (1961), 246–254.

[37] C.G. Strouthos and D.N. Walters, *Mass generation without phase coherence at nonzero temperature*, Phys. Rev. **D67** (2003), 034505.

[38] S.J. Hands, B. Lucini, and S. Morrison, *Numerical portrait of a relativistic thin film BCS superfluid*, Phys. Rev. **D65** (2002), 036004.

[39] R. Aloisio, V. Azcoiti, G. Di Carlo, A. Galante, and A.F. Grillo, *Probability distribution function of the diquark condensate in two colours QCD*, Nucl. Phys. **B606** (2001), 322–336.

[40] S.J. Hands and J.B. Kogut, *Logarithmic corrections to the equation of state in the SU(2)⊗SU(2) Nambu–Jona-Lasinio model*, Nucl. Phys. **B520** (1998), 382–408.

[41] S.P. Klevansky, *The Nambu–Jona-Lasinio model of quantum chromodynamics*, Rev. Mod. Phys. **64** (1992), 649–708.

[42] B. Rosenstein, B. Warr, and S.H. Park, *Dynamical symmetry breaking in four Fermi interaction models*, Phys. Rept. **205** (1991), 59–108.

[43] S.J. Hands, A. Kocić, and J.B. Kogut, *Four Fermi theories in fewer than four-dimensions*, Ann. Phys. **224** (1993), 29–89.

[44] I. Montvay and G. Munster, *Quantum fields on a lattice*, Cambridge monographs on mathematical physics, Cambridge University Press, 1994.

[45] P. Hasenfratz and F. Karsch, *Chemical potential on the lattice*, Phys. Lett. **B125** (1983), 308.

[46] S.J. Hands and S.E. Morrison, *Lattice simulation of diquark condensation in dense matter*, Phys. Rev. **D59** (1999), 116002.

[47] L.H. Karsten and J. Smit, *Lattice fermions: Species doubling, chiral invariance, and the triangle anomaly*, Nucl. Phys. **B183** (1981), 103.

[48] T. Hatsuda and T. Kunihiro, *Fluctuation effects in hot quark matter: Precursors of chiral transition at finite temperature*, Phys. Rev. Lett. **55** (1985), 158–161.

[49] T. Hatsuda and T. Kunihiro, *Character changes of pion and sigma meson at finite temperature*, Phys. Lett. **B185** (1987), 304.

[50] S. Duane, A.D. Kennedy, B.J. Pendleton, and D. Roweth, *Hybrid Monte Carlo*, Phys. Lett. **B195** (1987), 216–222.

[51] S. Gottlieb, W. Liu, D. Toussaint, R.L. Renken, and R.L. Sugar, *Chiral symmetry breaking in lattice QCD with two and four fermion flavors*, Phys. Rev. **D35** (1987), 3972–3980.

[52] I. Barbour, S. Hands, J.B. Kogut, M. Lombardo, and S. Morrison, *Chiral symmetry restoration and realisation of the Goldstone mechanism in the U(1) Gross-Neveu model at non-zero chemical potential*, Nucl. Phys. **B557** (1999), 327–351.

[53] W.H. Press, S.A. Teukolsky, W.T. Vetterling, and B.P. Flannery, *Numerical recipes in FORTRAN*, Cambridge University Press, 1986.

[54] S. Elitzur, *Impossibility of spontaneously breaking local symmetries*, Phys. Rev. **D12** (1975), 3978–3982.

[55] G. Boyd, F. Karsch, and S. Gupta, *The quark propagator at finite temperature*, Nucl. Phys. **B385** (1992), 481–501.

[56] S.J. Hands, J.B. Kogut, C.G. Strouthos, and T.N. Tran, *Fermi surface phenomena in the (2+1)d four-Fermi model*, Phys. Rev. **D68** (2003), 016005.

[57] C. Kittel, *Introduction to solid state physics*, seventh ed., John Wiley & Sons, 1996.

[58] S.J. Hands and D.N. Walters, *Evidence for BCS diquark condensation in the 3+1d lattice NJL model*, Phys. Lett. **B548** (2002), 196–203.

[59] P. Hasenfratz and H. Leutwyler, *Goldstone boson related finite size effects in field theory and critical phenomena with O(N) symmetry*, Nucl. Phys. **B343** (1990), 241–284.

[60] P. Amore, M.C. Birse, J.A. McGovern, and N.R. Walet, *Colour superconductivity in finite systems*, Phys. Rev. **D65** (2002), 074005.

[61] M.G. Alford, J.A. Bowers, and K. Rajagopal, *Crystalline color superconductivity*, Phys. Rev. **D63** (2001), 074016.

[62] M.G. Alford, J. Berges, and K. Rajagopal, *Magnetic fields within color superconducting neutron star cores*, Nucl. Phys. **B571** (2000), 269–284.

[63] A.M. Clogsten, *Upper limit for the critical field in hard superconductors*, Phys. Rev. Lett. **9** (1962), 266–267.

[64] B.S. Chandrasekhar, *A note on the maximum critical field of high field superconductors*, App. Phys. Lett. **1** (1962), 7.

[65] P.F. Bedaque, *Color superconductivity in asymmetric matter*, Nucl. Phys. **A697** (2002), 569–577.

[66] A.I. Larkin and Y.A. Ovchinnikiv, Zh. Eksp. Teor. Fiz. **47** (1964), 1136.

[67] P. Fulde and R.A. Ferrel, *Superconductivity in a strong spin-exchange field*, Phys. Rev. **135** (1964), A550–A563.

[68] D. Toublan and J.B. Kogut, *Isospin chemical potential and the QCD phase diagram at nonzero temperature and baryon chemical potential*, Phys. Lett. **B564** (2003), 212–216.

[69] M. Frank, M. Buballa, and M. Oertel, *Flavor-mixing effects on the QCD phase diagram at non-vanishing isospin chemical potential: One or two phase transitions?*, Phys. Lett. **B562** (2003), 221–226.

[70] D.T. Son and M.A. Stephanov, *QCD at finite isospin density*, Phys. Rev. Lett. **86** (2001), 592–595.

[71] J.B. Kogut and D.K. Sinclair, *Lattice QCD at finite isospin density at zero and finite temperature*, Phys. Rev. **D66** (2002), 034505.

[72] K. Splittorff, D.T. Son, and M.A. Stephanov, *QCD-like theories at finite baryon and isospin density*, Phys. Rev. **D64** (2001), 016003.

[73] J.B. Kogut and L. Susskind, *Hamiltonian formulation of Wilson's lattice gauge theories*, Phys. Rev. **D11** (1975), 395.

[74] H. Kluberg-Stern, A. Morel, O. Napoly, and B. Petersson, *Flavors of Lagrangian Susskind fermions*, Nucl. Phys. **B220** (1983), 447.

[75] M. Creutz, *Monte Carlo study of quantized SU(2) gauge theory*, Phys. Rev. **D21** (1980), 2308–2315.

[76] N. Metropolis, A.W. Rosenbluth, M.N. Rosenbluth, A.H. Teller, and E. Teller, *Equation of state calculations by fast computing machines*, J. Chem. Phys. **21** (1953), 1087–1092.

[77] B.A. Berg, *Double jacknife bias corrected estimators*, Comp. Phys. Commun. **69** (1992), 7–15.

[78] R. Chandra, L. Dagum, D. Kohr, D. Maydan, J. McDonald, and R. Menon, *Parallel programming in OpenMP*, Morgan Kaufman, 2001.